UNIVERSITY OF OKLAHOMA

GRADUATE COLLEGE

SEISMIC ATTRIBUTES ASSISTED QUANTITATIVE UNCONVENTIONAL RESERVOIRS CHARACTERIZATION

A DISSERTATION

SUBMITTED TO THE GRADUATE FACULTY

in partial fulfillment of the requirements for the

Degree of

DOCTOR OF PHILOSOPHY

By

XUAN QI
Norman, Oklahoma
2018

SEISMIC ATTRIBUTES ASSISTED QUANTITATIVE UNCONVENTIONAL RESERVOIRS CHARACTERIZATION

A DISSERTATION APPROVED FOR THE
CONOCOPHILLIPS SCHOOL OF GEOLOGY AND GEOPHYSICS

BY

_____
Dr. Kurt Marfurt, Chair

_____
Dr. Jamie Rich, Co-chair

_____
Dr. Matthew Pranter

_____
Dr. Xiaowei Chen

_____
Dr. Zulfiquar Reza

To my family

ACKNOWLEDGMENTS

This journey would not have been possible without persisting hard work and support of my professors and mentors, family and friends.

I must thank all of faculties and staffs in ConocoPhillips School of Geology and Geophysics whom I have worked with over the last five years. Each of you has given your time, energy, and expertise and I am richer for it: Dr. Roger Slatt, Dr. Lynn Soreghan, Dr. Shankar Mitra, Dr. Gail Holloway, Dr. John Pigott, Dr. Brad Wallet, Dr. Randy Keller, Dr. Ze'ev Reches, Rebecca Fay, Amber Roberts, Donna Mullins, Nancy Lenard, Wei Wang, Ginny Gandy-Guedes, Ginger Leivas, and Leah Moser.

I would like to give special thanks to my dissertation committee. I owe a debt of gratitude to Dr. Jamie Rich for accepting as his student and giving me a chance to study in the geoscience department. Unlike other students, who have a geophysics background, I was entirely new to the geoscience field. His kindness and "laid-back" style of guidance, gave me enough time and space to work at my own speed and catch up with the other students.

I would like to thank Dr. Kurt Marfurt, my co-chair, and Ph.D. advisor. It is hard to come up with words of wisdom for someone so wise, so I genuinely appreciate having him as my advisor. After entering the AASPI group, I always had self-doubt not being smart enough. He treated me with nothing but respect and gave me confidence in believing in myself. His profound knowledge, passion for research and optimistic spirit guide me towards the right track in this field.

I would also like to show my greatest gratitude to Dr. Matthew Pranter, Dr. Xiaowei Chen, Dr. Deepak Devegowda, and Dr. Zulfiquar Reza, who serve on my Ph.D. committee. Thank Dr. Matthew Pranter for sponsoring my first research project, and for

providing his guidance in addressing shortcomings in my projects. His work ethic and attention to detail always motivate me. Dr. Xiaowei Chen encourages me a lot both in coursework and daily life. Dr. Deepak Devegowda shared his expertice in statistical and machine learning. Special thanks to Dr. Zulfiquar Reza for agreeing to be my committee member under such short notice. All of them set great examples of successful young professionals, it is my great honor to have them on my committee.

I would like to thank all team members and sponsors of the "Mississippi Lime" and Attribute Assisted Seismic Processing and Interpretation (AASPI) consortia for their continuous support. Special thanks to Thang Ha, Bin Lyu, and Jie Qi for your constant inspiration.

I would like to thank Marathon Oil Co. for a lience to their Barnett Shale survey used in chapter 2, or this dessertation is possible without data. I would like to thank Chesapeaks Energy for a license to their NW Oklahoma Mississippi Limestone survey used in chapter 3 and 4. I specifically thank Stephanie Cook for her interpretation and analyze of the image logs data and providing of the mud log data.

Finally, yet importantly, I want to thank my family and friends. To my family, thank you for encouraging me in all my pursuits and inspiring me to follow my dreams. I am especially grateful to my patents, who supported me emotionally and financially. I always knew that you believed in me and wanted the best for me. Thank you for teaching me that my job in life was to learn, to be happy, and to know and understand myself. I owe thanks to a very special person, my husband, Wei for his continued and unfailing love, support and understanding during my pursuit of the Ph.D degree that made the completion of this dissertation possible. I appreciate my baby, my little girl Jade for

coming into my life and making me smile like crazy. To my friends, thank you for listening, offering me advice, and supporting me through this entire process.

TABLE OF CONTENTS

LIST OF TABLES

LIST OF FIGURES

ABSTRACT

Unconventional reservoirs cover a wide range of hydrocarbon-bearing formations and reservoir types that generally do not produce economic rates of hydrocarbons without stimulation. The focus of this dissertation is to develop and calibrate workflows to aid in the characterization of the highly heterogeneous Mississippi Limestone reservoir play of northern Oklahoma. Because natural fractures and faults are the primary pathways for hydrocarbon migration and production in many reservoirs, naturally fractured reservoirs represent a significant percentage of oil and gas reservoirs throughout the world. In 2012, unconventional shale gas productions were accounting for 34% of the total natural gas production in the U.S. (0.68 trillion m^3). Because of their complexity and commercial significance, naturally fractured reservoirs have been extensively studied showing that the in-situ stress field, lithology, formation thickness, structural setting and other geological factors all play a role. The understanding of the magnitude, timing, and distribution of these controlling factors could lead to an improvement in the characterization of fractures in reservoirs. Although, the geomechanical history of the rocks is elusive and often speculative, one can infer the magnitude and orientation of paleostresses and thereby hypothesize the degree of fracturing given current structure. Reservoir structure are mapped using petrophysical logs and seismic techniques where seismic attributes such as coherence and curvature are commonly used to map deformation in the subsurface. This dissertation introduces a new edge-detecting seismic attribute, aberrancy that quantitatively estimates the orientation and magnitude of poorly resolved faults as well as flexures in the subsurface. The rate of penetration (ROP) measures drilling speed, which is indicative of the overall time and in general, the cost of the drilling operation process. ROP depends on many engineering factors; however, if

these parameters are held constant, ROP is a function of the geology. This dissertation is the first study that links ROP to seismic data and seismic-related attributes using proximal support vector machine. By using this workflow, we anticipate that this process can help better predict a budget or even reduce the cost of drilling when an ROP assessment is made in conjunction with reservoir quality and characteristics. Due to the complexity of fracture characterization, fracture prediction is more commonly the product of comprehensive integration of software, data, and specialize measurements specific to unconventional reservoirs. To calibrate volumetric aberrancy. I integrate seismic attributes and borehole image logs as the input to neural network. The findings on the use of volumetric aberrancy as an aid to structrual interpretation and quantitative fracture prediction.

CHAPTER 1

INTRODUCTION

The term “unconventional reservoirs” covers a wide range of hydrocarbon-bearing formations and reservoir types that generally do not produce economic rates of hydrocarbons without stimulation. Common terms for such “unconventional reservoirs” include: Tight-Gas Sandstone, Gas Hydrates, Oil Shale formations, Heavy Oil Sandstones, and Shale Gas (Passey et al., 2010). The focus of this dissertation is to discuss the characterization of the Shale Gas and Carbonate reservoir assisted by seismic technique.

Because natural fractures and faults are the primary pathways for hydrocarbon migration and production in many reservoirs, natural fractured reservoirs represent a significant percentage of oil and gas reservoirs throughout the world (Ouenes, 2000). In 2012, unconventional shale gas productions were accounting for 34% of the total natural gas production in the U.S. (0.68 trillion m^3) (Vengosh et al., 2014). Because of their complexity and commercial significance, natural fractured reservoirs have been extensively studied. Many of the efforts have been dedicated to exploring the possible factors that may affect rock fracturing. Numerous approaches have been used to estimate the spatial distribution of fractures within individual horizons (Gale et al., 2007). Gale et al. (2007) characterized natural fractures using four Barnett Shale cores. Through measuring a suite of mechanical rock properties, he concluded that the geometry of the fracture system and in-situ stress field are two most critical factors that control the direction of hydraulic fracture propagation as well as natural fracture system. The

approach mentioned above was applied to small areas encompassing the scale of a gas field. Although structural aspects can be important, it is demanding to recognize there is a complex interplay between the driving factors. For example, fractures characteristics in carbonates are as variable as the range of carbonate lithologies, fabrics, and structural settings (Lorenz et al., 2012). Structure and tectonics cause the stresses that initiate fracturing within a package of rock, while lithology is the primary control on fractures susceptibility (Lorenz et al., 2012). Of these two controls, lithology is commonly more important than the structural position in determining the intensity of fracturing in carbonate strata, although structure becomes more import as deformation increases (Lorenz et al., 2012). Another factor in carbonates fracture characterization is solubility (Lorenz et al., 2012). Formation fluids within the fractures may have dissolved much of the adjacent rock, leaving mismatched fracture walls and significant volumes of vuggy, fracture-related porosity (Lorenz et al., 2012). It is imperative to identify the primary geologic controlling factors. Only then can a comprehensive fracture prediction model be generated.

As discussed above, in-situ stress field, lithology, formation thickness, structural setting and other geological factors are recognized to leave an impact in fractured reservoirs. The understanding of the magnitude, timing, and distribution of these controlling factors could lead to an improvement in the characterization of fractures in reservoirs. Unfortunately, the geomechanical history of the rocks is elusive and often speculative (Ouenes, 2000). Study pointed out paleostresses are, to some extent, revealed

by present-day curvature. Hence, one can infer the magnitude of paleostresses and gain insight into the degree of fracturing given current structure (Ouenes, 2000).

Reservoir structure can be obtained easily using petrophysical logs and seismic techniques. Geometric seismic attributes such as coherence allow interpreters to quickly visualize and map complex fault systems (Chopera, 2002). Volumetric curvature provides not only images of folds, domes, and collapse features, but also helps interpreters map faults whose vertical throw fall below seismic resolution (Chopra and Marfurt, 2007). Aberrancy measures the lateral change (or gradient) of the curvature of a picked or inferred surface, and as such provides not only an indication of the strength of the normal faulting, but also the direction fo the downthrown side (discussed in Chapter 2).

Seismic-reflection data used in reservoir characterization not only for obtaining the insight of geometric information of subsurface structures but also for estimating geomechanical properties such as lithologies and fluids. Rock physics allows us to link seismic response with reservoir properties. Impedance inversion is currently the most direct seismic-based estimate of rock properties. Seismic-impedance inversion results have been used to predict fault zones, potential fractures, and lithology in the Mississippian Limestone (Dowdell et al., 2013; Roy et al., 2013; Verma et al., 2013; Lindzey et al., 2015) (discussed in Chapter 3). Young's modulus, E, and Poisson's ratio, υ, calculated from bulk density, ρ, compressional velocity, V_p, and shear velocity, V_s logs can be used to estimate rock brittleness (Harris et al., 2011).

Seismic imaging brings large-scale reservoir behavior. Geostatistical stochastic stimulations add spatial correlation and small-scale variability which is hard to identify

from seismic due to the limits of resolution. Two machine learning techniques will be applied and discussed in this dissertation: the proximal support vector machine (PSVM) (Chapter 3) and artificial neural network (ANN) (Chapter 4). The PSVM method is a more recent innovation that has been successfully used to predict brittleness (Zhang et al., 2015), seismic facies recognition (e.g., channels, mass-transport complexes, etc.) (Zhao et al., 2015) and lithofacies classification (Zhao et al., 2014). Neural networks have been applied successfully in geophysics since last decade. Neural networks have been used for waveform recognition (Murat and Rudman, 1992), electromagnetic (Poulton et al., 1992), well log analysis (Hampson et al., 2001), seismic inversion (Bosch et al., 2010), and many other problems.

Due to the complexity of fracture characterization, fracture prediction is more commonly the product of comprehensive integration of software, data, and specialize measurements specific to unconventional reservoirs (**Figure 1.1**). Mukerji et al., (2001) combined three techniques to reduce the uncertainty of reservoir characterization. He integrated geological facies indicator (derived from cores, thin section, and production data), seismic attributes (derived from seismic inversion), and geostatistics method (such as variograms) to guide quantitative decision analysis. I will apply similar workflow in my third research topic (Chapter 4), which integrated geomechanical rock properties, seismic attributes, and neural network method to predict the fracture intensity over the Mississippian Limestone horizon located at central Oklahoma.

I structure the dissertation as follows. Chapter 2 is divided into two sections. In section 1, I will provide an in-depth review and comparison of some of the most popular

seismic geometric attributes that have been applied to characterize faults and fractures. In section 2, I will introduce aberrancy, a new seismic attributes volume developed by Dr. Marfurt and me. I will begin section 2 by summarizing the theory of aberrancy. I will then apply volumetric aberrancy calculation first to two synthetic models: a 3D synthetic of a circular sinkhole model and a 3D synthetic consisting of an EW-trending flexure and three NS-trending flexures. Next, I will present an application of volumetric aberrancy to a data volume acquired over the Barnett Shale gas reservoir of Fort Worth Basin, Texas. In Chapter 3, I will present a case study linking seismic attributes and geomechanical properties of Mississippian Limestone strata with a petroleum measurement rate of penetration using proximal support vector machine (PSVM). This case study is over a carbonate reservoir located at central Oklahoma. In this case study, I will cast workflow details for those wishing to create a similar model. In chapter 4, I will inherit the knowledge from Chapter 2 and 3, integrate aberrancy and other eight seismic attributes and geomechanical properties with a neural network to predict fracture intensity in the same carbonate reservoir discussed in chapter 3. Finally, I will sum up the materials from Chapter 2 to 4 with conclusions in Chapter 5.

CHAPTER 1 FIGURES

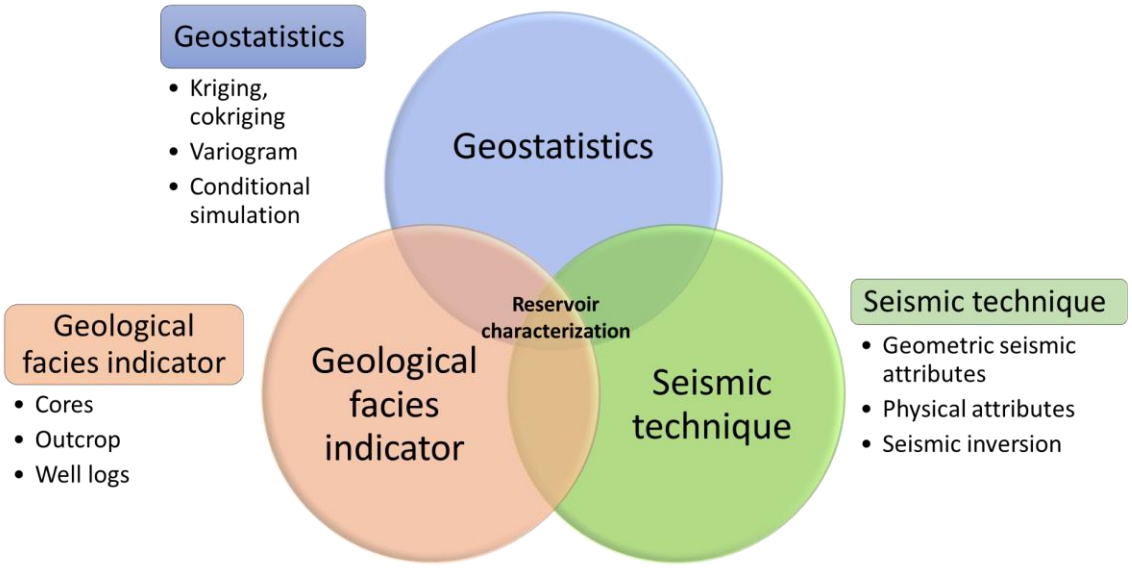

Figure 1.1. The conceptual diagram demonstrates fracture prediction is the product of comprehensive integration of software, data, and specialize measurements specific to unconventional reservoirs.

REFERENCES

Bosch, M., T. Mukerji, and E. F. Gonzalez, 2010, Seismic inversion for reservoir properties combining statistical rock physics and geostatistics: A review: Geophysics, **75**, 75A165-75A176, doi:10.1190/1.3478209.

Chopera, S., 2002, Technical article: Coherence cube and beyond: First Break, **20**, 27–33, doi:10.1046/j.1365-2397.2002.00225.x.

Chopra, S., and K. Marfurt, 2007, Seismic Attributes for Prospect Identification and Reservoir Characterization: Society of Exploration Geophysicists and European Association of Geoscientists and Engineers, doi:10.1190/1.9781560801900.

Dowdell, B. L., J. T. Kwiatkowski, and K. J. Marfurt, 2013, Seismic characterization of a Mississippi Lime resource play in Osage County, Oklahoma, USA: Interpretation, **1**, SB97–SB108, doi:10.1190/INT-2013-0026.1.

Gale, J. F. W., R. M. Reed, and J. Holder, 2007, Natural fractures in the Barnett Shale and their importance for hydraulic fracture treatments: AAPG Bulletin, **91**, 603–622.

Hampson, D. P., J. S. Schuelke, and J. A. Quirein, 2001, Use of multiattribute transforms to predict log properties from seismic dataUsing Attributes to Predict Logs: Geophysics, **66**, 220, doi:10.1190/1.1444899.

Harris, N. B., J. L. Miskimins, and C. A. Mnich, 2011, Mechanical anisotropy in the Woodford Shale, Permian Basin: Origin, magnitude, and scale: The Leading Edge, **30**, 284–291, doi:10.1190/1.3567259.

Lindzey, K., M. J. Pranter, and K. Marfurt, 2015, Geologically constrained seismic characterization and 3-D reservoir modeling of Mississippian reservoirs, North Central Anadarko Shelf, Oklahoma: AAPG Annual Convention and Exhibition, Denver, Colorado, May 31–June 3, 2015.

Lorenz, J. C., H. E. Farrell, C. L. Hanks, W. D. Rizer, and M. D. Sonnenfeld, 2012, 8. Characteristics of Natural Fractures in Carbonate Strata, in Carbonate Seismology: 179–202, doi:10.1190/1.9781560802099.ch8.

Mukerji, T., P. Avseth, G. Mavko, I. Takahashi, and E. F. González, 2001, Statistical rock physics: Combining rock physics, information theory, and geostatistics to reduce uncertainty in seismic reservoir characterization: The Leading Edge, **20**, 313–319, doi:10.1190/1.1438938.

Murat, M. E., and A. J. Rudman, 1992, AUTOMATED FIRST ARRIVAL PICKING: A NEURAL NETWORK APPROACH1: Geophysical Prospecting, **40**, 587–604, doi:10.1111/j.1365-2478.1992.tb00543.x.

Ouenes, A., 2000, Practical application of fuzzy logic and neural networks to fractured reservoir characterization: Computers & Geosciences, **26**, 953–962, doi:https://doi.org/10.1016/S0098-3004(00)00031-5.

Passey, Q. R., K. Bohacs, W. L. Esch, R. Klimentidis, and S. Sinha, 2010, From Oil-Prone Source Rock to Gas-Producing Shale Reservoir - Geologic and Petrophysical Characterization of Unconventional Shale Gas Reservoirs: Beijing, China, Society of Petroleum Engineers, doi:10.2118/131350-MS.

Poulton, M. M., B. K. Sternberg, and C. E. Glass, 1992, Location of subsurface targets in geophysical data using neural networks: Geophysics, **57**, 1534–1544, doi:10.1190/1.1443221.

Roy, A., B. L. Dowdell, and K. J. Marfurt, 2013, Characterizing a Mississippian tripolitic chert reservoir using 3D unsupervised and supervised multiattribute seismic facies analysis: An example from Osage County, Oklahoma: Interpretation, **1**, SB109–SB124, doi:10.1190/INT-2013-0023.1.

Vengosh, A., R. B. Jackson, N. Warner, T. H. Darrah, and A. Kondash, 2014, A Critical Review of the Risks to Water Resources from Unconventional Shale Gas Development and Hydraulic Fracturing in the United States: Environmental Science & Technology, **48**, 8334–8348, doi:10.1021/es405118y.

Verma, S., O. Mutlu, and K. J. Marfurt, 2013, Seismic modeling evaluation of fault illumination in the Woodford Shale, in James Schuelke, ed., SEG Technical Program Expanded Abstracts 2013, 3310–3314.

Zhang, B., T. Zhao, X. Jin, and K. Marfurt, 2015, Brittleness evaluation of resource plays by integrating petrophysical and seismic data analysis: Interpretation, **3**, T81–T92, doi:10.1190/INT-2014-0144.1.

Zhao, T., V. Jayaram, K. J. Marfurt, and H. Zhou, 2014, Lithofacies classification in Barnett Shale using proximal support vector machines, in B. Birkelo, ed., SEG Technical Program Expanded Abstracts 2014, 1491–1495.

Zhao, T., V. Jayaram, A. Roy, and K. J. Marfurt, 2015, A comparison of classification techniques for seismic facies recognition: Interpretation, **3**, SAE29–SAE58, doi:10.1190/INT-2015-0044.1.

CHAPTER 2

VOLUMETRIC ATTRIBUTES TO MAP SUBTLE FAULTS AND FLEXURES[1]

ABSTRACT

One of the key tasks of a seismic interpreter is to map lateral changes in surfaces, not only including faults, folds, and flexures, but also incisements, diapirism, and dissolution features. Volumetrically, coherence provides rapid visualization of faults and curvature provides rapid visualization of folds and flexures. Aberrancy measures the lateral change (or gradient) of curvature along a picked or inferred surface. Aberrancy complements curvature and coherence. In normally faulted terrains, the aberrancy anomaly will track the coherence anomaly and fall between the most positive curvature anomaly defining the footwall and the most negative curvature anomaly defining the hanging wall. Aberrancy can delineate faults whose throw falls below the seismic resolution or is distributed across a suite of smaller conjugate faults that do not exhibit a coherence anomaly. Previously limited to horizon computations, we extend aberrancy to uninterpreted seismic data volumes. We apply our volumetric aberrancy calculation to a data volume acquired over the Barnett Shale gas reservoir of the Fort Worth Basin, Texas. In this area, the Barnett Shale is bound on the top by the Marble Falls Limestone and on the bottom by the Ellenburger Dolomite. Basement faulting controls karstification in the

---

[1] *This chapter contains contents from a published article - X. Qi and K. Marfurt, 2018, Volumetric aberrancy to map subtle faults and flexures: Interpretation*

Ellenburger, resulting in the well-known “string of pearls” pattern seen on coherence images. Aberrancy delineates small karst features, which are, in many places, too smoothly varying to be detected by coherence. Equally important, aberrancy provides the azimuthal orientation of the fault and flexure anomalies.

INTRODUCTION

As briefly introduced in Chapter 1, seismic attributes are the measure of seismic data that help us visually enhance or quantify features of interpretation interest (Chopra and Marfurt, 2007a). The deformation of rocks due to faulting and fracturing may cause changes in lithology and pore pressure, and thus affect seismic velocity and amplitude (Mooney and Ginzburg, 1986). Mooney and Ginzburg (1986) found out that highly fractured rock and thick fault gauge along the creeping portion of the San Andreas fault linked with a pronounced seismic low-velocity zone. Because observations of the seismic anisotropy have the potential of providing the orientation of the in-situ stress field, several theoretical studies of fracture-induced anisotropy have been reported in the literature (Schoenberg and Sayers, 1995). Among the various geophysical technique available for characterizing faults and fractures, 3-dimensional (3D) seismic attributes are particularly useful for interpreting faults and channels, unraveling the structural deformation history, and organize subtle features into displays (Chopra and Marfurt, 2007a). This chapter is divided into two subsections: section one focuses on the reviewing of existing volumetric seismic attributes to map subtle faults and flexures. Section two focuses on introducing volumetric aberrancy and its application in a case study, Fort Worth Basin.

A REVIEW OF VOLUMETRIC ATTRIBUTES TO MAP FAULTS AND FLEXURES

Taner et al. (1994) divide seismic attributes into two general categories: geometrical and physical. The geometrical attributes help to enhance the visibility of the geometrical characteristics of seismic data; they include dip, azimuth, coherence, curvature, and continuity (Chopra and Marfurt, 2005). Physical attributes have to do with the physical parameters of the subsurface and so relate to lithology; they include amplitude, phase, and frequency (Chopra and Marfurt, 2005).

Volumetric dip and azimuth

In seismology, dip is a vector consisting of dip magnitude and dip azimuth. Dip magnitude, θ, is identical to that used in the above geologic definition. Dip azimuth, φ, is measured either from the north, or for convenience, from the inline seismic survey axis. Azimuth is perpendicular to the geologic strike and is measured in the direction of maximum downward dip. Dip magnitude and azimuth volumes can be a very convenient tool in defining a local reflector surface upon which we estimate discontinuity features. The discontinuity features include chaotic slumps, infill of karsted terrains, angular unconformities and of course faults and flexures (Marfurt, 2006). Inline and crossline dip components in **Figure 2.1**, delineate detail of a system of complex joints and fractures. A robust estimate of vector dip allows us to generate curvature attributes throughout the entire survey volume (Marfurt, 2006).

Coherence

Coherence measures the similarity between waveforms or trace. The seismic waveform is a response of the seismic wavelet convolved with the geology subsurface. Any changes in response such as amplitude, frequency, and phase depending on the acoustic-impedance contrast and thickness of the layers above and below the reflecting boundary (Chopra and Marfurt, 2007a). Because acoustic-impedance is closely related to the lithology, porosity, density and fluid type of the subsurface layers, consequently, strong lateral changes in subsurface layers give rise to strong later changes in waveform character. Coherence allows interpreters to quickly visualize and map complex fault systems, salt and shale diapirs and incoherent overpressured shales (Chopra and Marfurt, 2007a). Bahorich and Farmer (1995) used coherence attribute to map faults on time slices that are not readily seen on conventional amplitude slices (**Figure 2.2**). Using traditional methods, it is often difficult to get a clear and unbiased view of faults and stratigraphic features hidden in the 3-D data (Bahorich and Farmer, 1995). It allows an interpreter to view geologic features in map view without having to pick seismic events. Large faults are often readily seen on vertical cross-sections, but time slice view allows interpreters to determine the lateral extent of faulting (Bahorich and Farmer, 1995).

Volumetric curvature

Curvature describes how bent a curve is at a particular point on the curve. Curvature in two dimensions is defined as the radius of a circle tangent to a curve (**Figure 2.3**) (Chopra and Marfurt, 2007a). Chopra and Marfurt, (2007a) defined anticlines as having positive curvature and synclines as having negative curvature. Linear (straight-line) portions of a curve have zero curvature. For example, portions with a constant dip

show zero curvature. Curvature in three dimensions is defined using two circles tangent to a surface. The circles always reside in orthogonal planes. The centers of these circles lie along an axis that is perpendicular to a plane tangent to the surface (Chopra and Marfurt, 2007a).

Curvature has been accepted as a promising attribute to predict fractures from surface seismic data (Chopra and Marfurt, 2007a). Both theoretical research and lab experiments show that large curvature values correlate with high-stress field and thus explained the increasing probability of fracturing (Hunt et al., 2011; White et al., 2012). However, the relationship between open fractures and curvature measures is proven quite complicated and can be controlled by lithology, precious faults and fractures zones, the paleo-stress regime, pore pressures, and the present-day stress regime (Chopra and Marfurt, 2007a).

Although direct prediction of open fractures using curvature requires a significant amount of geologic unraveling and calibration through production data, curvature images are a powerful aid to conventional structural and stratigraphic interpretation. Studies prove that the most-positive curvature, k_{pos}, and the most-negative curvature, k_{neg}, are the most helpful and widely used in delineating faults, fractures, and folds (Chopra and Marfurt, 2007b). Chopra and Marfurt used the most-positive and most-negative curvature to map channel system **(Figure 2.4),** which stands out with the main limb running northwest-southeast. Because of differential deposition compaction, the most-negative curvature highlights the channel axis, while the most-positive curvature delineates the

flanks of the channels, potential levee, and over-bank deposits (Chopra and Marfurt, 2007b).

VOLUMETRIC ABERRANCY

Well known to mathematicians (Schot, 1978), aberrancy has only recently been applied to 3D seismic surveys. Gao, (2013) defines aberrancy as a measure of the deformation of a surface. Aberrancy measures the lateral change (or gradient) of the curvature of a picked or inferred surface. In three dimensions, aberrancy is a vector described by its magnitude and azimuth. The magnitude defines the intensity of surface deformation, while the azimuth indicates the direction in which the curvature decreases in signed value. This positive-to-negative definition provides as azimuth consistent with that of fault plane azimuths.

Gao and Di, (2015) find aberrancy to be complementary to curvature. In normally faulted terrains, the aberrancy anomaly will track the coherence anomaly and fall between the most-positive curvature anomalies defining the footwall and the most-negative curvature anomalies defining the hanging walls (Chopra and Marfurt, 2007b). Unlike coherence, which measures lateral changes in waveform and/or amplitude, aberrancy measures lateral changes in curvature, and as such provides not only an indication of the strength of the normal faulting (the magnitude of the vector), but also the direction of the downthrown side (the azimuth of the vector).The value of aberrancy is that it may delineate faults whose throw falls below seismic resolution, or is distributed across a suite of smaller conjugate faults, which do not exhibit a coherence anomaly (Di and Gao, 2016)

(**Figure 2.5**). For this reason, we hypothesize that aberrancy will be quite useful in correlating surface seismic data to fractures associated with faults that are commonly seen in image logs from horizontal wells.

Because aberrancy measures the changes in curvature, it characterizes the third-order surface behavior (Joshi and Séquin, 2010). Calculation of aberrancy involves two main challenges, the robustness of high order derivatives, and computational efficiency. Di and Gao (2014) introduced a horizon-based aberrancy calculation based on first computing 3rd derivatives at equal azimuthal intervals. They then search these values for extrema. More recently, Di and Gao (2016) they showed how rotating the coordinate system can simplify the equations. We build on this latter innovation and generalize it to compute aberrancy volumetrically. We compute 2^{nd} derivatives of vector dip in the *x*, *y*, and *z* directions, rotate the calculations about the local vector dip to simplify the computation, compute aberrancy, and then rotate the aberrancy vectors back the original coordinate system. In general, there are three roots to the 3^{rd} order differential equation (Di and Gao, 2016), where we define as the maximum aberrancy, the minimum aberrancy, and the intermedium aberrancy. We begin this paper by summarizing the theory of aberrancy. We then apply our volumetric aberrancy calculation first to two synthetic models: a 3D synthetic of a circular sinkhole model and a 3D synthetic consisting of an EW-trending flexure and three NS-trending flexures. Next, we apply our volumetric aberrancy algorithm to a data volume acquired over the Barnett Shale gas reservoir of Fort Worth Basin, Texas. We conclude with a summary of interpretational

value of the attribute as well as the computational cast mathematical details for those wishing to implement such an algorithm are provided in the appendices.

Apparent dip, curvature, and aberrancy

Geoscientists define a locally planar surface by its dip magnitude, θ, and dip azimuth, φ, where θ is sometimes called the "true dip" to distinguish it from the apparent dip at an azimuth β. Introducing the dip vector, **p**, measured in dimensionless units of km/km or kft/kft, the components of the true dip along the x_1 and x_2 axes are

$$\begin{aligned} p_1 &= \tan\theta\cos\varphi, \\ p_2 &= \tan\theta\sin\varphi, \end{aligned} \tag{1}$$

while the apparent dip component p_β and apparent dip angle θ_β along the azimuth β are

$$\begin{aligned} p_\beta &= \tan\theta\cos\beta, \\ \theta_\beta &= \tan^{-1} p_\beta, \end{aligned} \tag{2}$$

Most geoscientists are also familiar with the two principal (most-positive and most-negative) curvature values, k_1 and k_2, and their corresponding strikes, γ_1 and γ_2, where Rich and Marfurt (2013) shows that they are the eigenvalues and eigenvectors of a solid geometry problem. Somewhat less familiar is the apparent curvature at a given azimuth, or Euler curvature, k_β, at strike β defined as

$$k_\beta = k_1\cos^2(\beta-\gamma_1) + k_2\sin^2(\beta-\gamma_1), \tag{3}$$

Di and Gao (2014) show that one can compute the most-positive and most-negative principal curvatures by searching for extrema of the Euler or apparent

curvatures. This search is significantly simplified if one first locally flattens the data about the vector dip at the analysis point. While this approach is somewhat less efficient than the more commonly used eigenvector curvature solution, it provides not only physical insight into the meaning of the principal curvatures, it also provides a means to compute the extrema of aberrancy.

Because the vector dip at any voxel can be different from its neighbors, a direct implementation of Di and Gao's (2014) algorithm would require rotating an analysis window of volumetric dip values, **p**, followed by the computation of its derivatives using a convolution operator. In our implementation, this convolution operator typically uses 121 traces and 50 vertical samples, or a computational stencil of 6050 points, which would not be amenable to vector computing strategies. We therefore compute the required derivatives in the original unrotated coordinate system, and then obtain the corresponding derivatives in the locally rotated coordinate system through three cascaded rotation operators applied to the 3x3x3, or 27-element second derivative operators applied to the three vector dip components (**Figure 2.6**). These details are important to those who wish to implement aberrancy, but provide only limited insight into its use and are thus relegated to Appendix A.

After rotation, one can compute the apparent aberrancy at any azimuth, ψ, in the rotated plane, using equation B-3, repeated here

$$f_{\psi} = \frac{\partial^3 z'}{\partial x_1' \partial x_1' \partial x_1'} \cos^3 \psi + 3 \frac{\partial^3 z'}{\partial x_1' \partial x_1' \partial x_2'} \cos^2 \psi \sin \psi + 3 \frac{\partial^3 z'}{\partial x_1' \partial x_2' \partial x_2'} \cos \psi \sin^2 \psi + \frac{\partial^3 z'}{\partial x_2' \partial x_2' \partial x_2'} \sin^3 \psi,$$

(4)

where the primes indicate the surface $z'(x_1', x_2')$ in the rotated coordinate system. For volumetric aberrancy, one does not explicitly pick surfaces, but rather computes the first derivatives of assumed surfaces, resulting in the volumetric dip component volumes, p_1 and p_2 defined in equation, equation 4 then becomes

$$f_{\psi} = \frac{\partial^2 p_1'}{\partial x_1' \partial x_1'} \cos^3 \psi + \frac{3}{2} \left(\frac{\partial^2 p_1'}{\partial x_1' \partial x_2'} + \frac{\partial^2 p_2'}{\partial x_1' \partial x_1'} \right) \cos^2 \psi \sin \psi + \frac{3}{2} \left(\frac{\partial^2 p_1'}{\partial x_2' \partial x_2'} + \frac{\partial^2 p_2'}{\partial x_1' \partial x_2'} \right) \cos \psi \sin^2 \psi + \frac{\partial^2 p_2'}{\partial x_2' \partial x_2'} \sin^3 \psi.$$

(5)

The extrema of the aberrancy are computed by minimizing the value of f_{ψ} with respect to ψ. Recall that vector dip is computed using the first derivative of the surface, *z*, and has one extrema, the dip magnitude and the dip azimuth, which define a single dip vector. Curvature is computed using the second derivatives of the surface *z* and has two extrema, the most-positive and most-negative principal curvatures and their strikes. Aberrancy is computed using the third derivatives (equation 4) of the surface *z* and therefore will have in general three extrema. We will call these extrema the maximum, intermediate, and minimum aberrancy vectors expressed by its magnitude, f_{ψ} and its azimuth ψ (Borwein et al.,2012). The numerical roots of the minimization problem are in terms of tan ψ (equation B-1), such that initially ψ ranges between $\pm 90^0$. Inserting these

roots into equation 5 may provide negative values of aberrancy f_ψ. It is obvious that a negative flexure to the north is equivalent to a positive flexure to the south. For this reason, in our implementation, we define our resulting maximum, intermediate, and minimum aberrancy magnitudes, $\mathbf{f_{max}}$, $\mathbf{f_{int}}$, and $\mathbf{f_{min}}$, to be strictly positive, with the corresponding azimuths ψ_{max}, ψ_{int}, and ψ_{min} ranging between $\pm 180^0$. The analysis and display of three roots can be cumbersome, although we hypothesize non-zero values of $\mathbf{f_{int}}$, and $\mathbf{f_{min}}$, represent intersecting flexures which may be indicators of increased shear strain. We leave such quantitative analysis to future work which will require image logs calibration. In this paper we will examine the total vector aberrancy vector, $\mathbf{f_{tot}}$, which is simply the sum of the three aberrancy vectors.

$$\mathbf{f_{tot}} = \mathbf{f_{max}} + \mathbf{f_{int}} + \mathbf{f_{min}}.$$

Synthetic calibration

A 3D synthetic of a circular sink hole model

Figure 2.7 shows a simple 3D synthetic circular model used to validate the aberrancy calculation. The synthetic consists of a circular sinkhole embedded in a planar reflector dipping 2° to the northeast. In this example, the intermediate and minimum aberrancy vectors are near zero (**Figure 2.7d).** Note that, the total aberrancy vector is oriented inwards towards the center of the sinkhole. Also note that the maximum and total aberrancy vectors sit in the approximately middle of the most positive curvature and the most negative curvature (**Figure 2.7b**), where we observe the largest changes in the magnitude of curvature (**Figure 2.7c**).

A 3D synthetic consisting of an EW-trending flexure and three NS-trending flexures.

To calibrate how aberrancy works when two flexures cross each other, we built the simple synthetic model shown in **Figure 2.8a**, consisting of an EW-trending flexure (dipping to the North and appearing as blue), and three NS-trending flexures (dipping towards the east and appearing as red-magenta). The maximum dip of NS flexures increases from 1°, 2°, to 3° from left to right.

Rich and Marfurt (2013) show how the principal curvatures are the solution of an eigenvector problem. The first eigenvalue corresponds to the eigenvector that best represents the deformation at any voxel, and thus is the one exhibiting the largest absolute value, k_{max}. The second eigenvector represents the deformation in the orthogonal direction and is denoted as k_{min}. Note that the patterns exhibited by the weaker flexures (the NS one on the left, and the EW one on the right) are broken by the locally larger flexures (**Figure 2.8b**). Such images make it more difficult to track weak faults cut by stronger faults. In contrast, the most-positive and most-negative principal curvatures, k_1 and k_2, exhibit more continuous pattern. The blue arrow indicates a bowl-shaped anomaly in the most-positive curvature slice, while the red arrow indicates a dome-shaped anomaly in the most-negative curvature image (**Figure 2.8c**).

After examining the maximum, intermediate, and minimum aberrancy vectors, we find that the total aberrancy vector provides a single vector volume appropriate for structural interpretation (**Figure 2.8d**). However, the intermediate and minimum aberrancy indicate zones of conflicting flexure, and depending on the tectonic model, may potentially show areas of more intense natural fracturing.

Application

Geologic background

The Fort Worth basin is a shallow, north-south-elongated foreland basin extending 15,000 mi^2 (38,100 km^2) in north-central Texas (Montgomery et al., 2005). The Ouachita thrust-fold belt, Llano uplift, Bend arch, and the Muenster arch bound the basin to the east, south, west, and north, correspondingly (**Figure 2.9**). Preserved fill in the Fort Worth basin reaches a maximum of about 12,000 ft (3660 m) in the northeast corner, adjacent to the Muenster arch (Montgomery et al., 2005). Deposits consist of about 4000-5000 ft (1200-1500 m) of Ordovician-Mississippian carbonates and shales, 6000-7000 ft (1800-2100 m) of Pennsylvanian clastics and carbonates, and, in the eastern parts of the basin, a thin layer of Cretaceous rocks (Montgomery et al., 2005).

The structures in the Fort Worth basin include both major and minor faulting, local folding, fracturing, and karst-related collapse features (Montgomery et al., 2005; Qi et al., 2014). Thrust-fold structures are more common in the easternmost parts of the basin. Studies have shown that the major fault exerted significant control on the depositional patterns and thermal history of the Barnett (Qi et al., 2014). The small-scale faulting controls karstification in the Ellenburger, resulting in the well-known "string of pearls" pattern seen on seismic coherence images (Schuelke et al., 2014).

The Barnett Shale of the Fort Worth Basin, Texas, has played an important role in a gas-shale play in North America. Recent studies estimate that the Barnett Shales may hold as much as 39 trillion cubic feet of gas (Tcf) undiscovered (Bruner and Smosna, 2011). The Barnett Shale of the Fort Worth Basin, Texas formed during the late Paleozoic

Ouachita Orogeny, generated by the convergence of Laurasia and Gondwana (Bruner and Smosna, 2011). **Figure 2.10** provides a generalized stratigraphy column of the Fort Worth Basin. The Barnett Shale is an organic-rich, petroliferous black shale of middle-late Mississippian age, bound in the survey between the Lower Marble Falls and Ellenburger Group (**Figure 2.10**). The Marble Falls Formation is conformably overlying the Barnett Shale on top. It typically includes two parts, an upper limestone interval and a lower member of interbedded dark limestone and gray-black shale (Montgomery et al., 2005). The top of the Ellenburger Group is an erosional surface (second-order Sauk-Tippecanoe erosional unconformity) commonly characterized by solution-collapse features (Montgomery et al., 2005). We expect to see major and/or minor faulting, local folding, fracturing, and karst-related collapse features within our study area.

Seismic data

In 2006, Marathon Oil Company acquired a 3D wide-azimuth seismic survey to image the Barnett Shale using 16 live receiver lines with a nominal 16×16 m (55×55 ft) CDP bin size (Khatiwada et al., 2013). The overall data quality is excellent, with a poststack data-conditioning workflow including edge-preserving structure oriented filtering and spectral balancing performed by Qi et al. (2014) further improving the continuity and vertical resolution. The top Marble Falls Limestone is an easy-to-pick horizon that lies immediately above the Barnett Shale at approximately 0.7 s two-way time (TWT).

Results

Seismic amplitude

Seismic amplitude is the most commonly used attribute in seismic interpretation. Lines AA' and BB' (**Figure 2.12**) shows two strong reflections, representing the top of the Marble Falls (**Figure 2.11a**) and the top of Ellenburger Group (**Figure 2.11b**). The organic-rich Barnett Shale sits between these two units where arrows indicating karst collapse features. At least two major faults control collapse features indicated by yellow arrows. Several smaller compaction induced sags are seen some distance away from the faults. Even though the seismic amplitude data have been preconditioned, there are several strata-bound low coherence anomalies, some of which are associated with deeper collapse features (cyan arrows), and others simply due to areas exhibiting a low seismic signal-to-noise ratio.

Coherence

Coherence measures the similarity between waveforms on neighboring traces, and helps delineate faults and collapse features in the study area (**Figure 2.12**). **Figures 2.12 and 2.13** shows the same time slices at approximately t = 0.726 s through coherence volume. Time slices through the coherence volume show a complex system of lineaments and collapse features (yellow and white arrows). Although we do see the vertical trace of several faults, the most prominent features are the circular collapse features, which are more pronounced at the deeper Ellenburger level than at the Marble Falls level (**Figure 2.11**).

Curvature

When calibrated to image logs, most-negative and most-positive curvature can serve as a means of predicting fractures from surface seismic data (Chopra and Marfurt,

2007a). **Figure 2.13** shows co-rendered most-positive and most-negative curvature, corendered with coherence on the time slice and with amplitude on the same vertical slice. Notice that the major faults exhibit a positive curvature anomaly on the footwall, which is laterally offset from a corresponding negative curvature anomaly on the hanging wall. The bowl-shaped collapse features exhibit a negative curvature value and appear as blue ellipses (white and yellow arrows).

Aberrancy

Because aberrancy measures the lateral change (or gradient) of the curvature along a picked or inferred surface, it not only detects major faults that exhibit finite displacement, but also more subtle "sub-seismic-resolution" faults that appears as flexures referring to **Figure 2.5**. **Figure 2.5a** shows a finite offset across a fault which results in a strong coherence anomaly (highlighted in red). In contrast, in **Figure 2.5b**, if the offset is distributed over a zone of conjugate faults, where the offsets fall below seismic resolution. The continuous reflector no longer gives rise to a coherence anomaly. Aberrancy measures the change in curvature, highlighting the zone of conjugate faults area that offset a horst block to the east (shaded in red). **Figure 2.14** shows the same slices as in the previous two images, but now through the total aberrancy volume. Orange and green arrows indicate small grabens while white arrows indicate collapse features. **Figure 2.15** shows the same image but now with the addition of coherence on the time slice. In this data volume, the inability of coherence to map subtle featues may be due to geology (a single fault becoming a flexure, fault splay) or data quality issues (limit of seismic resolution of a fault offset, or insufficient statics and velocities limiting the lateral

resolution of the image). **Figure 2.16** shows horizon slices along the top Marble Falls through the maximum, intermediate, minimum, and total aberrancy vectors. The total aberrancy vector provides a single vector volume appropriate for structural interpretation. Lineaments in the total aberrancy vector horizon slices indicate faults or flexures, while flexures that cycle the color wheel (as in the synthetic example shown in figure 1), indicate collapse features. The intermediate and minimum aberrancy may indicate zones of conflicting flexure, and depending on the tectonic model, may potentially show areas of more intense natural fracturing.

Aberrancy is a function of signal to noise ratio (**Figure 2.17, 2.18**). In **Figure 2.18**, note the strong NW-SE trending acquisition footprint in the shallow slice shown in (a). Likewise, the dip estimate in the basement in (c) is also noisy. In contrast, the time slice in (b) through the target Barnett Shale area exhibits a high signal-to-noise ratio. The accuracy of the aberrancy estimates are directly related to the accuracy of the input components of the structural dip vector (d-f). The image in (a) is contaminated by acquisition footprint while that in (c) is noisy, although useful structural lineaments can still be extracted in total aberrancy images.

Comparison between aberrancy and coherence on cross sections

To better understand the collapse patterns, flexures, faults and their expression in the aberrancy attributes, we display three vertical cross-section through seismic survey corresponding to line AA', BB', and CC' in **Figure 2.19-2.21**. Aberrancy seems to be less sensitive to the chaotic zones seen in vertical section AA' and BB', showing flexures that continue vertically through the section. In cross section AA' the anomalies along the

top Marble Falls that are better resolved by aberrancy (**Figure 2.19**). From left to right, aberrancy delineates flexures (indicated by green arrows), which coherence is unable to resolve. In cross section BB', the faults in the aberrancy image appear as steeply dipping continuous thin lines, but as stair step blotches in coherence image (**Figure 2.20**). Similarly, in cross section CC', the collapse features are better resolved by aberrancy, indicated by green arrows (**Figure 2.21**).

CONCLUSION AND DISCUSSION

Tectonic forces, diagenetic dissolution, diapirism, and erosion all act to deform stratigraphic layers that originally may have been deposited with relatively featureless surfaces. While coherence measures disruptions in these surfaces, dip, curvature, and aberrancy measures changes in their orientation and morphology. Lateral changes in dip give use to curvature while lateral changes in curvature give use to aberrancy.

Positive and negative curvature pairs are commonly used to map the footwall and hanging wall of normal faults, bracketing a coherence anomaly. When the fault offset falls below seismic resolution, and the coherence anomaly disappears, the curvature pattern can be used to map the fault further. In general, curvature anomalies are typically juxtaposed to rather than aligned with a fault. In contrast, aberrancy anomalies are aligned with the fault, providing a quantitative measure than can not only be mapped, but also correlated with image logs, production logs, chemical trace data and other measures of fractures.

Previously limited to computation from picked horizons, we have extended aberrancy to provide volumetric results of uninterpreted seismic data volumes. By using along wavelength calculations commonly used in volumetric curvature computations implemented as convolution operators in the original unrotated data volume, we obtain results that are numerically stable, computationally efficient, and geologically meaningful.

While we compute the three aberrancy roots, their value as independent measures has yet to be determined. In contrast, the vector sum of these three roots is easier to understand and interpret. Since it is a vector, total aberrancy images can be azimuthally limited using to highlight and then numerically correlate hypothesized fracture sets to production data.

While aberrancy will provide superior images of certain geologic features, it will complement rather than supplant other structural attributes such as coherence, curvature, and diffraction imaging. Indeed, when used together, they provide deeper insight into the seismic data volume.

CHAPTER 2 FIGURES

(a)

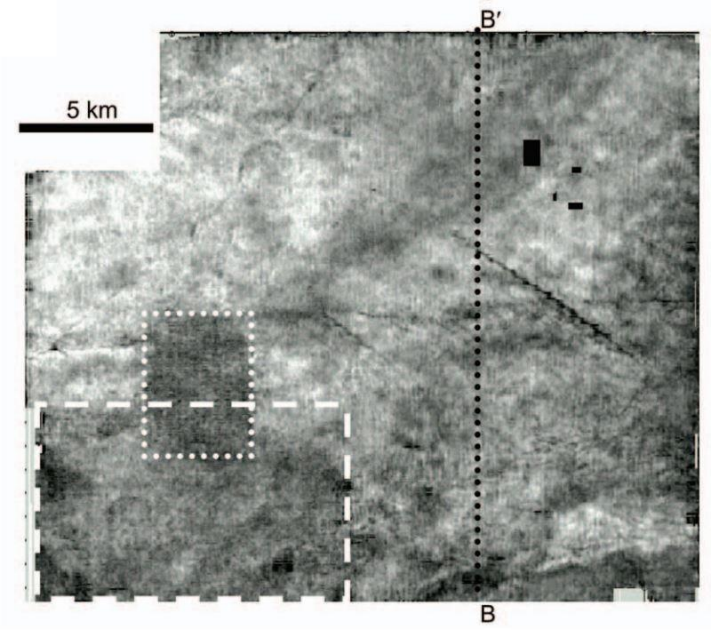

(b)

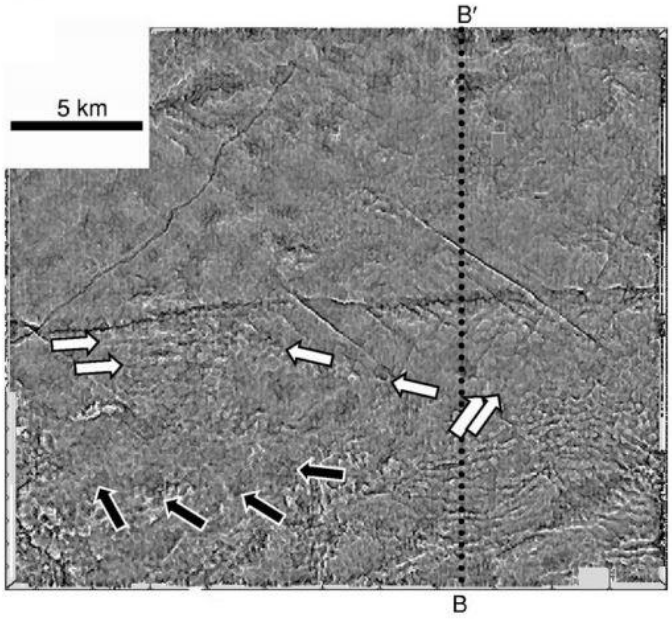

Figure 2.1. (a) amplitude-extract map corresponding to the Caddo horizon. (b) Estimates of inline and crossline dip corresponding to the same horizon (modified from Marfurt 2006).

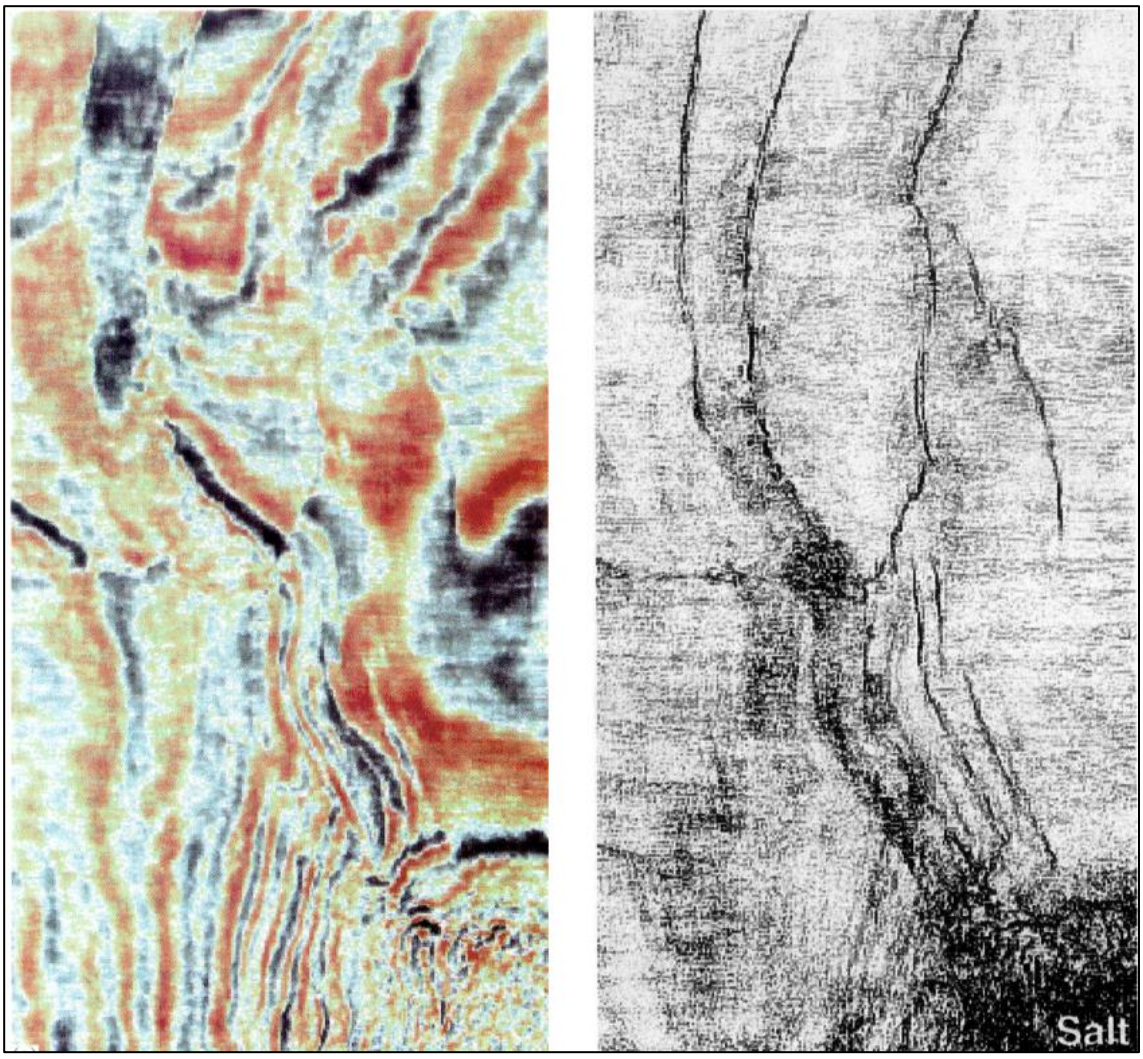

Figure 2.2. The left panel shows traditional 3-D seismic time slice. Fault parallel to strike are difficult to see. The right panel shows coherency time slice. Faults are clearly visible (modified from Bahorich and Farmer 1995).

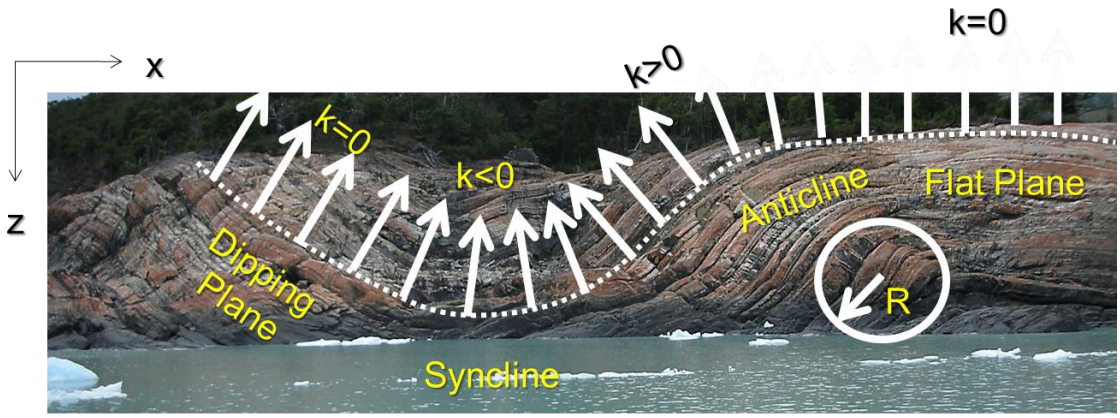

Figure 2.3. An illustrated definition of 2D curvature. Synclinal features have negative curvature, anticlinal features have positive curvature, and planar features have zeros curvature.

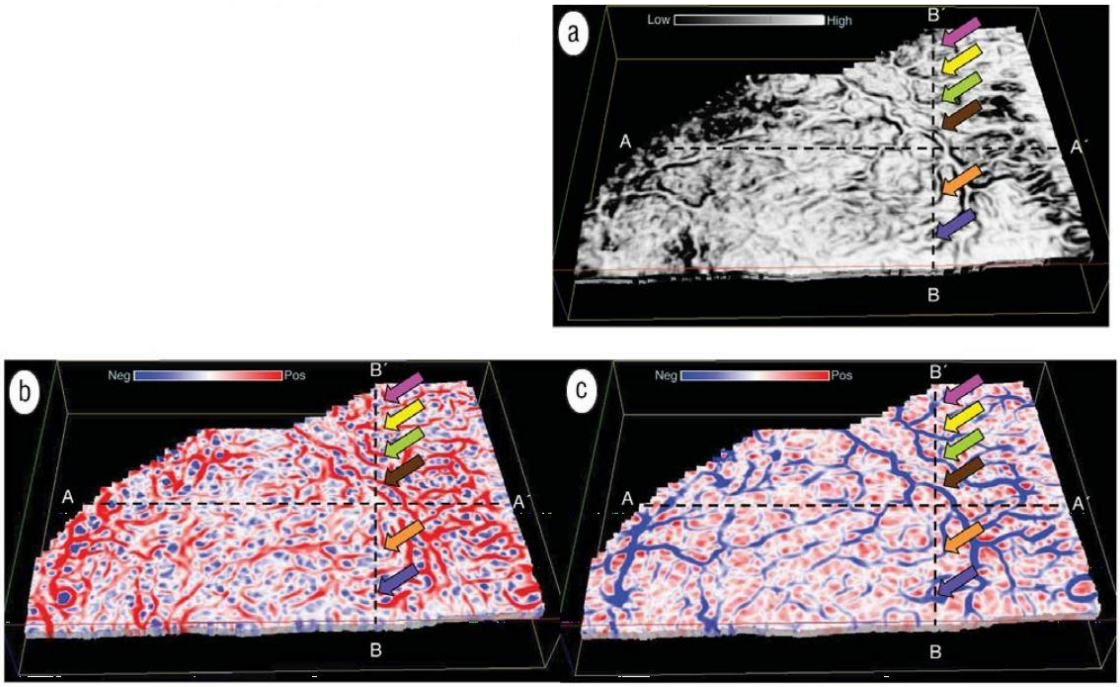

Figure 2.4. Phantom horizon slices through the (a) coherence, (b) most-positive curvature, and (c) most-negative curvature volumes (modified from Chopra and Marfurt, 2007b).

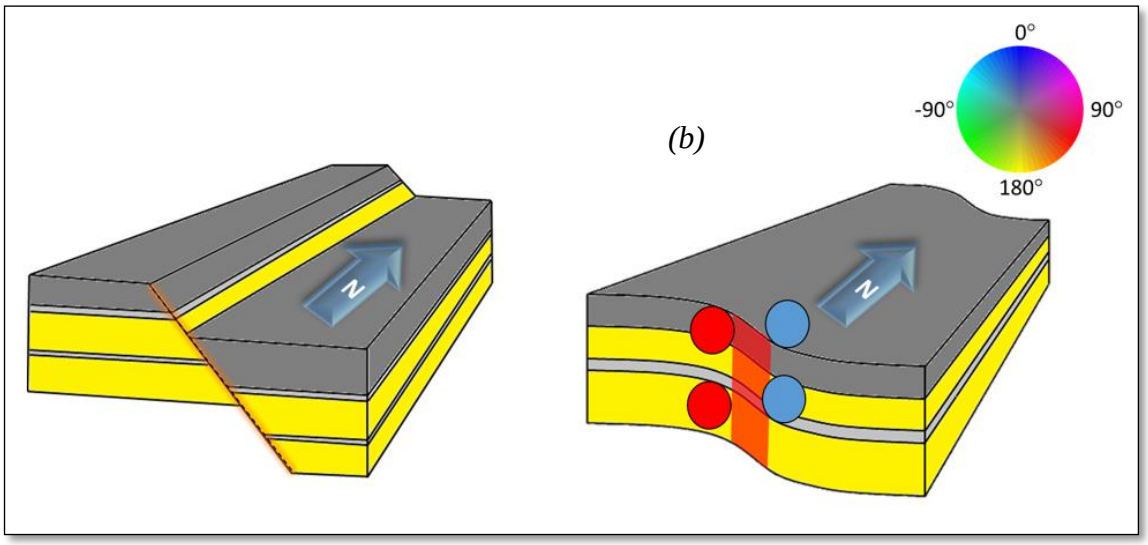

Figure 2.5. Cartoons of two different fault models, (a) a model where finite offset across a fault results in a strong coherence anomaly but no curvature or aberrancy anomaly. (b) a model where the offset is distributed over a zone of conjugate faults, such that the now continuous reflector no longer gives rise to a coherence anomaly. Positive curvature anomalies on the footwall are indicated by red circles, where negative curvature anomalies on the hanging wall indicated by the blue circles. Aberrancy measures the change in curvature which in this example is towards the east, and is displayed as a red-magenta aberrancy anomaly.

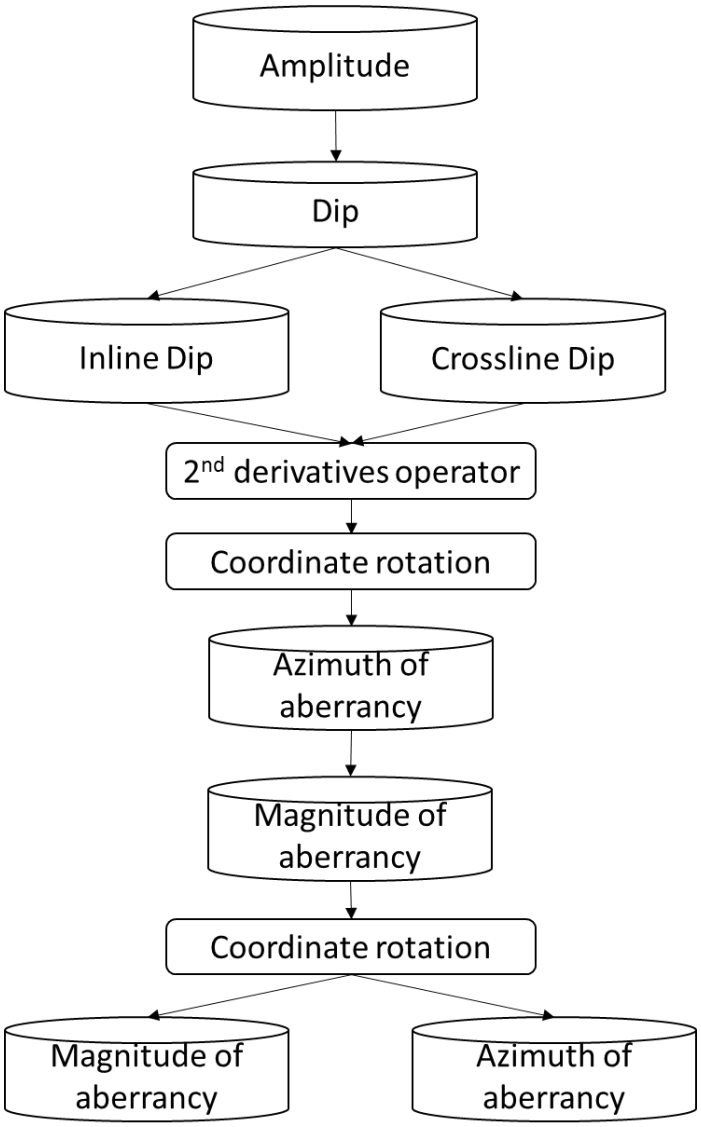

Figure 2.6. The internal steps of aberrancy computation. The first step is to compute the inline and crossline dip, which including the first, and second derivatives of inline and crossline dip. The second step is to rotate the original coordinate system, $x_0 - y_0 - z_0$, to the new coordinate system, $x_1 - y_1 - z_1$ by using the dip magnitude and dip azimuth. The third step is to find extrema of a cubic function, which compute the magnitude and azimuth of aberrancy. The final step is rotate the new coordinate sytem back to original coordinate system to get the correct aberrancy azimuth value.

(a)

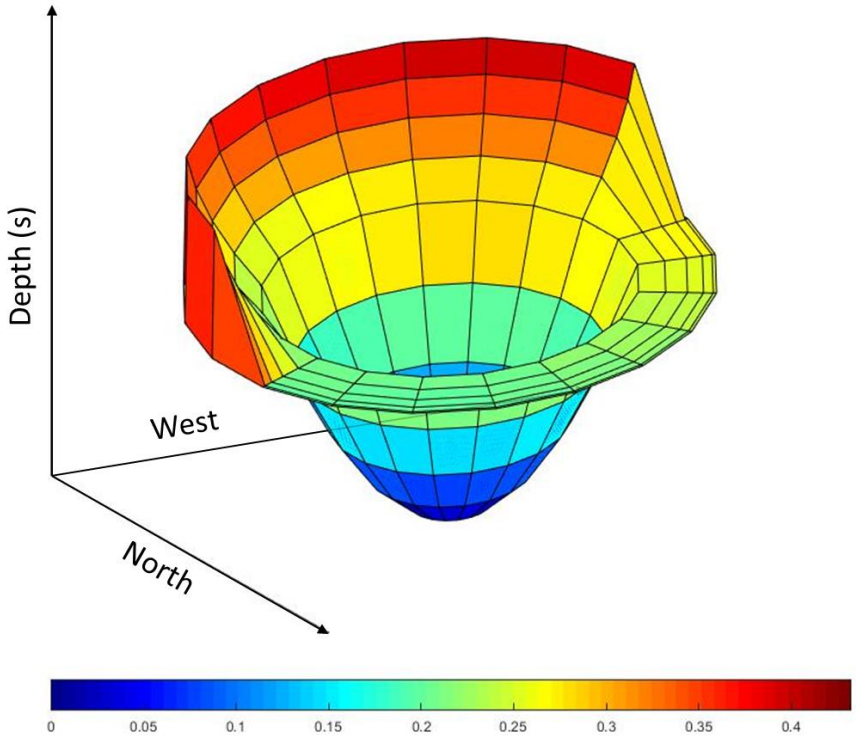

(b)

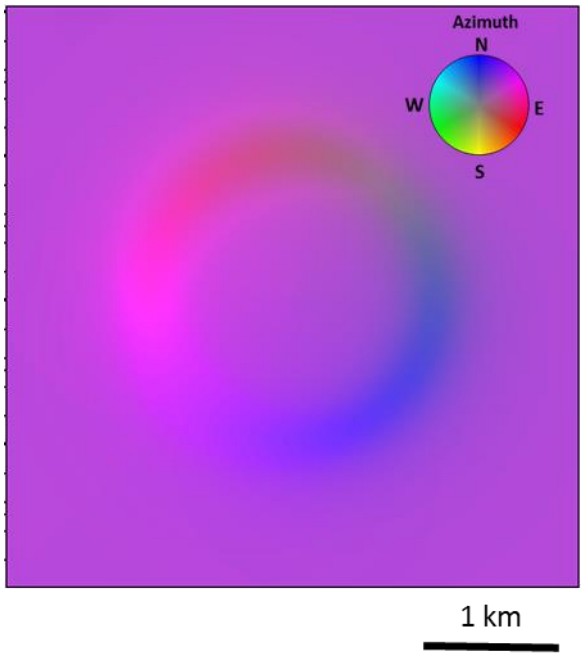

(c)

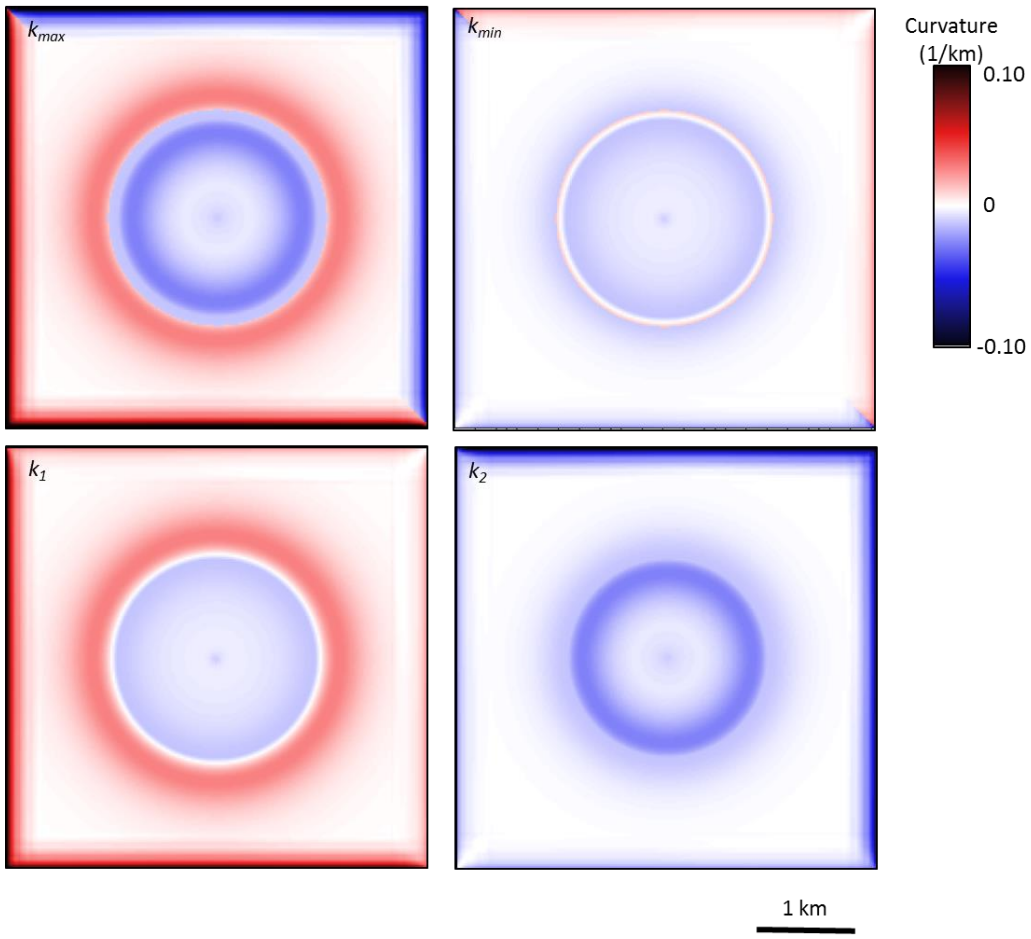

(d)

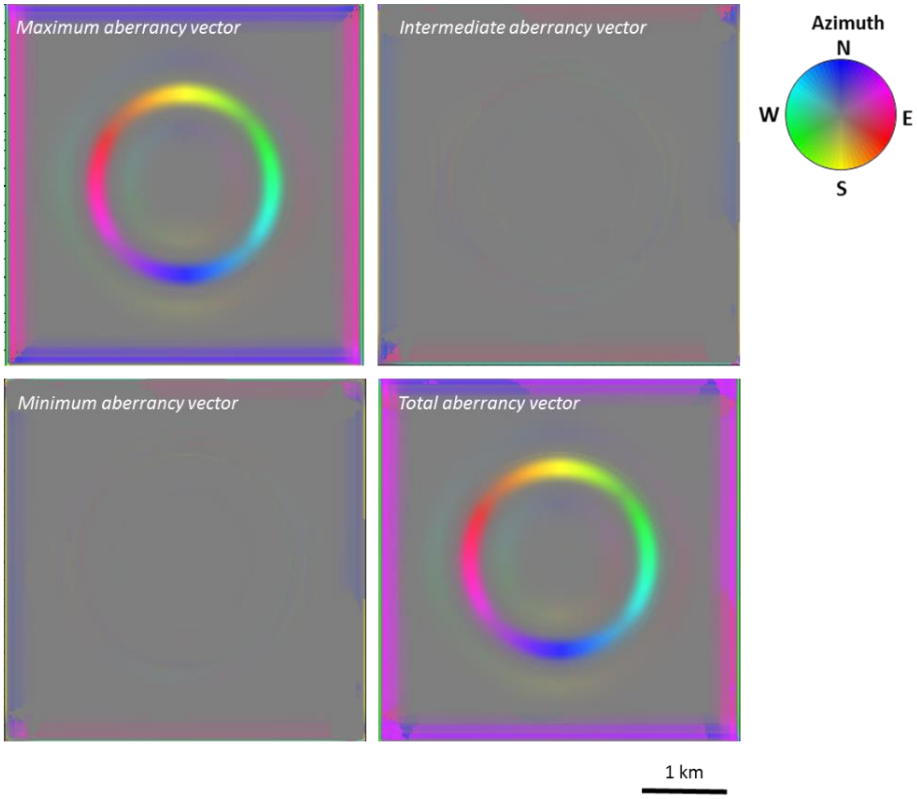

Figure 2.7. (a) Mesh grid showing a simple synthetic model in depth consisting of a circular sink hole embedded in a planar reflector dipping 2° to the northeast (b) Vector dip computed from the synthetic model shown in (a) The maximum dip of the sink is 2° such that the edge dips 4° to the NE in the SW portion of the sink hole and dips 0° or is nearly flat in the northeast portion of the sink hole. (c) Alternative means of displaying the two extreme curvature values computed from the synthetic shown in the previous figure. In this image, the minimum curvature carries little information, since the input model consists of parallel rather than crossing flexures. (d) Time slices through the aberrancy volumes corresponding to the synthetic dip and curvature images shown in the previous two figures. The total aberrancy is the vector sum of the maximum, intermediate, and minimum aberrancy vectors.

(a)

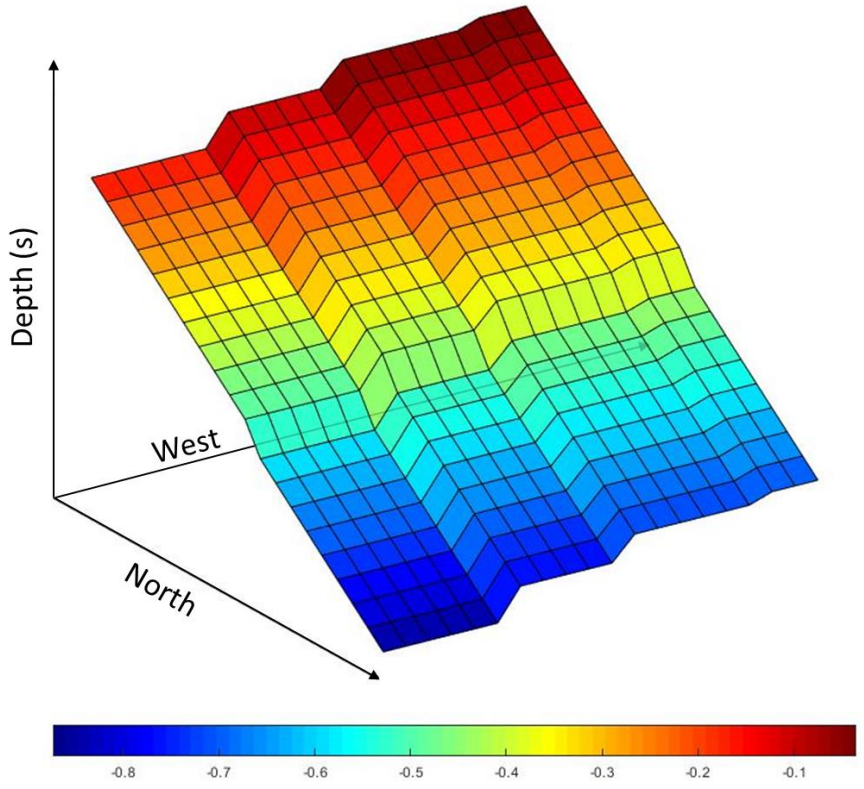

(b)

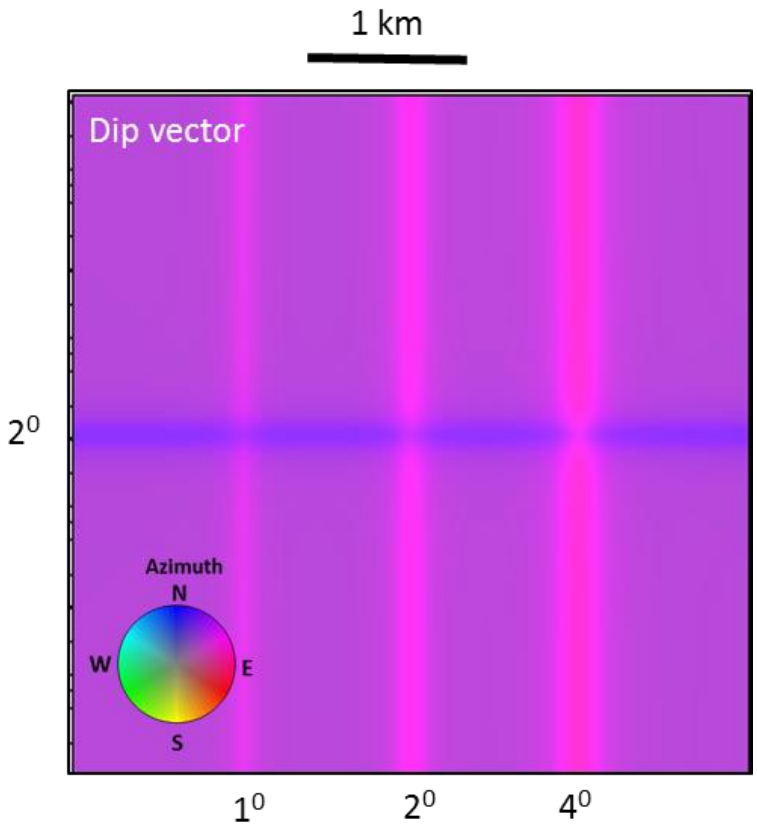

(c)

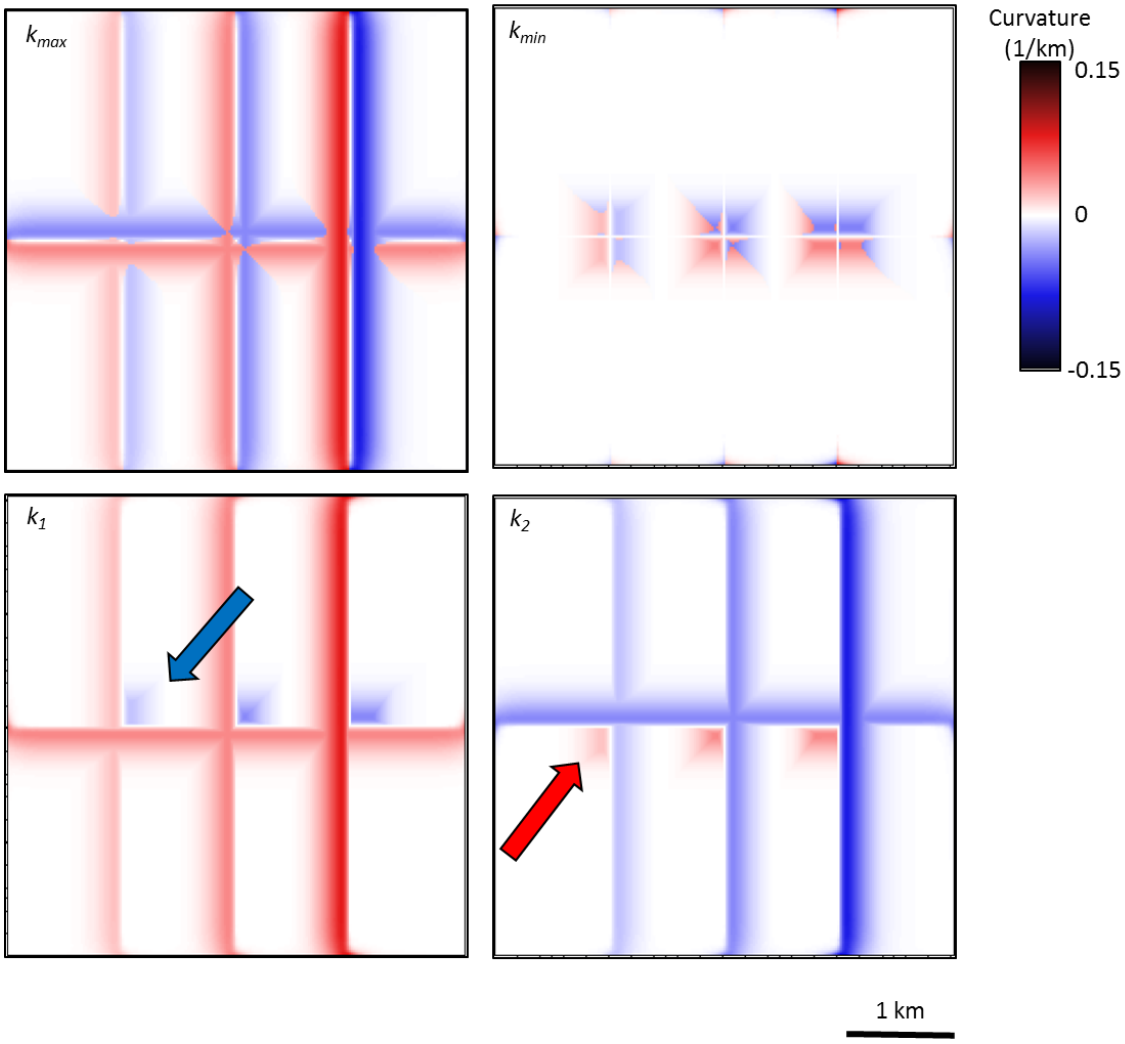

(d)

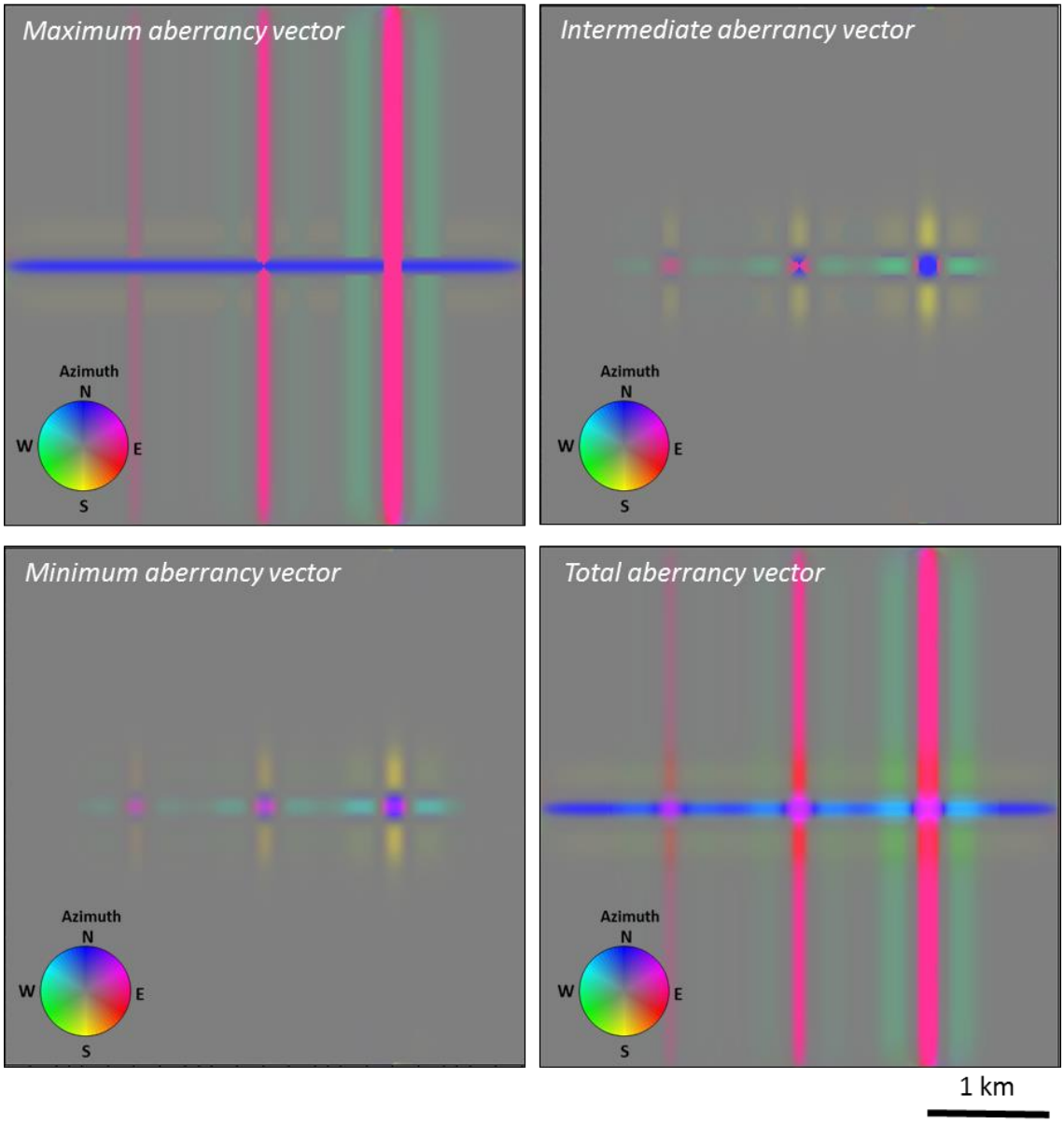

Figure 2.8. (a) Mesh grid showing a simple synthetic model in depth consisting of an EW-trending flexure and three NS-trending flexures. (b) Vector dip computed from the synthetic model shown in (a). The EW-trending flexure dipping to the North appearing as blue, and three NS-trending flexures dipping towards the east and appearing as red-magenta. The maximum dip for each of the NS flexures is 1°, 2°, and 4°, crossing the EW flexure with maximum dip of 2°. (c) Alternative means of displaying the two extreme curvature values computed from the synthetic shown in the previous figure. (d) Time slices through the aberrancy volumes corresponding to the synthetic dip and curvature images shown in the previous two figures. The total aberrancy is the vector sum of the maximum, intermediate, and minimum aberrancy vectors.

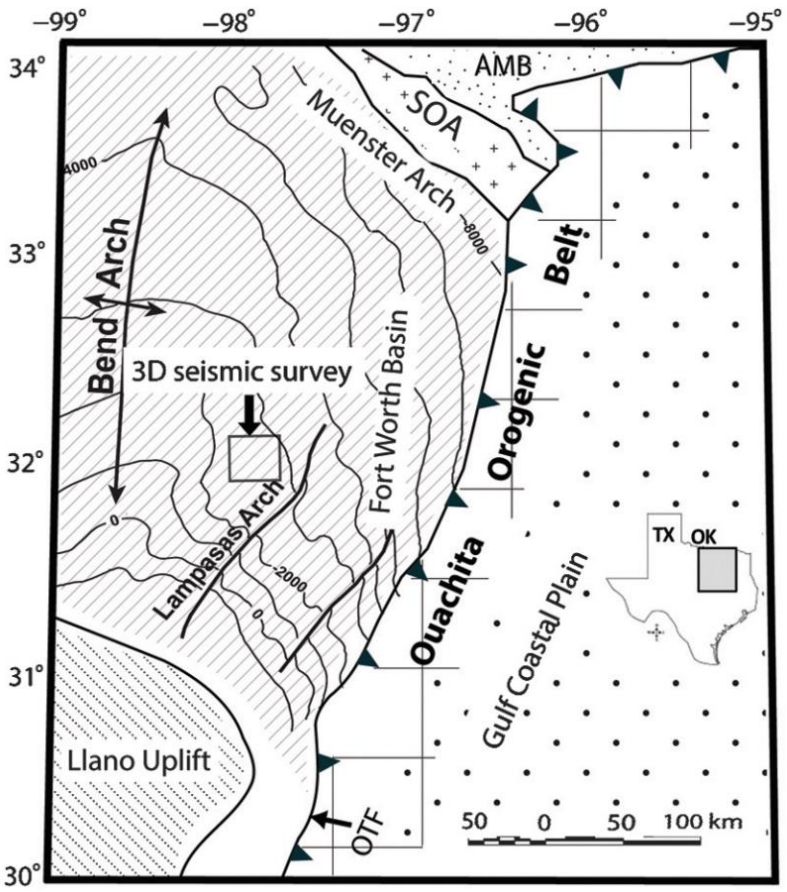

Figure 2.9. Index map of FWB and major tectonic units (modified after Khatiwada et al., 2013) corresponding to the gray square on the map of Texas.

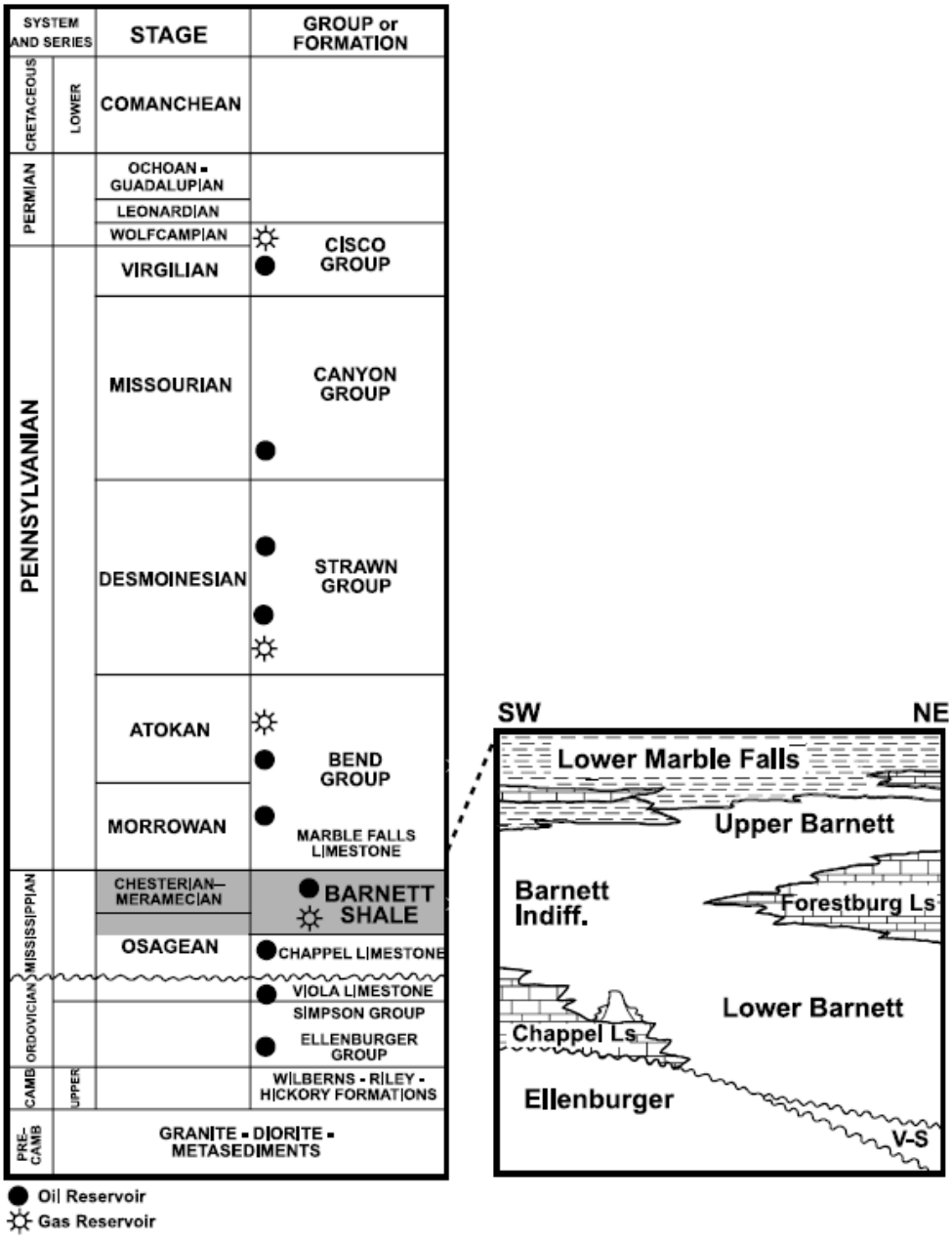

Figure 2.10. Generalized stratigraphic column (modified from Montgomery et al., 2005).

(a)

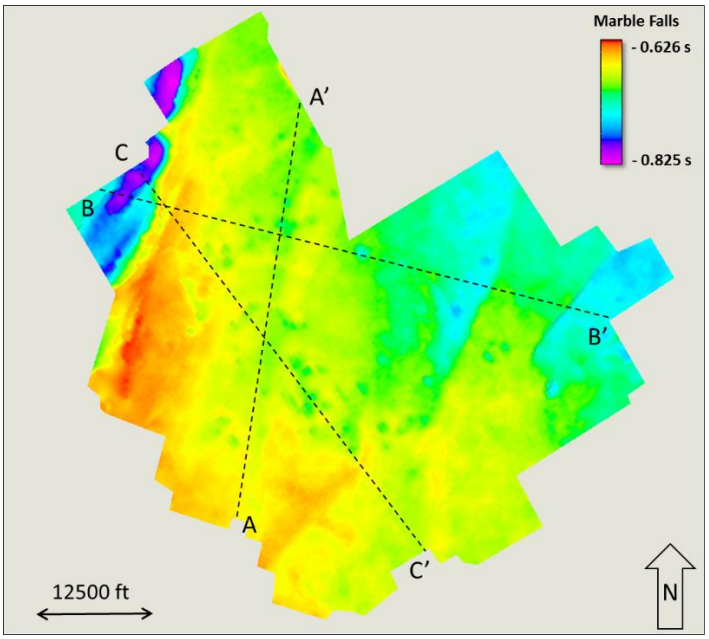

(b)

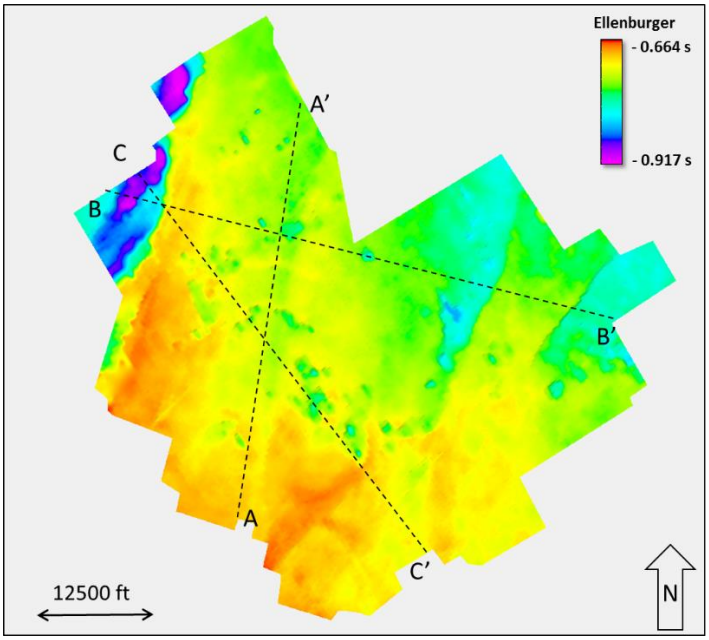

Figure 2.11. (a) Time structure maps of the top Marble Falls and (b) Ellenburger horizons with three crossline AA', BB', and CC'. Vertical slices AA', BB', and CC' will be discussed in subsequent figures.

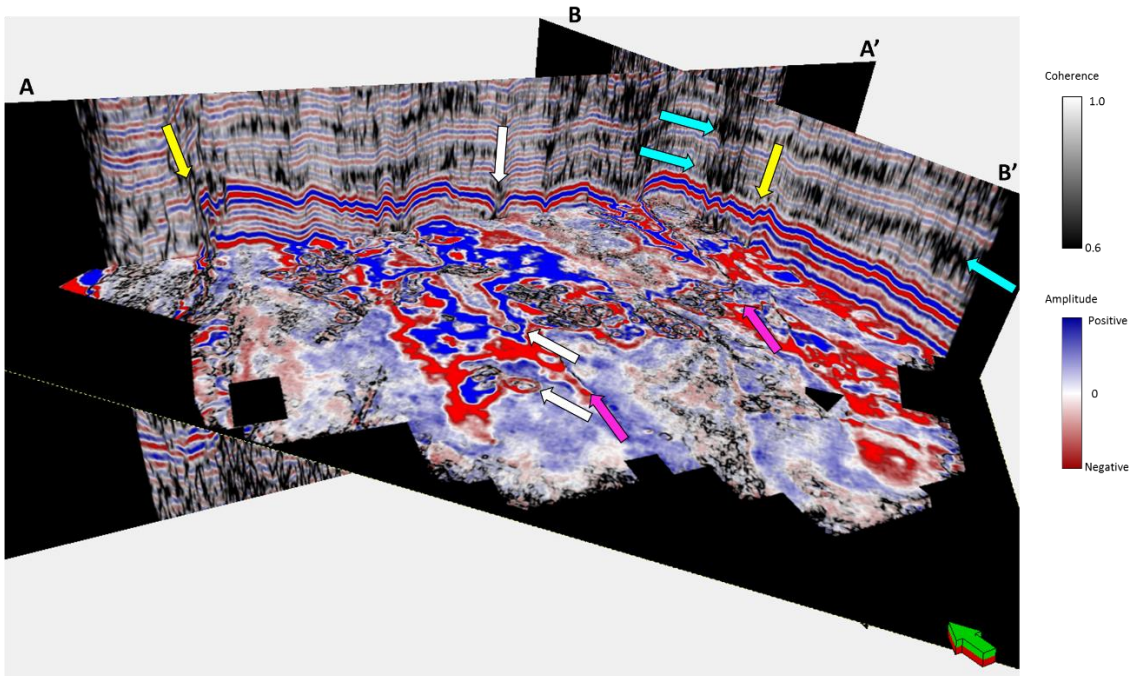

Figure 2.12. Vertical slices AA' and BB' through the Barnett Shale interval through the co-rendered seismic amplitude and coherence volumes. Time slice at the Barnett Shale level (t = 0.726) through the coherence volume. Yellow arrows indicate two faults delineated on the lines AA' and BB' that continue into the time slice. Even though the seismic amplitude data have been preconditioned, there are several strata-bound low coherence anomalies (cyan arrows), some of which are associated with deeper collapse features (white arrows), and others with low signal-to-noise ratio.

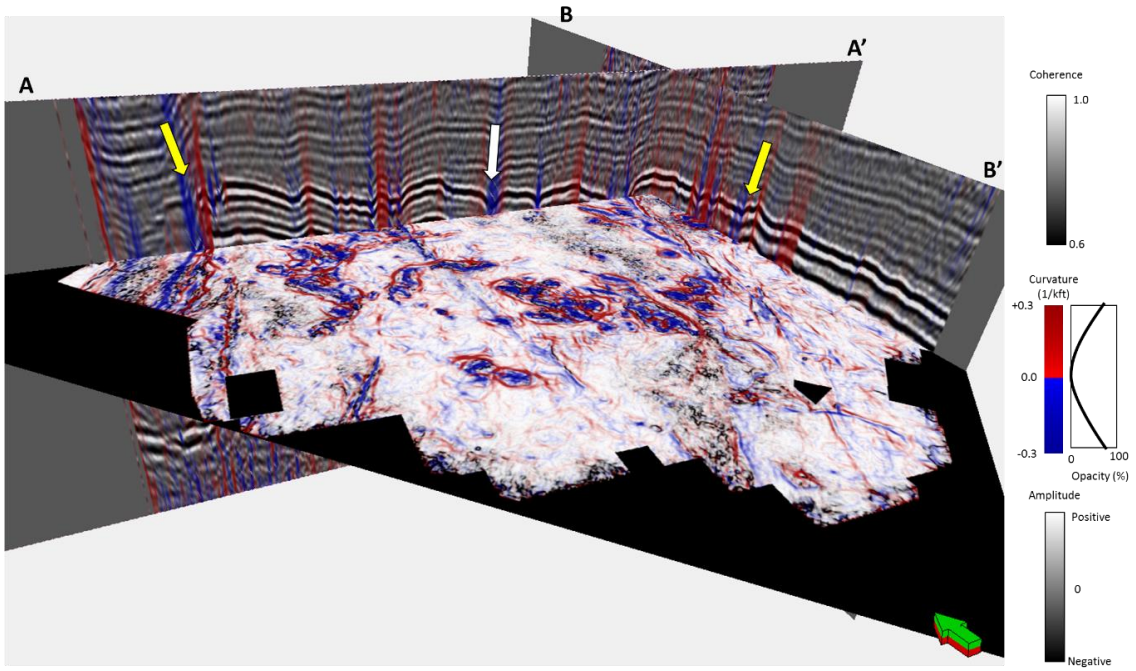

Figure 2.13. The same slices shown in the previous figure, but now through the co-rendered most-positive and most-negative curvature with seismic amplitude on the vertical slices and with coherence on the time slice. The yellow arrows indicate the same faults shown indicated in the previous image. The White arrow points deeper collapse features.

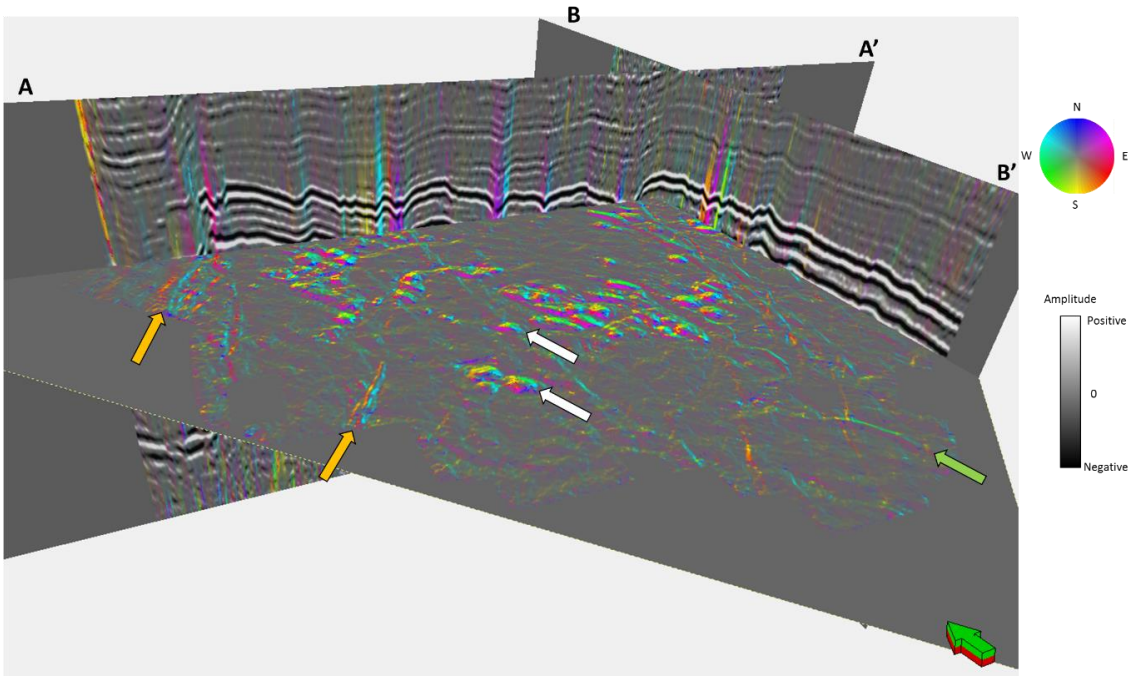

Figure 2.14. The same slices shown in the previous two figures through the total aberrancy volume. Note the continuous flexures cutting through the time slice. Orange arrows indicate couplets, defining the edges of small grabens by a NW-oriented (cyan) flexure on one side and a SE-oriented (orange) flexure on the other. The green arrow indicates a graben delineated by a NE-oriented (magenta) on one side and a SW-oriented (lime green) flexure on the other. Several of the collapse features exhibit flexures that cycle the color wheel (white arrows).

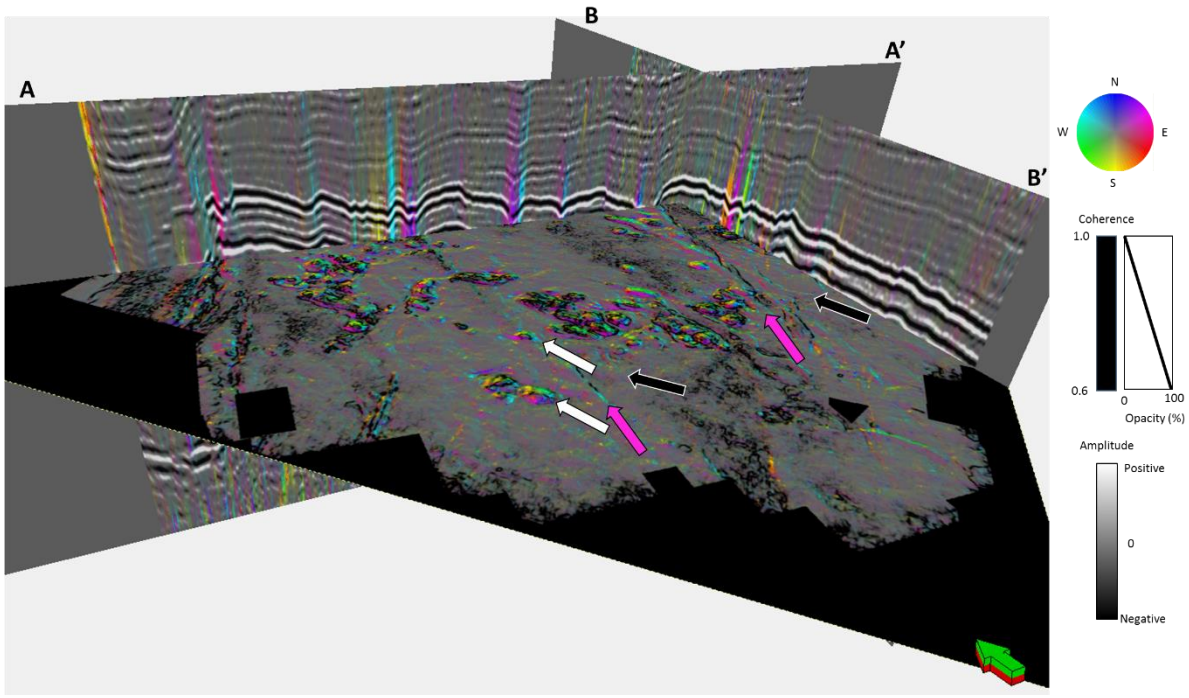

Figure 2.15. The same slices as the previous four figures, but now with the time slice through co-rendered aberrancy vector and coherence volumes. The magenta arrows indicate the same two faults shown in the previous image. The flexures indicated by the black arrows exhibit a different azimuth, suggesting trans-tensional deformation. In this example, coherence is complementary to aberrancy, providing additional insight into the interpretation. White arrows indicate the same two collapse features shown in previous images. In this example, aberrancy confirms an interpretation already made by examining coherence alone.

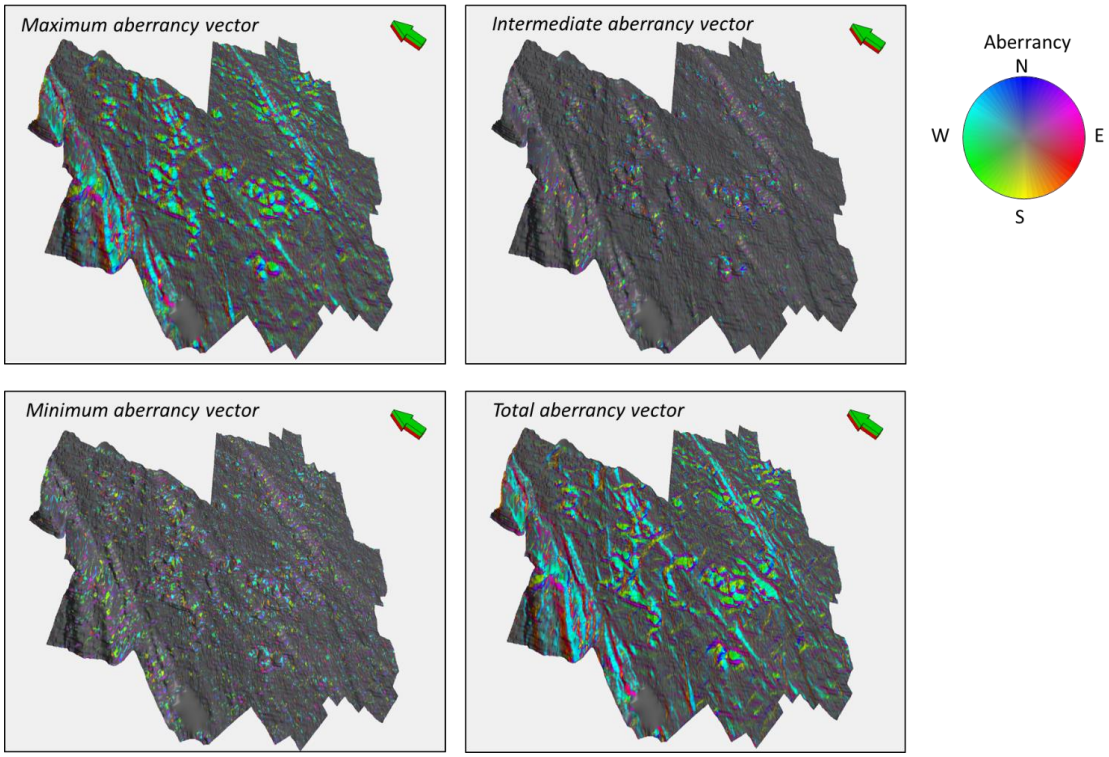

Figure 2.16. Horizon slices along the top Marble Falls through the aberrancy volumes. The total aberrancy is the vector sum of the maximum, intermediate, and minimum aberrancy vectors. We find the total aberrancy vector to be most useful for structural interpretation; however, the intermediate and minimum aberrancy indicate zones of conflicting flexure, and depending on the tectonic model, may potentially indicate areas of more intense natural fracturing.

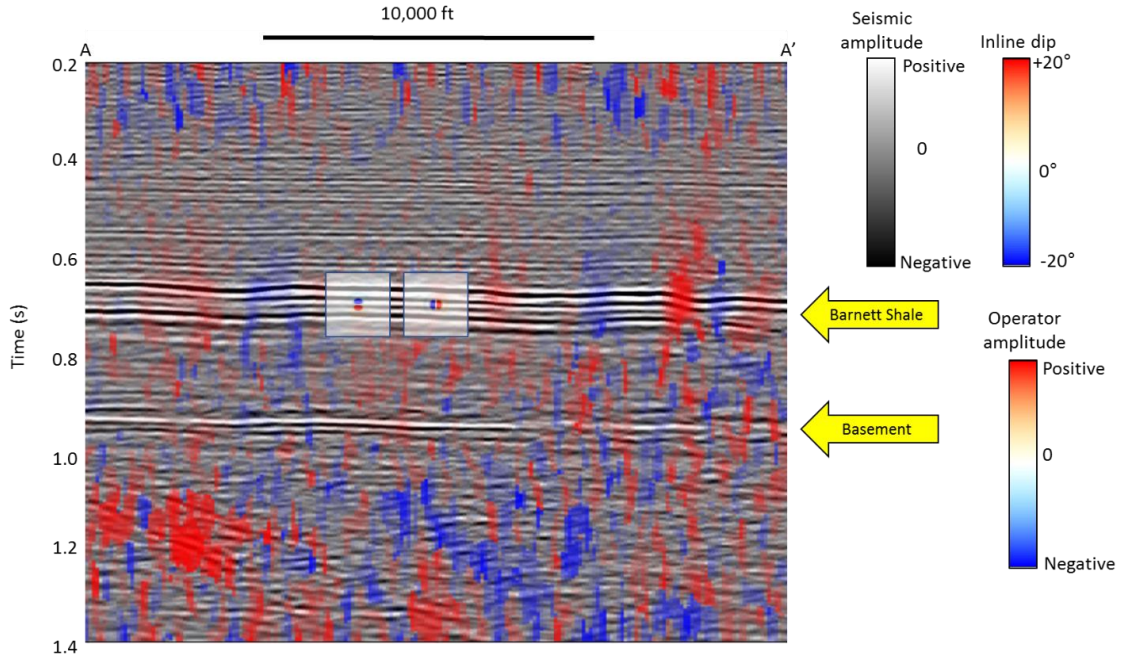

Figure 2.17. Vertical slice along line AA' through seismic amplitude co-rendered with the inline component of vector dip at approximately 1:1 vertical to horizontal aspect ratio, showing the data quality. Location of line shown in the Figure 2.18. There is strong acquisition footprint in the shallow section at t = 0.3 s , resulting in vertical stripes in inline dip. In contrast, the inline dip estimated at the target Barnett Shale level at t = 0.7 s exhibits high signal-to-noise. The top of the basement is at t = 0.9 s in this image. Below this level, the reflectors become less continuous, resulting in a noisier estimation of the inline dip component. The vertical (left square inset) and inline (right square inset) derivative operators show the extent of what we call a "long wavelength" operator. Since the bin size is 110 ft by 110 ft, the crossline derivative operator (not shown) is a rotated version of the inline derivative operator for this data volume.

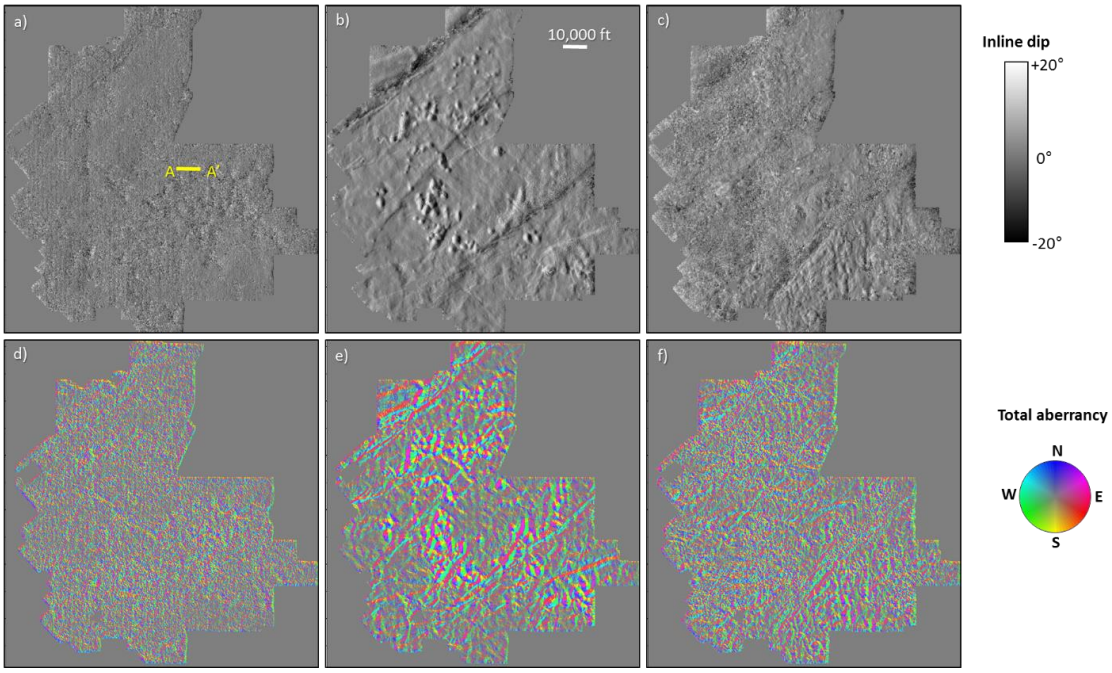

Figure 2.18. Time slices at (a) t = 0.3 s, (b) t = 0.7 s, and (c) t = 1.0 s through the inline component of the dip vector. The line AA' indicates the location of the vertical slice through the same volume shown in the previous figure. Time slices through total vector aberrancy at (d) t = 0.3 s, (e) t = 0.7 s, and (f) t = 1.0 s. Because aberrancy is the second derivative of the two dip components, the time slice in (d) exhibits acquisition footprint while the time slice in (f) is noisy due to the poorly imaged basement reflectors. In contrast, the time slice in (e) at the target level exhibits high signal-to-noise and accurate delineates both faulting and karsting.

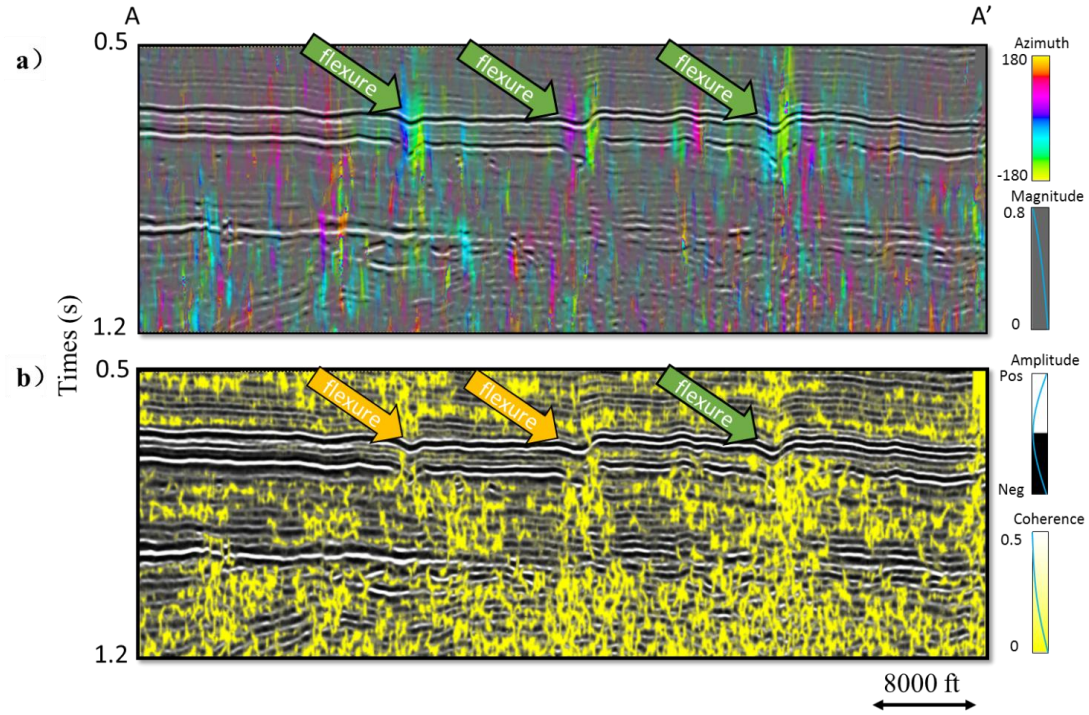

Figure 2.19. Vertical slices along line AA' through (a) aberrancy and (b) coherence. Arrows indicate anomalies along the top Marble Falls that are better resolved by aberrancy.

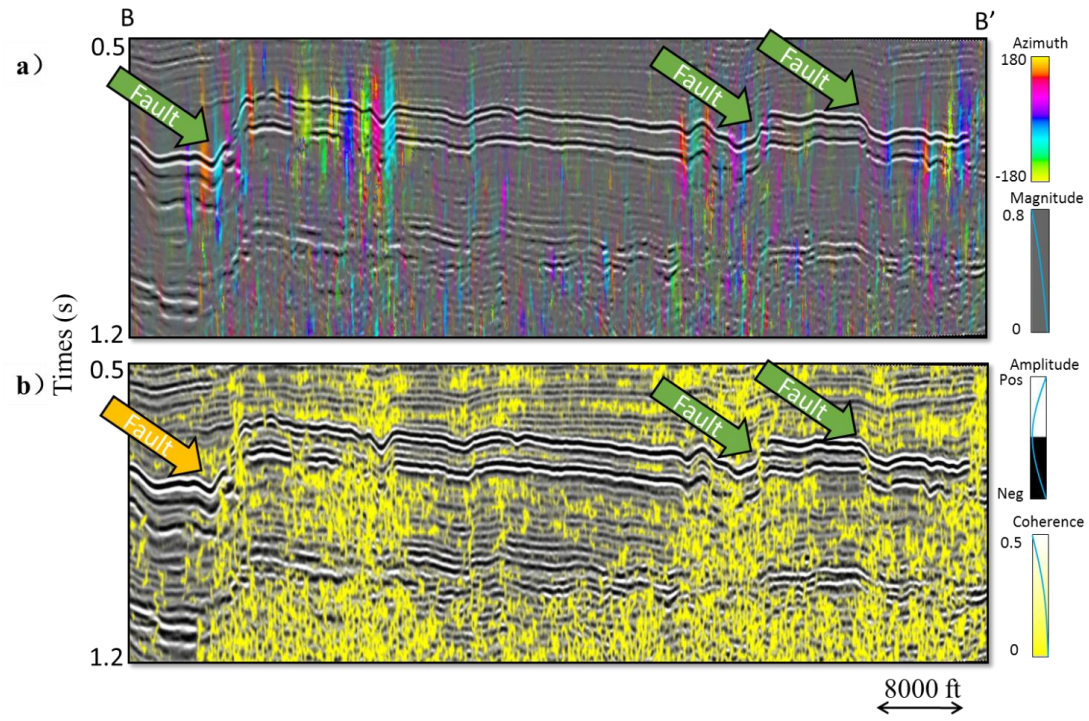

Figure 2.20. Vertical slices along line BB' through (a) aberrancy and (b) coherence. Arrows indicate anomalies along the top Marble Falls that are better resolved by aberrancy. The faults in the aberrancy image appear as relatively thin, vertically continuous vertical thin lines but as less continuous stair step blotches in coherence.

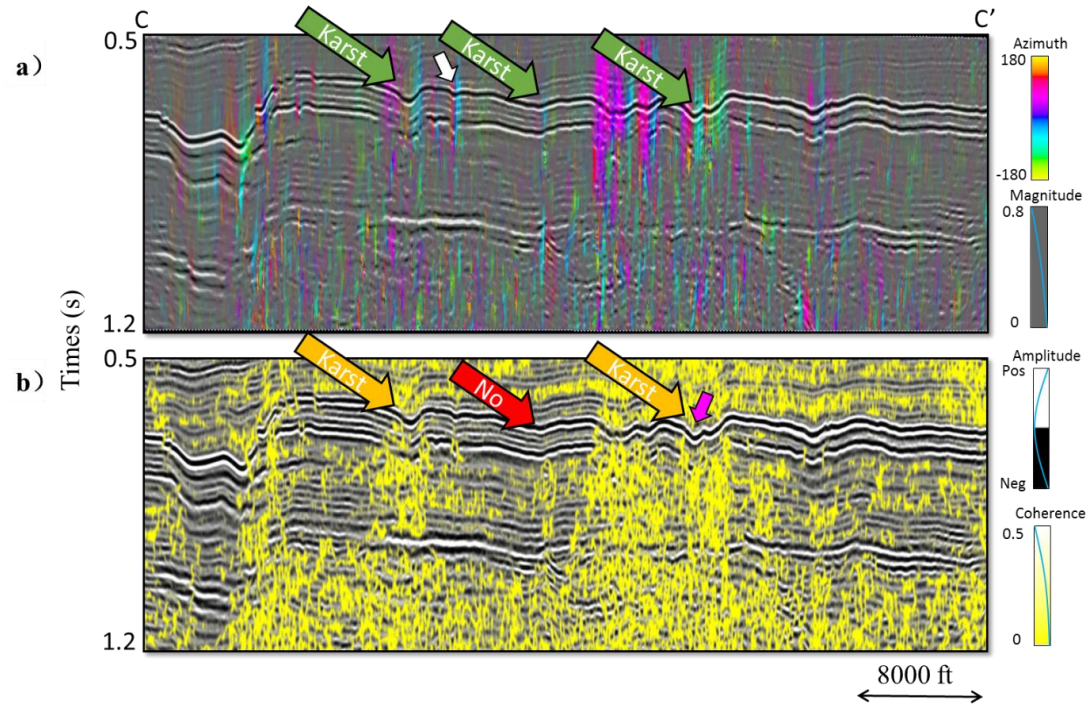

Figure 2.21. Vertical slices along line CC' through (a) aberrancy and (b) coherence through several collapse features. Arrows indicate anomalies along the top Marble Falls that are better resolved by aberrancy. The flexure indicated by the magenta arrow in (b) exhibits a 19 ms offset over a distance of 260 ft, while the more subtle flexure indicated by the white arrow in (a) exhibits only a 8 ms offset over 260 ft.

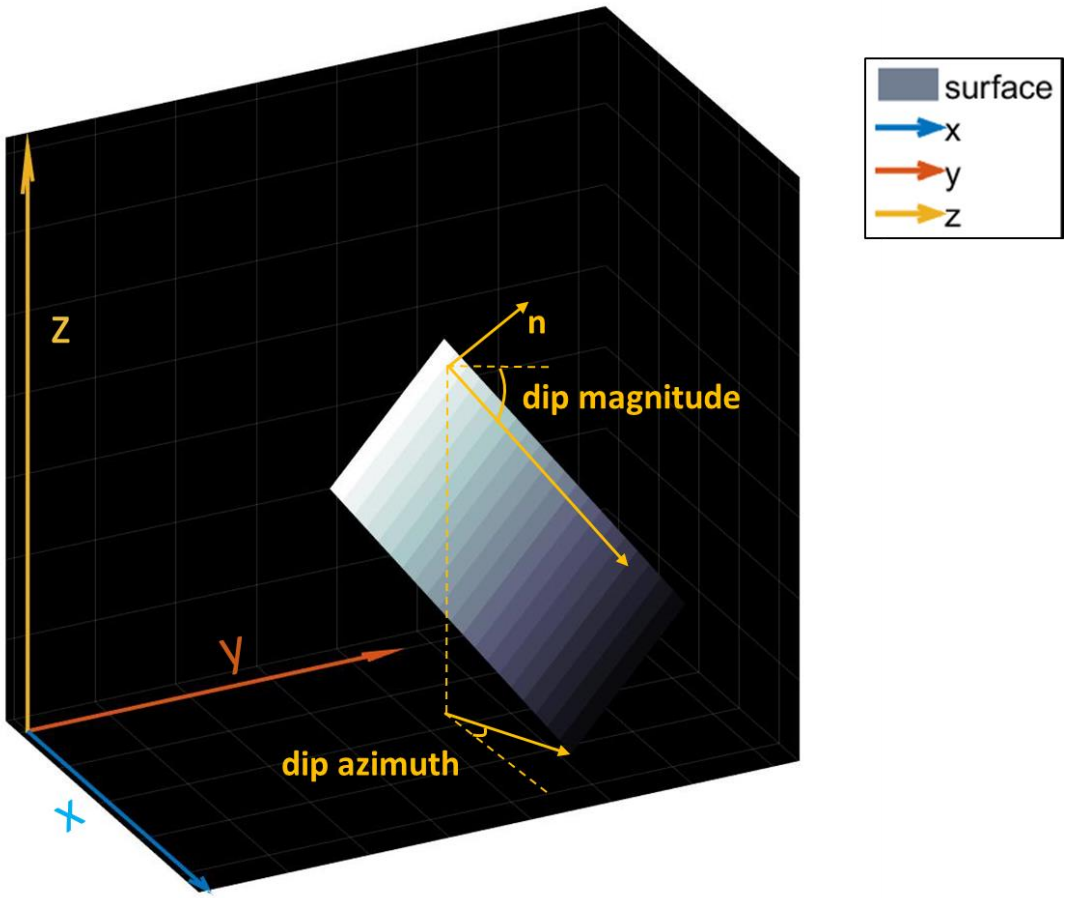

Figure A-1. Schematic diagram showing a reflector surface, z(x,y) (in gray) along with dip magnitude, dip azimuth, and the unit vector **n** normal to the reflector surface.

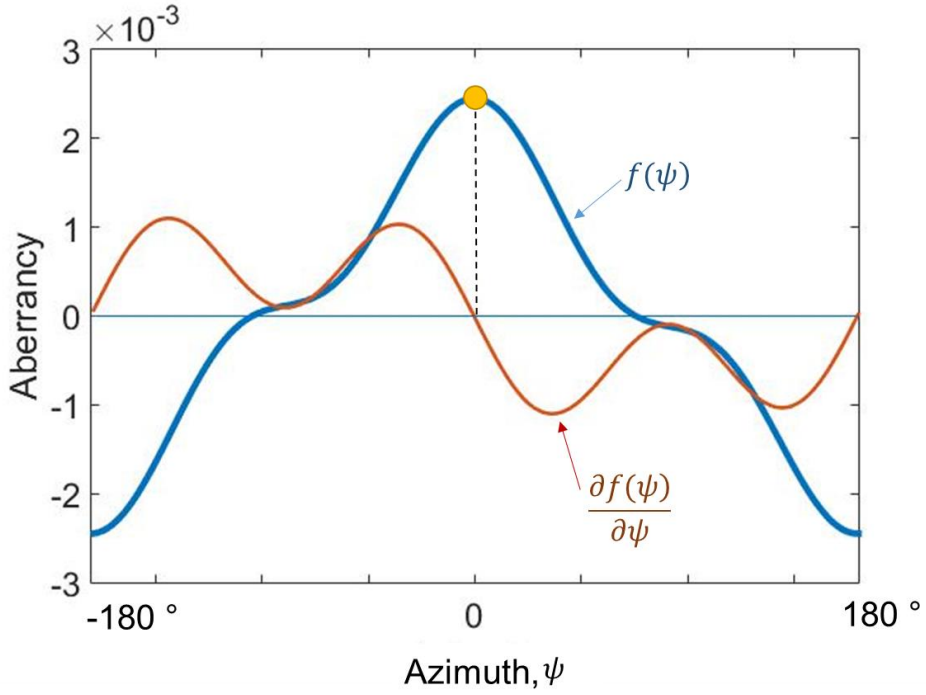

Figure B-1. Flexure $f(\psi)$ showing one independent extremum.

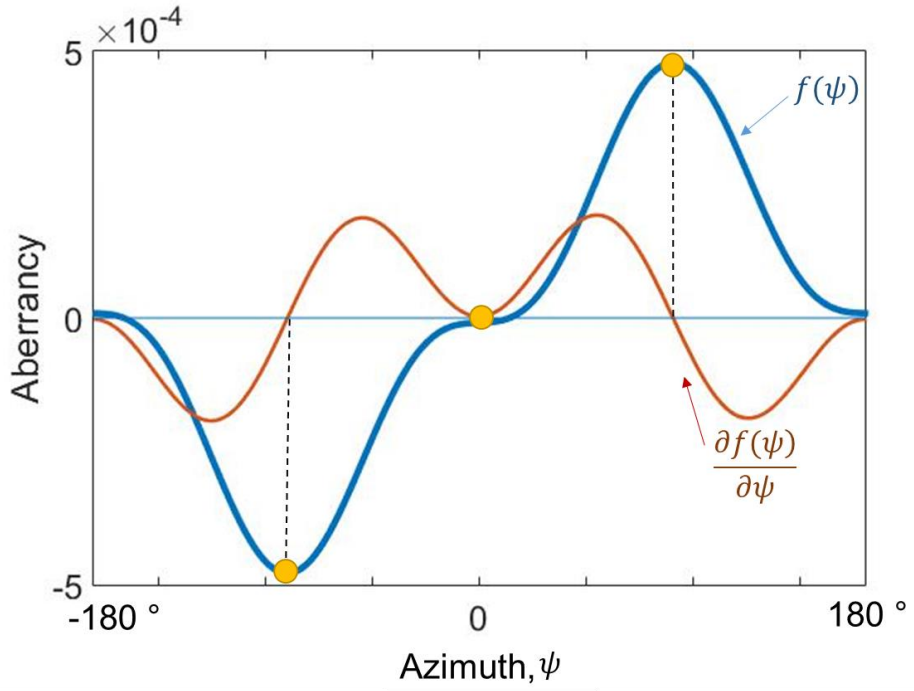

Figure B-2. Flexure $f(\psi)$ showing two independent extrema.

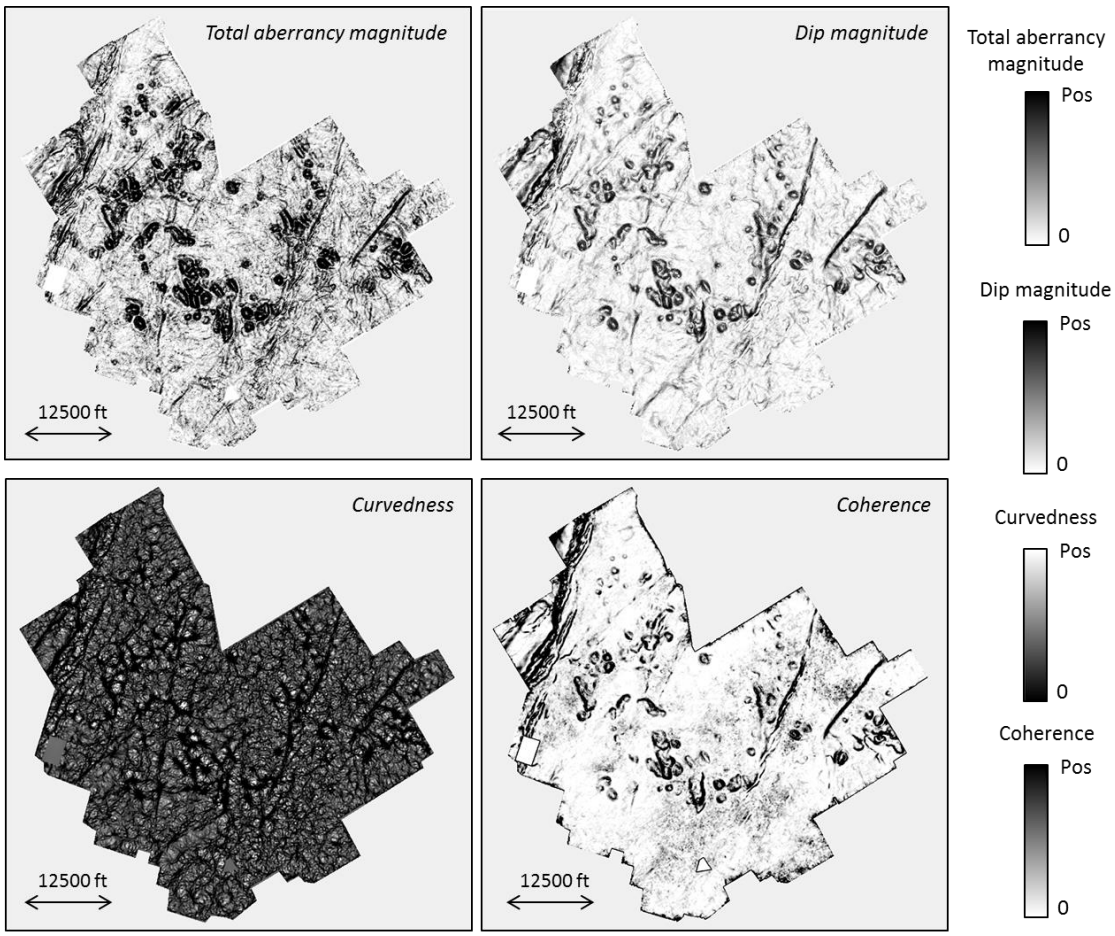

Figure C-1. Horizon slices along the top Marble Falls through the total aberrancy magnitude, dip magnitude, curvedness, and the coherence volume. The total aberrancy is the vector sum of the maximum, intermediate, and minimum aberrancy vectors.

(a)

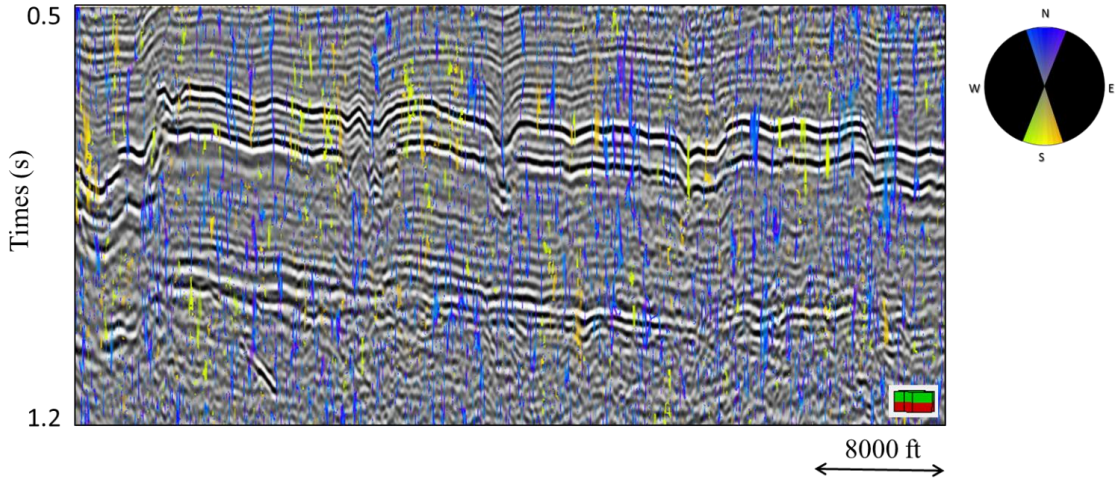

(b)

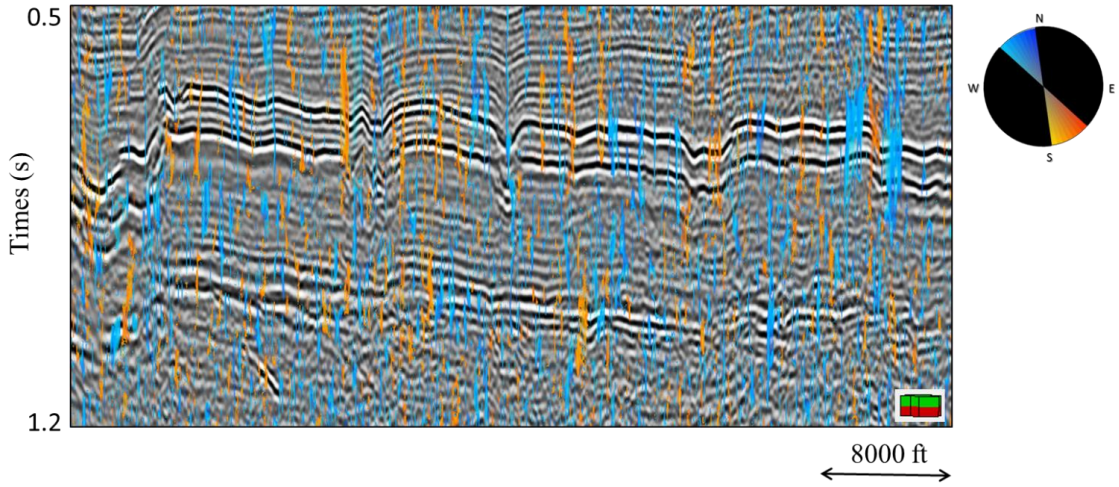

(c)

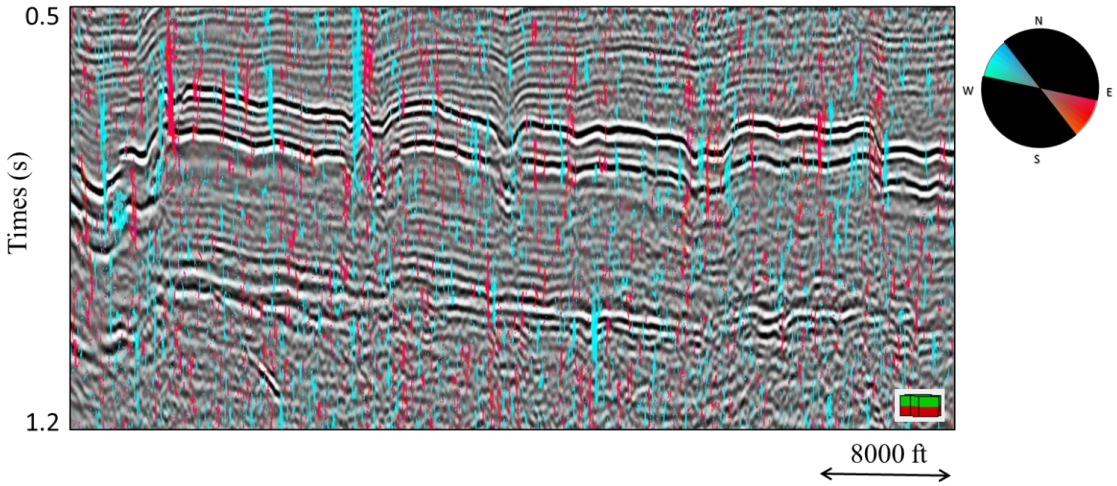

(d)

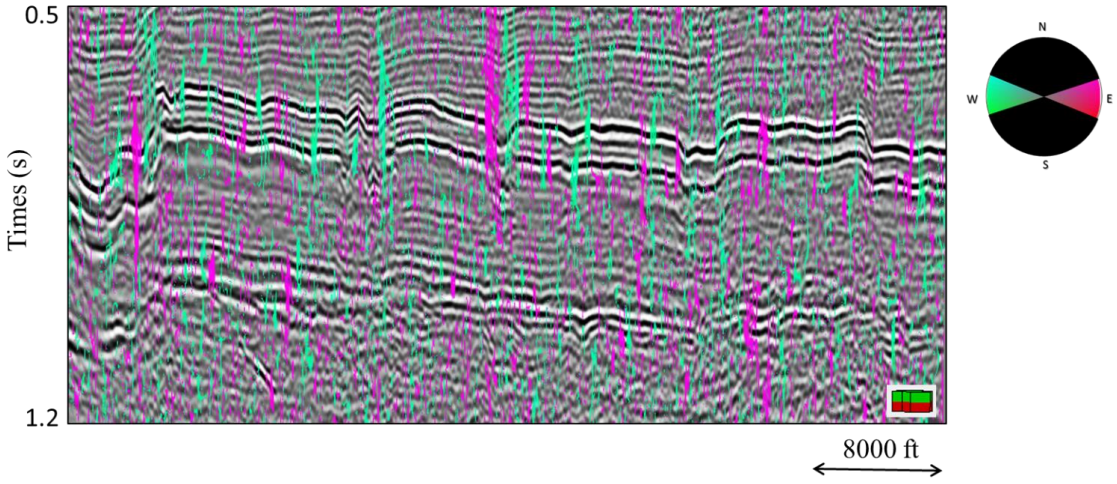

(e)

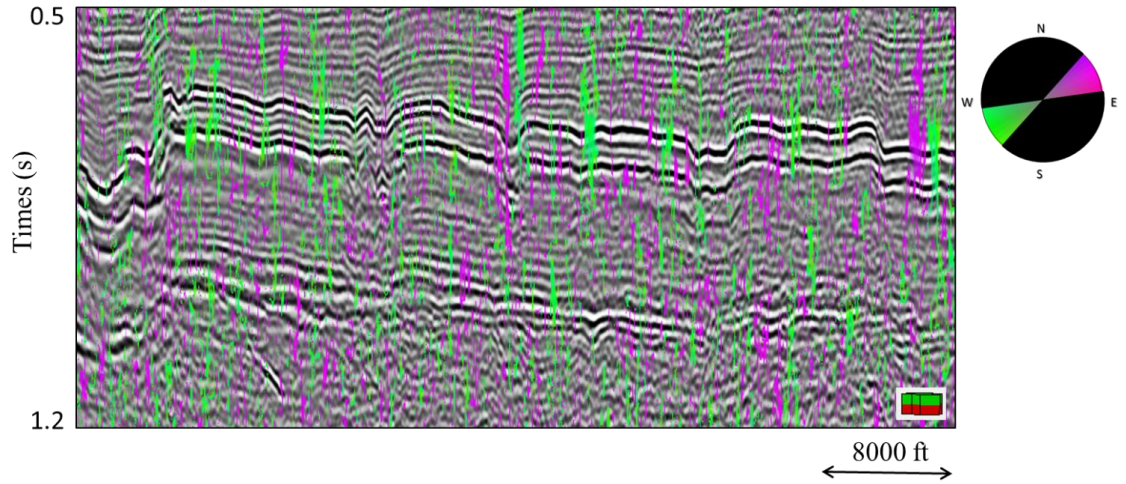

(f)

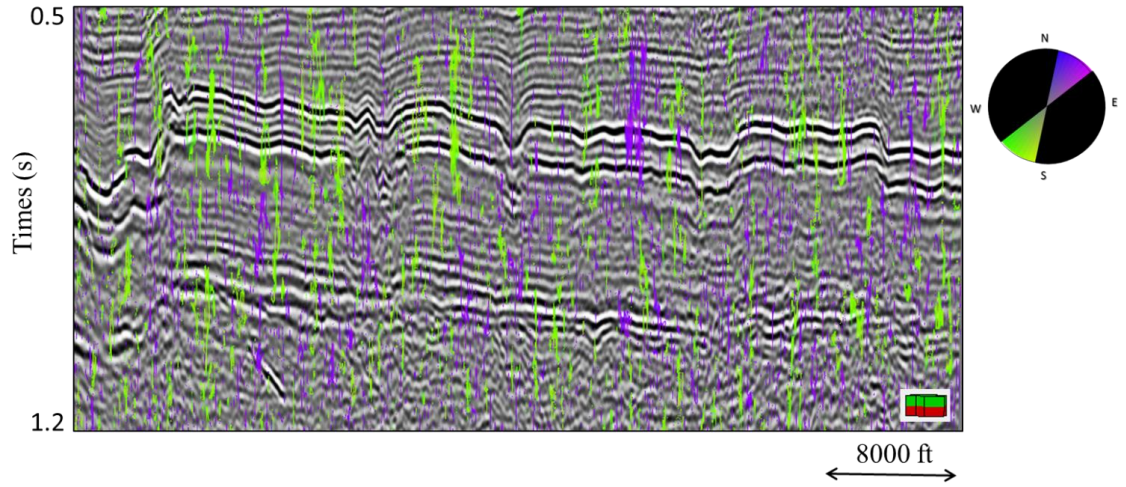

Figure D-1. Because each aberrancy anomaly is described by a magnitude and an azimuth, one can generate a suite of apparent aberrancy by either explicitly filtering the attribute volumes, or as shown in this suite of six images at 30° increments, using opacity resulting in image that show flexure trending at (a) 0° and -180°, (b) 30° and -150°, (c) 60° and -120°, (d) 90° and -90°, (e) 120° and -60°, and (f) 150° and -30°.

REFERENCES

Bahorich, M., and S. Farmer, 1995, 3-D seismic discontinuity for faults and stratigraphic features: The coherence cube: The Leading Edge, **14**, 1053–1058, doi:10.1190/1.1437077.

Borwein, P., and T. Erdélyi, 2012, Polynomials and polynomial inequalities: Springer-Verlag New York, 480 p., doi:10.1007/978-1-4612-0793-1.

Bruner, K. R., and R. Smosna, 2011, A comparative study of the Mississippian Barnett Shale, Fort Worth Basin, and Devonian Marcellus Shale, Appalachian Basin, in Technical Report DOE/NETL/2011/1478: National Energy Technology Laboratory for the United States Department of Energy.

Chopra, S., and K. J. Marfurt, 2005, Seismic attributes — A historical perspective: Geophysics, **70**, 3SO–28SO, doi:10.1190/1.2098670.

Chopra, S., and K. Marfurt, 2007a, Seismic attributes for prospect identification and reservoir characterization: Society of Exploration Geophysicists and European Association of Geoscientists and Engineers, doi:10.1190/1.9781560801900.

Chopra, S., and K. J. Marfurt, 2007b, Volumetric curvature attributes add value to 3D seismic data interpretation: The Leading Edge, **26**, 856–867, doi:10.1190/1.2756864.

Di, H., and D. Gao, 2014, A new algorithm for evaluating 3D curvature and curvature gradient for improved fracture detection: Computers & Geosciences, **70**, 15–25, doi:http://dx.doi.org/10.1016/j.cageo.2014.05.003.

Di, H., and D. Gao, 2016, Improved estimates of seismic curvature and flexure based on 3D surface rotation in the presence of structure dip: Geophysics, **81**, IM13-IM23, doi:10.1190/geo2015-0258.1.

Einstein, A., L. Infeld, and B. Hoffmann, 1938, The Gravitational Equations and the Problem of Motion: Annals of Mathematics, **39**, 65–100, doi:10.2307/1968714.

Fan, S., 1989, A new extracting formula and a new distinguishing means on the one variable cubic equation: J. Hainan Teach. Coll, **2**, 91–98.

Gao, D., 2013, Integrating 3D seismic curvature and curvature gradient attributes for fracture characterization: Methodologies and interpretational implications: Geophysics, **78**, O21–O31, doi:10.1190/geo2012-0190.1.

Gao, D., and H. Di, 2015, Extreme curvature and extreme flexure analysis for fracture characterization from 3D seismic data: New analytical algorithms and geologic implications: Geophysics, **80**. IM11-IM20, doi:10.1190/geo2014-0185.1.

Joshi, P., and C. Séquin, 2010, An Intuitive Explanation of Third-order Surface Behavior: Comput. Aided Geom. Des., **27**, 150–161, doi:10.1016/j.cagd.2009.11.003.

Khatiwada, M., G. R. Keller, and K. J. Marfurt, 2013, A window into the Proterozoic: Integrating 3D seismic, gravity, and magnetic data to image subbasement structures in the southeast Fort Worth basin: Interpretation, **1**, T125–T141, doi:10.1190/INT-2013-0041.1.

Marfurt, K. J., 2006, Robust estimates of 3D reflector dip and azimuth: Geophysics, **71**, P29–P40, doi:10.1190/1.2213049.

Montgomery, S. L., D. M. Jarvie, K. A. Bowker, and R. M. Pollastro, 2005, Mississippian Barnett Shale, Fort Worth basin, north-central Texas: Gas-shale play with multi--trillion cubic foot potential: AAPG bulletin, **89**, 155–175.

Qi, J., B. Zhang, H. Zhou, and K. Marfurt, 2014, Attribute expression of fault-controlled karst — Fort Worth Basin, Texas: A tutorial: Interpretation, **2**, SF91-SF110, doi:10.1190/INT-2013-0188.1.

Rich, J., and K. Marfurt, 2013, Curvature gradient attributes for improved fault characterization, 83rd annual international meeting of the SEG Expanded Abstracts: 1319–1323, doi:10.1190/segam2013-1290.1.

Schot, S. H., 1978, Aberrancy: Geometry of the Third Derivative: Mathematics Magazine, **51**, 259–275, doi: 10.2307/2690245.

Schuelke, J. S., 2011, Overview of seismic attribute analysis in shale plays: GCSSEPM 31st Annual Bob. F. Perkins Research Conference on Seismic attributes – New views on seismic imaging: Their use in exploration and production, 806-827.

APPENDIX A: COMPUTATION OF DERIVATIVES IN A ROTATED COORDINATE SYSTEM

Reflector dip and the unit normal

Seismic interpreters commonly define reflector dip vector, **u**, in terms of an inline dip component, p_1, and crossline dip component, p_2, for time migrated data in units of s/km or s/kft

$$\mathbf{u} = \hat{\mathbf{x}}_1 p_1 + \hat{\mathbf{x}}_2 p_2 + 1. \tag{A-1}$$

In this appendix we will assume the x_1-axis of the survey to be North, and the x_2 axis to be East, with all azimuths, φ, measured clockwise from North. Other survey orientations require additional rotations before any of the rotations described below. Computation of curvature and aberrancy requires the conversion of such dips to the depth domain, either through depth migration, depth conversion of a time-migrated data volume, or more commonly, using a single conversion velocity, resulting in the units of p_1 and p_2 being dimensionless (or more explicitly, in km/km or kft/kft), much as a roofer measures the pitch when installing a new roof. Thus, p_1 measures how many units down the horizon goes for every unit traversed in the x, direction, and p_2 how many units down the horizon goes for every unit traversed in the y direction. The definition of a vector requires a third component, which is a measure of how many units down one goes for every unit traversed in the x_3 direction. This last value, which is not always obvious, is identically 1.0 for all dips.

Given these definitions, the unit normal to the reflector surface, $\mathbf{n} = (n_1, n_2, n_3)$, where the axes are chosen such that $n_3 \geq 0$ (Figure A-1), is then

$$\mathbf{n} = \begin{pmatrix} n_1 \\ n_2 \\ n_3 \end{pmatrix} = \frac{1}{\left(p_1^2 + p_2^2 + 1^2\right)^{1/2}} \begin{pmatrix} p_1 \\ p_2 \\ 1 \end{pmatrix}. \qquad \text{(A-2)}$$

After depth conversion of the vector **p**, the reflector dip magnitude θ and dip azimuth φ are

$$\theta = \mathrm{ACOS}\left[\frac{1}{\left(p^2 + q^2 + 1^2\right)^{1/2}} \right] , \qquad \text{(A-3a)}$$

and

$$\varphi = \mathrm{ATAN2}(p_2, p_1), \qquad \text{(A-3b)}$$

where the result of the function ATAN2 ranges between $\pm 180^0$.

Derivatives in the original (unrotated) coordinate system

Using indicial notation, the derivative in the x_l *(l=1,2,3)* direction of vector dip component p_n *(n=1,2)* in the unrotated coordinate system can be written as

$$p_n{}_{,l} = \partial_l p_n, \qquad \text{(A-4a)}$$

while the second derivatives in the *l* and *m* (*m*=1,2,3) directions are

$$p_n{}_{,lm} = \partial_m \partial_l p_n . \qquad \text{(A-4b)}$$

In terms of implementation, we compute the gradient of p_n numerically, using a convolutional operator described by Marfurt (2006). The second derivatives are computed by cascading two first derivative convolution derivative operators. The

convolution of the more finely sampled vertical dimension is accelerated by computing the convolution as a multiplication in the vertical wavenumber domain.

The vector dip and its derivatives in the rotated coordinate system

Di and Gao (2016) show that the equations for curvature and aberrancy are much simpler if the data are first flattened about the reflector normal at each voxel. Such flattening requires a rotation -φ about the original x_3-axis, followed by a rotation -θ first about the new x_2' axis. The resulting rotation operator **R** is then

$$\begin{bmatrix} p_1' \\ p_2' \\ p_3' \end{bmatrix} = \begin{pmatrix} R_{11} & R_{12} & R_{13} \\ R_{21} & R_{22} & R_{23} \\ R_{31} & R_{32} & R_{33} \end{pmatrix} \begin{pmatrix} p_1 \\ p_2 \\ p_3 \end{pmatrix} = \begin{pmatrix} \cos\theta\cos\varphi & -\cos\theta\sin\varphi & \sin\theta \\ \sin\varphi & \cos\varphi & 0 \\ -\sin\theta\cos\varphi & \sin\theta\sin\varphi & \cos\theta \end{pmatrix} \begin{pmatrix} p_1 \\ p_2 \\ p_3 \end{pmatrix} \tag{A-5}$$

where p_3=1. Writing equation A-5 in indicial notation using the Einstein summation convention (Einstein et al., 1938):

$$p_k' = R_{kn} p_n \ (k=1,2,3). \tag{A-6}$$

The gradient, ∂_l, is a vector operator and can also be rotated:

$$\partial_j' = R_{jl}\partial_l \ (j=1,2,3) \tag{A-7}$$

while the rotated second derivative operator becomes

$$\partial_i'\partial_j' = R_{im}\partial_m R_{jl}\partial_l = R_{im}R_{jl}\partial_m\partial_l \ (i=1,2,3). \tag{A-8}$$

Applying the operator in equation A-8 to the dip components in equation A-6, the rotated derivatives of p_k' are thus

$$\partial_i'\partial_j' p_k' = R_{im}\partial_m R_{jl}\partial_l R_{kn} p_n = R_{im}R_{jl}R_{kn}\left(\partial_m\partial_l p_n\right), \tag{A-9}$$

Where the terms in the parentheses are the previously calculated derivatives in the original, unrotated coordinate system given by equation A-4b. For efficiency, we compute the required derivatives in the unrotated system then using equation A-9.

APPENDIX B: COMPUTING THE EXTREMA OF APPARENT ABERRANCY

Derivation of the roots to the cubic equation

Di and Gao (2014) show that the apparent flexure, f_ψ, at azimuth ψ in the rotated coordinate system to be

$$f_\psi = \frac{\partial^3 z'}{\partial x_1' \partial x_1' \partial x_1'}\cos^3\psi + 3\frac{\partial^3 z'}{\partial x_1' \partial x_1' \partial x_2'}\cos^2\psi\sin\psi + 3\frac{\partial^3 z'}{\partial x_1' \partial x_2' \partial x_2'}\cos\psi\sin^2\psi + \frac{\partial^3 z'}{\partial x_2' \partial x_2' \partial x_2'}\sin^3\psi \quad \text{(B-1)}$$

Where $z'(x_1', x_2')$ is their rotated picked surface. Computing the derivative of f_ψ, with ψ and setting the result to zero results in an equation for three extrema:

$$\frac{df_\psi}{d\psi} = \cos^3\psi \cdot [-\frac{\partial^3 z'}{\partial x_1' \partial x_1' \partial x_2'}\tan^3\psi - (2\frac{\partial^3 z'}{\partial x_1' \partial x_1' \partial x_2'} - \frac{\partial^3 z'}{\partial x_2' \partial x_2' \partial x_2'})\tan^2\psi + (2\frac{\partial^3 z'}{\partial x_1' \partial x_2' \partial x_2'} - \frac{\partial^3 z'}{\partial x_1' \partial x_1' \partial x_1'})\tan\psi + \frac{\partial^3 z'}{\partial x_1' \partial x_1' \partial x_2'}]. \quad \text{(B-2)}$$

Next, Di and Gao (2014) set $y=\tan\psi$ and define coefficients *a*, *b*, *c*, and *d*, to obtain a simple cubic equation in *s*:

$$\frac{df_\psi}{d\psi} = \cos^3\psi(ay^3 + by^2 + cy + d) \quad . \quad \text{(B-3)}$$

The coefficients of equation B-3 are third derivatives of the rotated surface *z'*. In our volumetric implementation, we do not pick any surfaces. The third derivatives of *z'* in equation B-2 then become second derivatives of p_1' and p_2', resulting in

$$a = -\frac{1}{2}\left(\partial_2'\partial_2' p_1' + \partial_1'\partial_2' p_2'\right), \tag{B-4}$$

$$b = -\left(\partial_1'\partial_2' p_1' + \partial_1'\partial_1' p_2' - \partial_2'\partial_2' p_2'\right), \tag{B-5}$$

$$c = +\left(\partial_2'\partial_2' p_1' + \partial_1'\partial_2' p_2' - \partial_1'\partial_1' p_1'\right), \tag{B-6}$$

and

$$d = +\frac{1}{2}\left(\partial_1'\partial_2' p_1' + \partial_1'\partial_1' p_2'\right). \tag{B-7}$$

Setting equation B-3 to zero provides the three extrema of the cubic equation. There are multiple special cases that would lead to equation B-3 equals to zeros. The first is the degenerate case where:

$\cos^3\psi = 0$, and $\frac{df_\psi}{d\psi} \equiv 0$.

In this case, $\psi = 90^\circ$.

For the non-degenerate case where $\cos^3\psi \neq 0$, one solves the cubic equation

$$ay^3 + by^2 + cy + d = 0. \tag{B-8}$$

Computation of the roots to the cubic equation

Following Fan (1989), one defines the following variables in order to facilitate the computation of the roots of equation B-3:

$$\begin{aligned} A &= b^2 - 3ac, \\ B &= bc - 9ad, \\ C &= c^2 - 3bd, \text{ and} \\ \Delta &= B^2 - 4AC. \end{aligned} \tag{B-9}$$

There are several cases:

Case 1: $A = B = 0$ (three identical roots):

$$s_1 = s_2 = s_3 = -\frac{b}{3a} \quad . \tag{B-10}$$

Case 2: $A \neq 0, B \neq 0, \Delta > 0$ (only one real root) (Figure B-2):

$$s_1 = \frac{-b - \left(Y_1\right)^{1/3} + \left(Y_2\right)^{1/3}}{3a} \quad , \tag{B-11}$$

where

$$\begin{aligned} Y_1 &= Ab + 3a\left(\frac{-B + \sqrt{B^2 - 4AC}}{2}\right), \quad \text{and} \\ Y_2 &= Ab + 3a\left(\frac{-B - \sqrt{B^2 - 4AC}}{2}\right). \end{aligned} \tag{B-12}$$

Case 3: $A \neq 0, B \neq 0, \Delta = 0$ (three real roots, two of which are identical):

$$\begin{aligned} s_1 &= -\frac{b}{a} + \frac{B}{A}, \quad \text{and} \\ s_2 &= s_3 = -\frac{B}{2A}. \end{aligned} \tag{B-13}$$

Case 4: $A \neq 0, B \neq 0, \Delta < 0$ (three independent real roots) (Figure B-1):

$$\begin{aligned} s_1 &= \frac{-b - 2A^{1/2}\cos\Lambda}{3a}, \\ s_2 &= \frac{-b + A^{1/2}\left(\cos\Lambda + \sqrt{3}\sin\Lambda\right)}{3a}, \quad \text{and} \\ s_3 &= \frac{-b + A^{1/2}\left(\cos\Lambda - \sqrt{3}\sin\Lambda\right)}{3a}, \end{aligned} \tag{B-14}$$

where

$$\Lambda = \frac{1}{3}\arccos T, \quad \text{and}$$
$$T = \frac{2Ab - 3aB}{2A^{3/2}}. \tag{B-15}$$

The resulting values of ψ represent an azimuth in the rotated plane. To compute ψ projected on the *x*-*y* plane of the original unrotated coordinate system, one must first create a vector, **q'**,

$$\begin{pmatrix} q_1' \\ q_2' \\ q_3' \end{pmatrix} = \begin{pmatrix} \cos\psi \\ \sin\psi \\ 0 \end{pmatrix}, \tag{B-16}$$

and rotate it back using the transpose of **R**

$$\mathbf{q}=\mathbf{R}^{\mathrm{T}}\mathbf{q'}. \tag{B-17}$$

The desired aberrancy azimuth measured from North is then ATAN2(q_2,q_1).

APPENDIX C: MAGNITUDE OF ABERRANCY

The use of color by interpreters is subjective. Many of interpreters prefer the display of just the magnitude of aberrancy. We've emphasized the points that aberrancy is a vector, whereby the azimuth shows the orientation of the flexure. However, there are applications (e.g. co-rendering an edge attribute like aberrancy with impedance inversion or peak frequency) where one would rather use a grayscale. We have included an additional figure that shows coherence, dip magnitude, curvedness, and the magnitude of aberrancy, all plotted against a grayscale color bar in the Figure C-1.

APPENDIX D: APPARENT ABERRANCY

The maximum aberrancy is larger in magnitude than the intermediate and minimum aberrancy. The problem we have with aberrancy, is that the roots (at least at present) cannot be organized in a manner that separates geological features as k_1 and k_2 do for curvature. As crossing flexures become larger and smaller, we will encounter situations where the maximum aberrancy will follow two separate flexures rather than a single flexure that is losing strength when it crosses a second one gaining strength. Our current fix for this issue is to provide a suite of apparent aberrancy images, sorted by azimuthal windows (Figure D-1).

CHAPTER 3

CORRELATION OF SEISMIC ATTRIBUTES AND GEOMECHANICAL PROPERTIES TO THE RATE OF PENETRATION IN THE MISSISSIPPIAN LIMESTONE, OKLAHOMA [2]

ABSTRACT

The rate of penetration (ROP) measures drilling speed, which is indicative of the overall time and in general, the cost of the drilling operation process. ROP depends on many engineering 30 factors; however, if these parameters are held constant, ROP is a function of the geology. We examine ROP in the relatively heterogeneous Mississippian Limestone reservoir of north-central Oklahoma where hydrocarbon exploration and development have been present in this area for over fifty years. A 400 mi^2 (1036 km^2) 3D seismic survey and 51 horizontal wells were used to compute seismic attributes and geo-mechanical properties in the area of interest. Previous Tunnel Boring Machines (TBM) studies have shown that ROP can be correlated to rock brittleness and natural fractures. We therefore hypothesize that both structural attributes and rock properties should be correlated to ROP in drilling horizontal wells. We use a proximal support vector machine (PSVM) to link rate of penetration to seismic attributes and mechanical rock properties with the objective to better predict the time and cost of the drilling operation process. Our

[2] *This study is published as - Qi, X., J. Snyder, T. Zhao, K. J. Marfurt, and M. J. Pranter, 2017, Correlation of seismic attributes and geo-mechanical properties to the rate of penetration in the Mississippian Limestone, Oklahoma,* in *Mississippian Reservoirs of the Midcontinent: AAPG Memoir 116: AAPG Books Ahead of Print, doi:10.1306/13632162M1163795.*

workflow includes three steps: exploratory data analysis, model validation, and classification. Exploratory data analysis using 14 wells indicate high ROP is correlated with low porosity, high lambda-rho, high mu-rho, low curvedness, and high P-impedance. Low ROP was exhibited by wells with high porosity, low lambda-rho, low mu-rho, high curvedness and low P-impedance. Validation of the PSVM model using the remaining 37 wells gives an $R^2 = 0.94$. Using these five attributes and 14 training wells, we used PSVM to compute a ROP volume in the target formation. We anticipate that this process can help better predict a budget or even reduce the cost of drilling when an ROP assessment is made in conjunction with reservoir quality and characteristics.

INTRODUCTION

Drilling and completion of horizontal wells are the largest expenses in unconventional reservoir plays, where the cost of drilling a well is proportional to the time it takes to reach the target objective. Accordingly, the faster the desired penetration depth and offset is achieved, the lower the cost of the drilling process. The rate of penetration (ROP) is measured in all wells, but rarely examined by geoscientists. ROP depends on many factors, but the primary factors are weight on the drill bit, drill bit rotation speed, drilling fluid flow rate, and the characteristics of the formation being drilled (Bourgoyne et al., 1986). In this study, all wells were drilled within a 2-year period using similar drilling parameters, allowing investigation of the formation characteristics on the ROP.

Various approaches have been applied to estimate ROP. One of the main challenges for ROP estimation is the variability in the interplay between the rock and drilling speed (Farrokh et al., 2012). A "drill-off test" is a method primarily used to determine an optimum ROP for a set of conditions; however, a limitation of the drill-off test is that this process produces a static weight only valid for limited conditions during the test. The drill-off test does not work well under more complex geological conditions (King and Pinckard, 2000). Gong et al. (2007) utilized numerical simulations to investigate how rock properties affected penetration rates in Tunnel Boring Machines (TBM) and found that an increase in rock brittleness caused an increase in penetration rate. Later, a numerical model was created to model penetration rate for TBM's by Gong and Zhao (2009), who found that an increase in compression strength decreased ROP and an increase in volumetric joint count increased ROP.

In addition to well logs and cores, seismic attributes are widely used to predict lithological and petrophysical properties of reservoirs. For example, curvature anomalies commonly indicate an increase in rock strain, which in turn can be used to infer fractures (White et al., 2012). Impedance inversion is currently the most direct seismic-based estimate of rock properties. Seismic-impedance inversion results have been used to predict fault zones, potential fractures, and lithology in the Mississippian limestone (Dowdell et al., 2013; Roy et al., 2013; Verma et al., 2013; Lindzey et al., 2015). Young's modulus, E, and Poisson's ratio, υ, calculated from bulk density, ρ, compressional velocity, V_p, and shear velocity, V_s logs can be used to estimate rock brittleness (Harris et al., 2011).

Drilling and borehole measurements such as ROP are usually not linearly related to volumetric seismic attributes, such that the use of multilinear regression is limited. Artificial neural networks (ANN) are commonly used to link attributes to properties such as gamma-ray response (Verma et al., 2013), total organic carbon (TOC; Verma et al., 2016), and well production (Da Silva et al., 2012). The proximal support vector machine (PSVM) method is a more recent innovation that has been successfully used to predict brittleness (Zhang et al., 2015). PSVM utilizes pattern recognition and classifies points by mapping them to a higher dimension before assigning them to categories. PSVM has been applied in seismic facies recognition (e.g., channels, mass-transport complexes, etc.) (Zhao et al., 2015) and lithofacies classification (Zhao et al., 2014). Zhao et al. (2014) used PSVM to categorize shale and limestone on well logs with training inputs of gamma-ray and sonic logs.

With the recent onset of unconventional techniques such as horizontal drilling and hydraulic fracturing, the Mississippian limestone has seen a growth in activities. Where operators once targeted structural traps with vertical wells, now they target stratigraphic traps with horizontal wells (Lindzey et al., 2015). Such horizontal wells require a better understanding of the variability within the Mississippian limestone to increase the success and efficiency of precisely targeted directional wells. Throughout this study, a workflow is presented to establish a relationship between seismic attributes and rock mechanical properties with ROP to optimize well placement and decrease the drilling cost.

GEOLOGIC SETTING

The Mississippian limestone is a broad informal term that refers to dominantly carbonate deposits of the midcontinent (Parham and Northcutt, 1993). The main depositional environment represented in north-central Oklahoma is associated with the east–west trending ramp margin of the Burlington shelf of a starved basin environment (Costello et al., 2013). The thickness of the Mississippian limestone ranges from 350 ft (106.7 m) to 700 ft (213.4 m) north to south over the study area (Costello et al., 2013).

Mississippian limestone in the study area was deposited in a southward prograding system near the shelf margin during the Osagean and Meramecian (Costello et al., 2013). This environment has resulted in commonly acknowledged facies within the Mississippian carbonates, ranging from shale, chert conglomerate, tripolitic chert, dense chert, altered chert-rich limestone, dense limestone, to shale-rich limestone (Lindzey et al., 2015). In the study area, tripolitic chert is most prevalent in the Upper Mississippian zones and rapidly decreases in abundance at depth greater than 150 ft (45.7 m) below the pre-Pennsylvanian unconformity (Lindzey et al., 2015).

During the Early Mississippian, warm oxygenated water covered much of the ramp in the study area. Sponge-microbe bioherms formed elongate mounds below storm wavebase and produced abundant SiO_2 spicules, which led to formation of spicule-rich wackestones and packstones (Lindzey et al., 2015). Limestone and cherty limestone rich in marine fauna were the dominant sediments deposited at this time (Parham and Northcutt, 1993).

Regional uplift occurred during the Pennsylvanian, creating the Pennsylvanian unconformity that overlies most of the Mississippian in the midcontinent (Parham and Northcutt, 1993). The uplift not only removed large sections of rock but also reworked and caused alteration at the top of the Mississippian section and created detrital deposits of reworked Mississippian-aged rocks (Rogers, 2001). These altered sections of rocks comprise highly porous tripolitic chert and very dense glass-like chert. The leaching due to meteoric waters during relative sea-level fall has led to karstification and the formation of caverns and solution-channel features (Parham and Northcutt, 1993).

In the study area, diagenesis left intensely altered Mississippian limestone after deposition, and one of the most prominent of these diagenetic features is silica replacement (Lindzey et al., 2015). Water washed through the pores and redistributed the siliceous volcanic ash and some macrofossils, which left extensive microscale porosity (Lindzey et al., 2015). The dissolved silica precipitated in pore space and partially or completely replaced some carbonate fossils (Lindzey et al., 2015). Pore sediment structures are not well preserved due to the strong diagenetic overprint. Chert nodules are present, especially in highly reworked and bioturbated zones. Fractures are often filled with silica or calcite (Costello et al., 2013).

Molds, fractures, channels, and especially vugs are the most prominent pore type observed in the Mississippian interval of the study area (Lindzey et al., 2015). Vuggy porosity is often associated with tripolite but also exists in the other dominant facies. In many places where silica replacement took place, extensive secondary porosity formed in the shape of vugs (Rogers, 2001). Moldic porosity is also common, especially in

packstone and grainstone facies that exhibit more skeletal grains. Moldic porosity develops by dissolution of sponge spicules (Montgomery et al., 1998). Both fracture and channel porosity exist but are less abundant compared to the other pore types (Lindzey et al., 2015).

METHODOLOGY

In 2010, Chesapeake Energy acquired a 400 mi^2 (1,036 km^2) 3-D seismic survey in Woods County, Oklahoma (**Figure 3.1**). The seismic processing workflow included refraction statics, velocity analysis, residual statics, prestack time migration, frequency–space-time (FXY) predictive noise rejection, and Ormsby filtering. The overall data quality is excellent. The signal-to-noise ratio (S/N) is relatively high and the wavelet amplitude appears continuous throughout the Mississippian target. The data set includes digital well logs and mud logs for 83 wells consisting of 52 horizontal and 31 vertical wells. For the ROP analysis, only horizontal wells were used. These data consisted of 52 gamma-ray logs, 51 mud logs, and 18 of them are open-hole logs.

The wells in the area of interest were drilled by the same operator in a similar time period; therefore, we assume consistency between the wells regarding weight on bit, mud type, and bit type. This study evaluates the impact of geological properties on the ROP. The workflow contains three steps: training, validation, and classification (**Figure 3.2**). Prestack inversion and seismic-attribute volumes were generated for the Mississippian limestone and converted to depth. Geomechanical rock properties (from seismic inversion) and seismic-attribute values were interpolated and then extracted along each

wellbore every 2 ft (0.61 m) corresponding to the well-coordinate system from the mud logs. The mud logs give ROP in units of min/ft, which is an inverse velocity. We define the inverse velocity to be the cost of penetration (COP). The mean and standard deviation of COP for the 51 horizontal wells resulted in two categories: high and low COP with average values of 27 and 2.5 min/ft (89 and 8.2 min/m), respectively (**Figure 3.3**). Each coordinate location is assigned a COP category and a set of values including seismic attributes and geomechanical rock properties. The category and values for 30% of the wells were used as inputs to train the model. The remaining 70% of the wells were used to validate the model. When an optimal accuracy is reached, the model is used to classify the entire data set where wells have yet to be drilled and no COP data are available.

Time-Depth Conversion

Formation tops for the Lansing, Mississippian, and Woodford units were interpreted on the time-migrated seismic data in the time domain and on well logs in the depth domain. A conversion velocity model ($V_0(x, y)$) was built using commercial software PETREL (© Schlumberger), where velocity, V_0, is defined at the top of the Lansing datum, $Z_0(x, y)$. Depth, Z, is calculated by adding the depth below the Lansing, $\Delta Z = V_0(x, y) \times [t - t_0(x, y)]$ to the datum. The well tops were used as a correction factor in the creation of the velocity model. Well data were assigned more weights than the seismic data. We followed the recommended settings to build the velocity model, such that a moving-average method was used as an interpolation approach for creating the new

depth surfaces and an inverse-distance-squared algorithm was used to compute the inverse distance during the interpolation processes. Because the seismic horizons honored the faults in the study area, the velocity model is computed taking faults into consideration.

Geometric Attributes

Geometric attributes for this data set were generated using software AASPI developed at the University of Oklahoma. The attributes generated included: most positive curvature, k_1, most negative curvature, k_2, curvedness, $\sqrt{k_1^2 + k_2^2}$, shape index, $s = \frac{2}{\pi} ATAN(\frac{k_2 + k_1}{k_2 - k_1})$, coherent energy, and coherence. These attributes were chosen because of their ability to delineate the structural complexity in the area of interest. The sampling interval of these attributes is the same as the original seismic data volume, 110 × 110 ft (33.5 × 33.5 m). To match the mud log coordinate spacing, linear interpolation was used to generate values at 2 ft (0.61 m) intervals.

Geomechanical Rock Properties

Geomechanical rock properties were derived from prestack inversion results using commercial software Hampson Russell (©CGG GeoSoftware). Data preconditioning steps, prior to a prestack seismic inversion included phase shift, bandpass filtering (10–15–110–120 Hz), parabolic radon transform, and trim statics.

Exploratory Data Analysis

Exploratory data analysis consisted of evaluation of two different families of volumetric attributes as input to PSVM classification: geometric attributes and geomechanical rock properties with the goal of determining which attributes are most sensitive to COP in the heterogeneous Mississippian limestone.

Geometric attributes are used to aid in the interpretation of folds and faults. Based on the TBM observation by Gong et al. (2007), we hypothesize that COP is affected by faults and fractures. Therefore, we examined the correlation of the structural attributes coherence, dip magnitude, curvature, and curvedness to our two well clusters (**Figure 3.6**). The attribute histograms indicate little to no separation for coherence and dip magnitude; however, curvature and curvedness exhibit measurable separation. Figure 4D indicates that low curvedness correlates to low COP.

TBM analysis by Gong et al. (2007) also suggested that mechanical properties play a significant role in the variation of COP. Using prestack seismic inversion we computed porosity, lambda–rho, $\lambda\rho$, mu–rho, $\mu\rho$, and P-impedance volumes to analyze the Mississippian Limestone (**Figure 3.5**). The P-impedance measures the product of density and seismic P velocity. $\lambda\rho$ and $\mu\rho$ are used to estimate lithology and geomechanical behavior such as the brittleness index (Perez and Marfurt, 2013). **Figure 3.4B, C**, shows the high degree of separation for these rock properties. Low COP is related to low porosity, high $\lambda\rho$, high $\mu\rho$, and high P-impedance values. Conversely, high porosity, low $\lambda\rho$, low $\mu\rho$, and low P-impedance values are indicative of high COP. These differences were used to train the PSVM model and classify COP data based on the

geomechanical rock properties within the Mississippian interval in the study area (**Figure3.10**).

RESULTS

Interactive Classification

The rectangular frame separating the dark gray circle from the light gray circle in **Figure 3.7B** is called a discriminator. Note that many of the measurements cannot be separated in **Figure 3.7A**. Because Gong and Zhao (2009) found that increased brittleness improved TBM performance, we examine brittleness as a means to predict COP. Altamar and Marfurt (2014) used geomechanical properties to predict brittleness index for shale plays in the U.S.A. We display a crossplot in **Figure 3.9** where each sample was color-coded by COP and plotted in a 2-D space. Then we manually defined high COP (red), low COP (green), and mixed COP (yellow) polygons to define a 3-cluster template. A cross-plot of $\lambda\rho$ and $\mu\rho$ in **Figure 3.9A** illustrates the limitations of manually picking clusters in two-attribute space, where 50% of the voxels fall into the mixed COP (yellow) class. **Figure 3.9B**, a cross-plot of ρ and V_p/V_s, further shows this problem with the handpicked clusters where an even larger number of voxels falls into the mixed (yellow) class. **Figure 3.8** suggests improved class separation when using three attributes. However, drawing a template is significantly more challenging than in **Figure 3.6**.

PSVM Classification

Visualization and interactive visualization with more than three attributes is intractable. PSVM addresses this problem in two ways. First, it projects the data, in this case, two attributes defining a 2-D space that cannot be separated by a linear discriminator, into a higher 3-dimensional space (**Figure 3.7**) where separation by a planar discriminator is possible. Second, because the discriminator generation is machine driven rather than interpreter driven, one can introduce more than three input attributes. We used the five attributes, curvedness, $\lambda\rho$, $\mu\rho$, porosity, and P-impedance, which found to exhibit good histogram separation in all exploratory data analysis steps (**Figure 3.3**). The PSVM method allows us to create a classification model based on a set of training input. As the dimensionality of the input increases, the model becomes more accurate at classifying COP within the data set. For instance, during the validation process, we found the model to be sensitive to porosity. Before porosity was introduced to the model, the accuracy was 88.9%. When porosity was added as a new degree of dimensionality, the accuracy increased to 94%. This allowed for the creation of an optimal model with five degrees of dimensionality for COP classification across the study area.

A comparison of the histograms (**Figure 3.4**) shows that the generated PSVM model is more sensitive to geomechanical rock properties than geometric attributes. Indeed, strain (measured by curvature) is only one component necessary to generate natural fractures. Stearns (2015) found fractures measured in horizontal image logs were highly correlated to gamma-ray (lithology) response and only less connected to curvature, if at all. Nevertheless, this is not to say structural attributes such as curvature have no

effect on the model. We observed that higher COP values are linked with higher curvedness, which indicated that it is harder to drill through the formation with higher structural complexities. Studies have found that large curvature values are related with natural fractures, which may or not be cemented (Bourgoyne et al., 1986; Hunt et al., 2011). Such heterogeneities may slow the drilling progress. Porosity is another good indicator of microstructures associated with fracture geometry. Low porosity observed in low-COP wells may seem counter-intuitive at first; however, woodworkers observe that there are few bit problems when drilling through oak, but that the bit often gets stuck or even breaks when drilling relatively "soft" pine (Neher, 1993). Again, using the woodworker's analogy, one uses different saw blades for different woods. The bits used in this survey may have been chosen to deal effectively with the very hard chert.

CONCLUSIONS

COP is a major factor affecting the time spent drilling a well and is directly related to the overall cost of the drilling process. This is the first study that links COP to seismic data and seismic-related attributes. Clustering five attributes using a PSVM classification method, we were able to correlate COP with seismic attributes and geomechanical rock properties and obtain a confidence of 94%. Low COP was observed in wells encountering low porosity, high $\lambda\rho$, high $\mu\rho$, low curvedness, and high P-impedance. High COP was observed in wells encountering high porosity, low $\lambda\rho$, low $\mu\rho$, high curvedness, and low P-impedance. By using this workflow, we can use COP of previously drilled wells with 3-D seismic data to predict COP over the study area. Whereas one may still wish to drill

a specific target objective, we claim that this statistical analysis technique will provide a more accurate cost estimate and help choose the appropriate drilling equipment.

CHAPTER 3 FIGURES

(a)

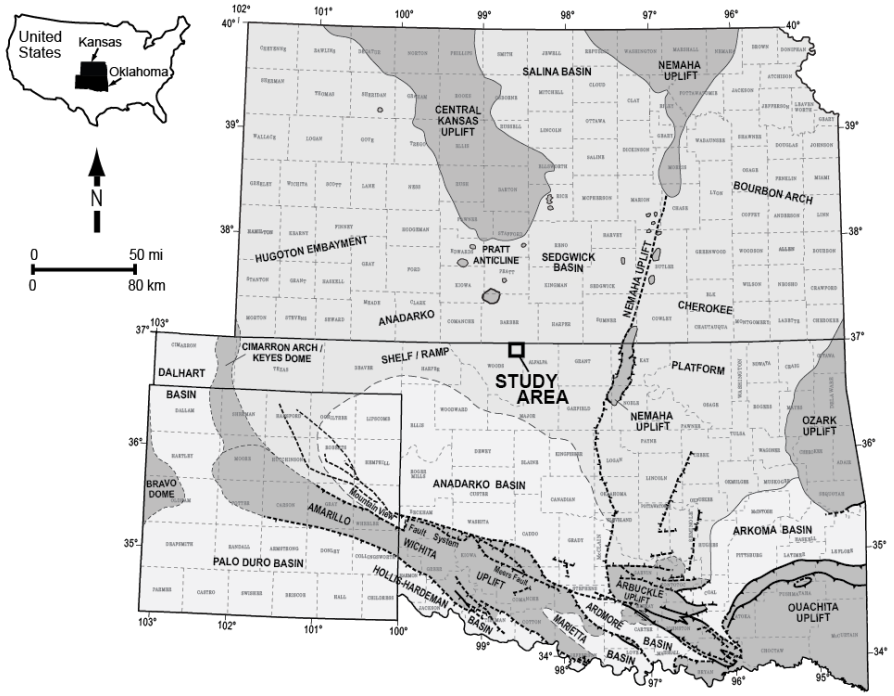

(b)

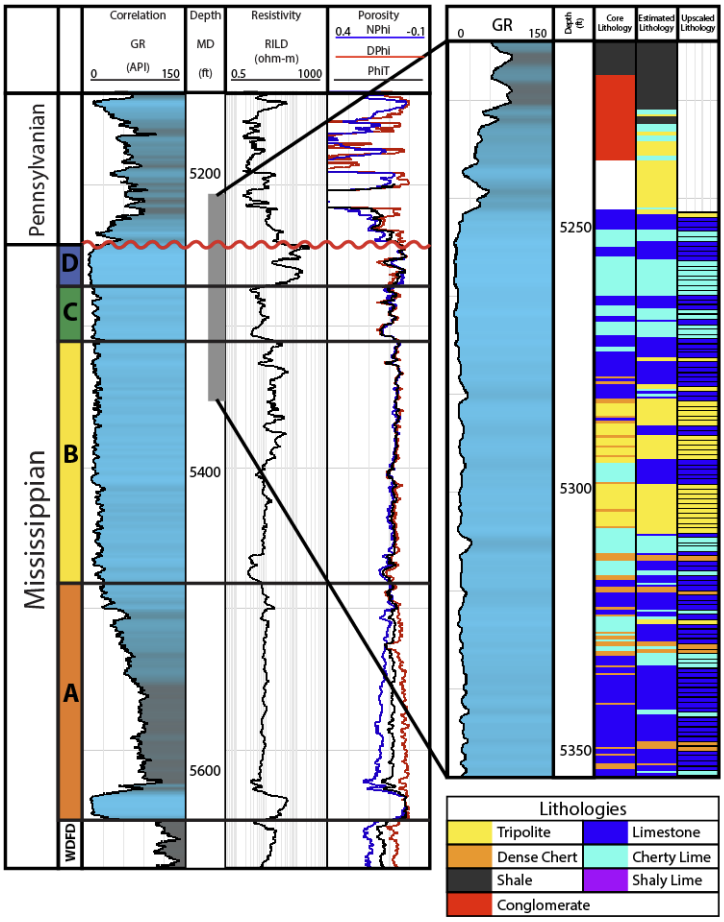

Figure 3.1. (A) Major geologic provinces of Oklahoma with the area of interest outlined in red. (Modified from Johnson and Luza, 2008; Northcutt and Campbell, 1996). (B) a type log showing the Mississippian Limestone section in the area of interest (Modified from Lindzey et al., 2015).

(a)

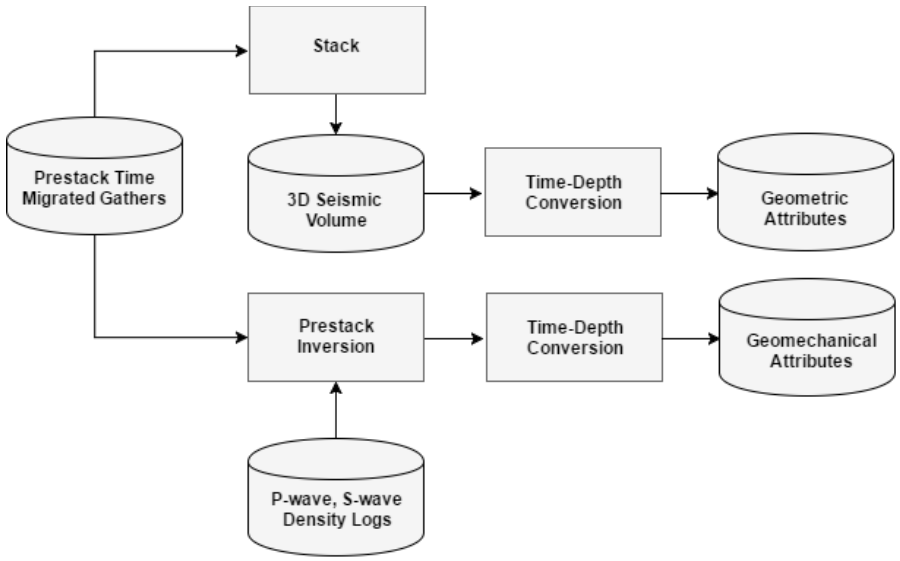
Stack
Prestack Time Migrated Gathers
3D Seismic Volume
Time-Depth Conversion
Geometric Attributes
Prestack Inversion
Time-Depth Conversion
Geomechanical Attributes
P-wave, S-wave Density Logs

(b)

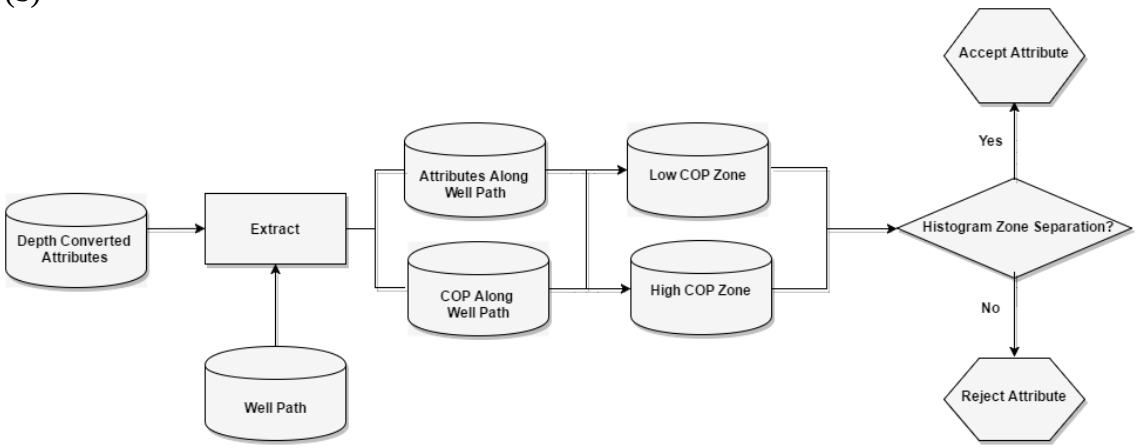
Accept Attribute
Yes
Depth Converted Attributes
Extract
Attributes Along Well Path
Low COP Zone
Histogram Zone Separation?
COP Along Well Path
High COP Zone
No
Well Path
Reject Attribute

(c)

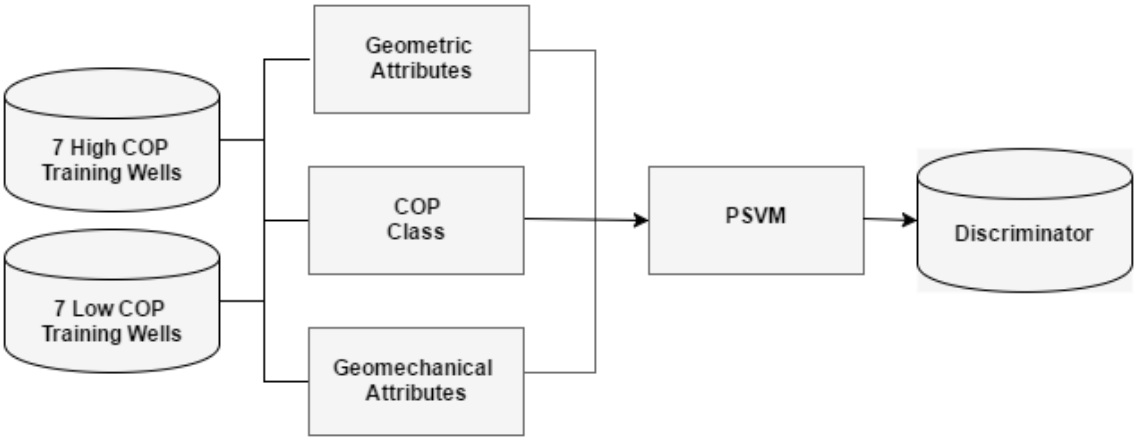

(d)

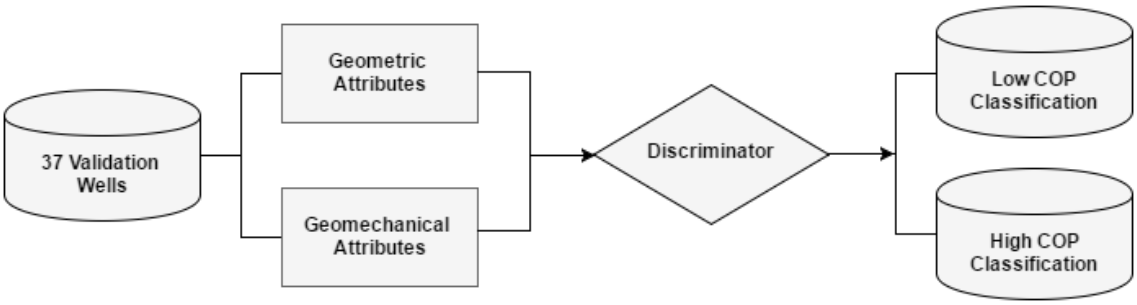

Figure 3.2. (a) Workflow for attribute generation and depth conversion, (b) data analysis of the extracted parameters, (c) the training process, and (d) the validation process.

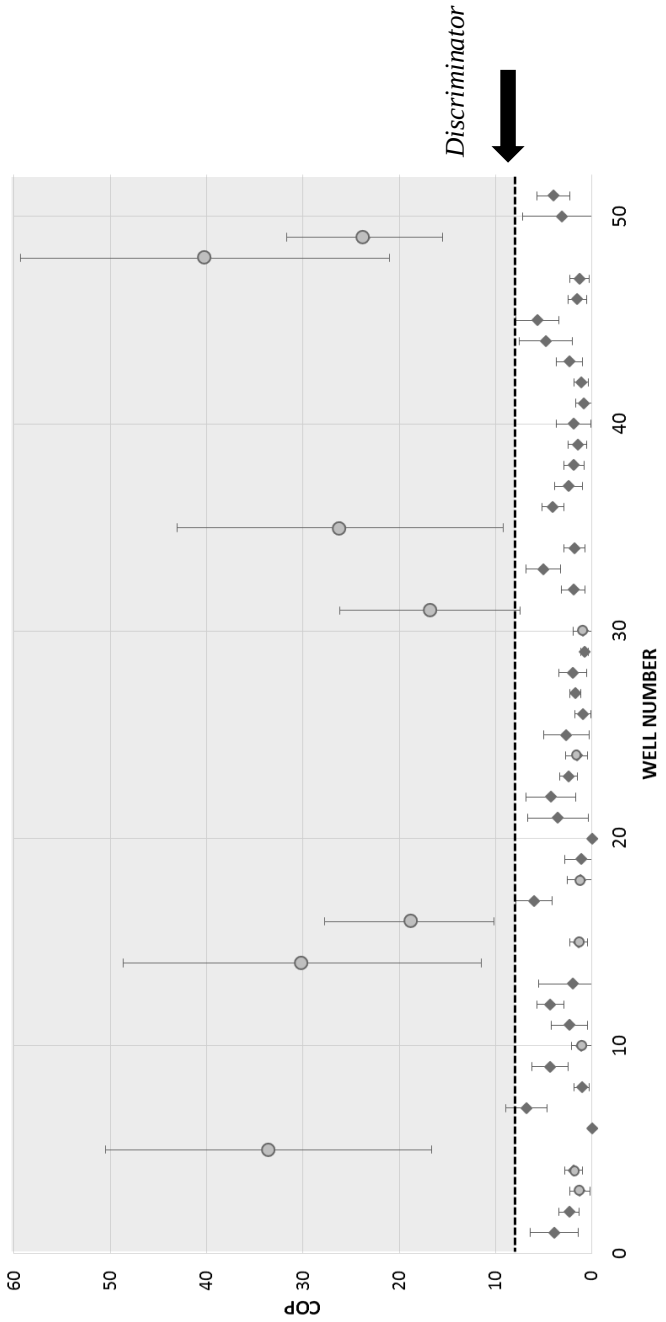

Figure 3.3. The mean and standard deviation of COP for 51 horizontal wells that fall within the 3D seismic survey. We separate these wells into two classes: seven high COP (the grey cluster) and forty-four low COP wells (the white cluster). The dashed line is called the discriminator between the two clusters.

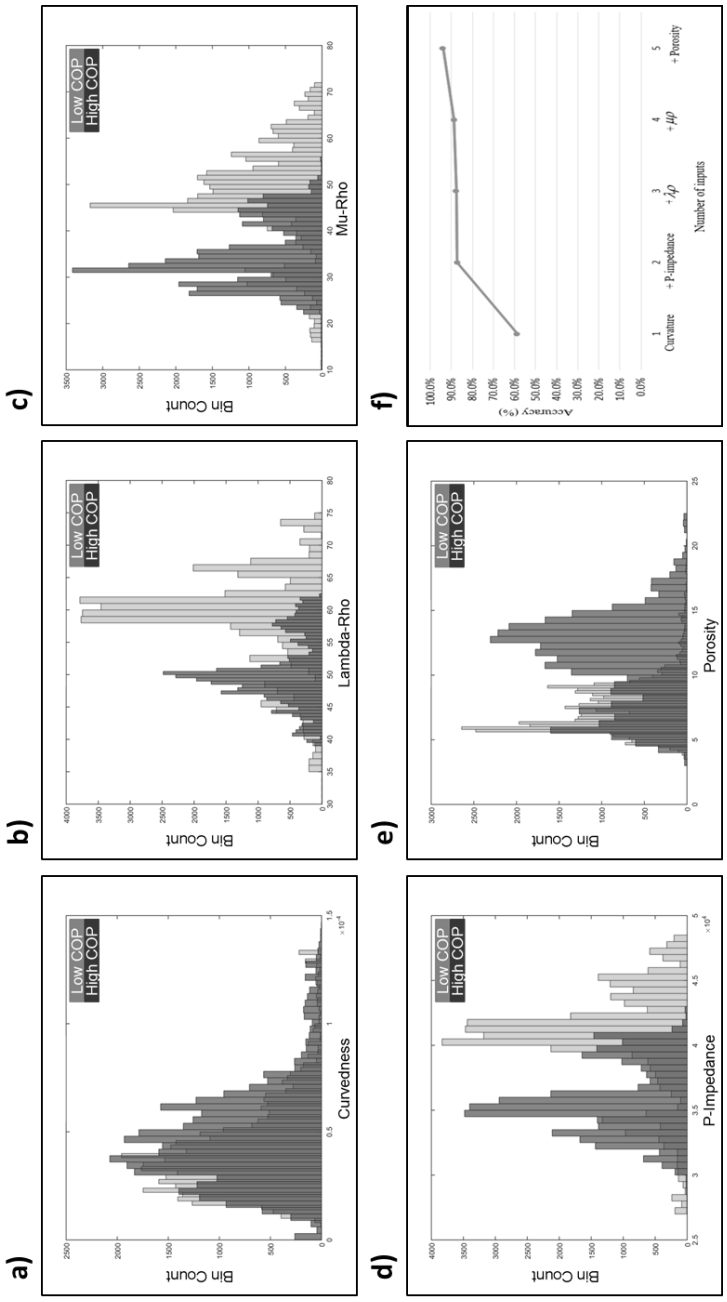

Figure 3.4. Exploratory data analysis using the workflow shown in Figure 3.2b. Showing five attributes exhibiting good histogram separation between high COP (in dark gray) and low COP (in light gray) along all well trajectories: (a) curvedness, (b) $\lambda\rho$, (c) $\mu\rho$, (d) P-impedance, and (e) porosity. (f) Results of the validation test using seven low and seven high COP wells which are highlighted by gray circle in Figure 3.3. With increases in the number of inputs (from one to five), the accuracy increases accordingly.

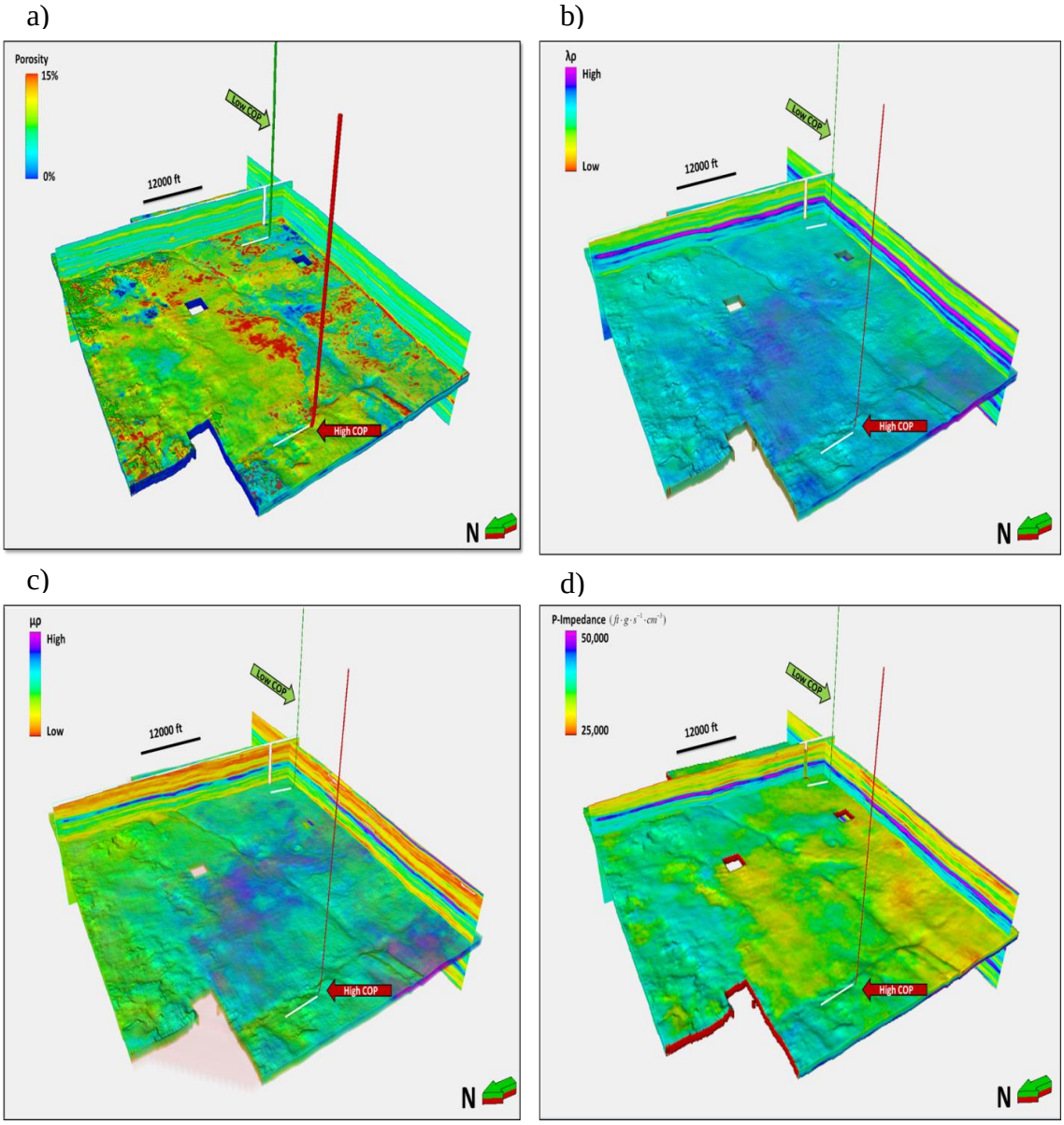

Figure 3.5. Horizon probes along the top of Mississippian Limestone through (a) porosity, (b) $\lambda\rho$, (c) $\mu\rho$, and (d) P-impedance volumes. Red and green well paths denote representative high and low COP wells, respectively.

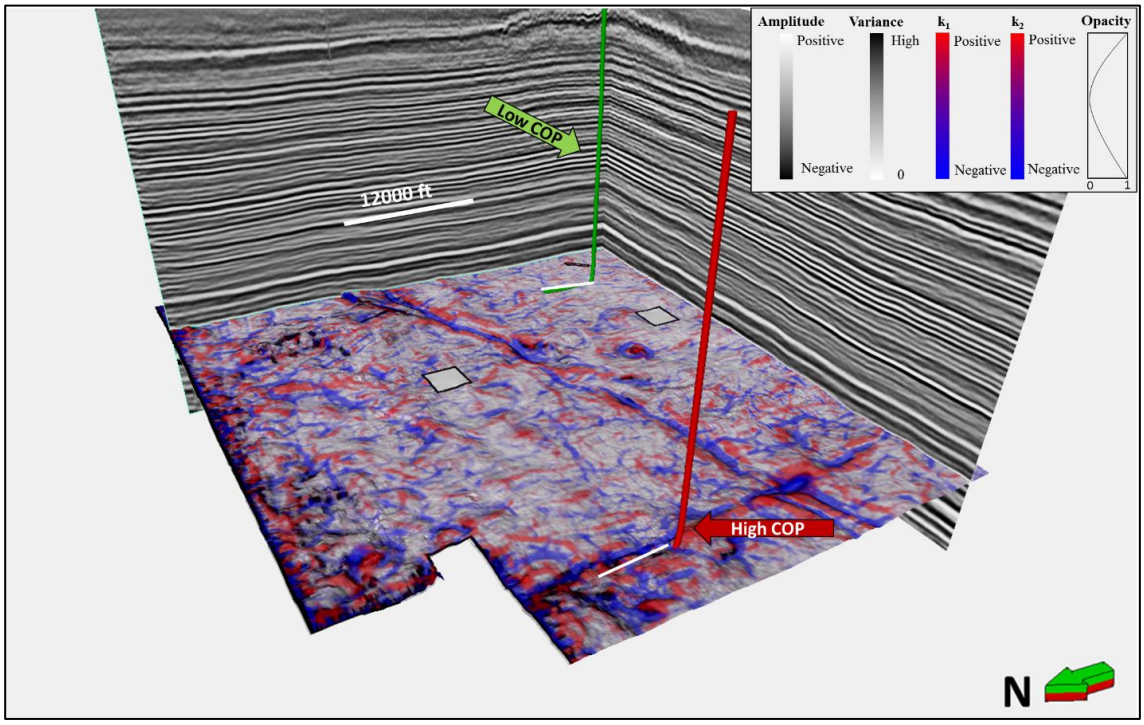

Figure 3.6. Co-rendered the most positive (k_1) and the most negative (k_2) curvature along the top of the picked Mississippian horizon with two representative high and low COP wells paths. The opacity curve is applied to k_1 and k_2.

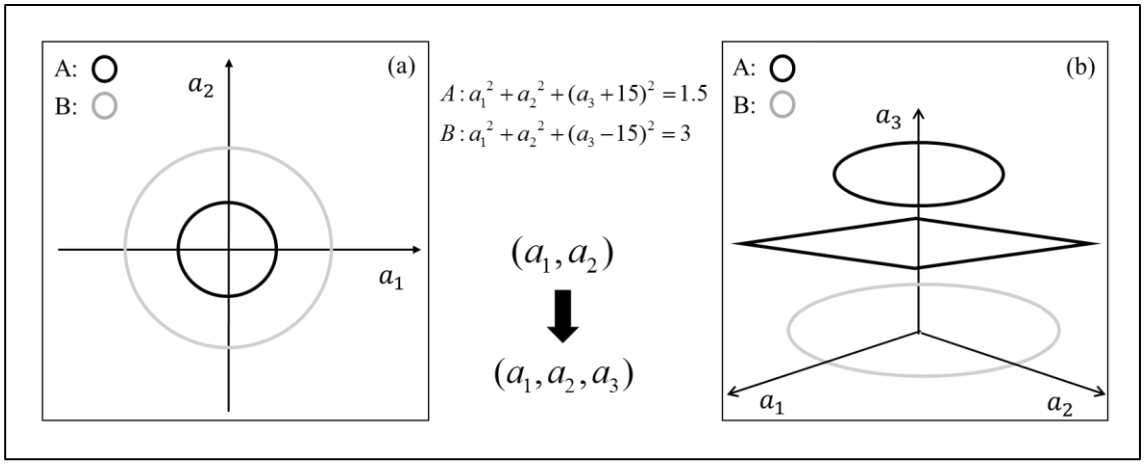

Figure 3.7. (a) when two different clusters are impossible to separate by a line in a 2-D space. (b) increasing the dimensionality to 3 through a nonlinear attribute transformation allows separation of the two classes by a plan.

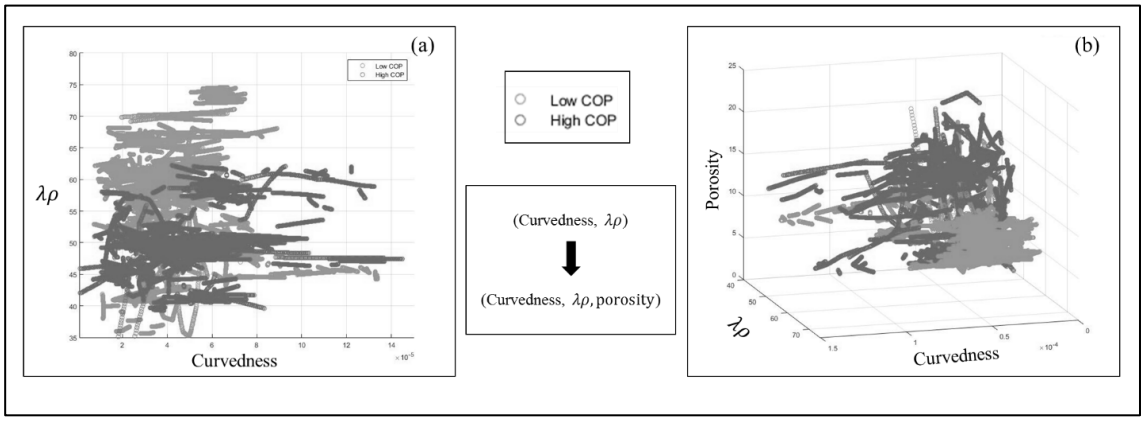

Figure 3.8. (a) Similarly, high and low COP is difficult to discriminate when using $\lambda\rho$ and curvedness in a 2-D space. (b) Discrimination becomes easier by adding a third porosity axis.

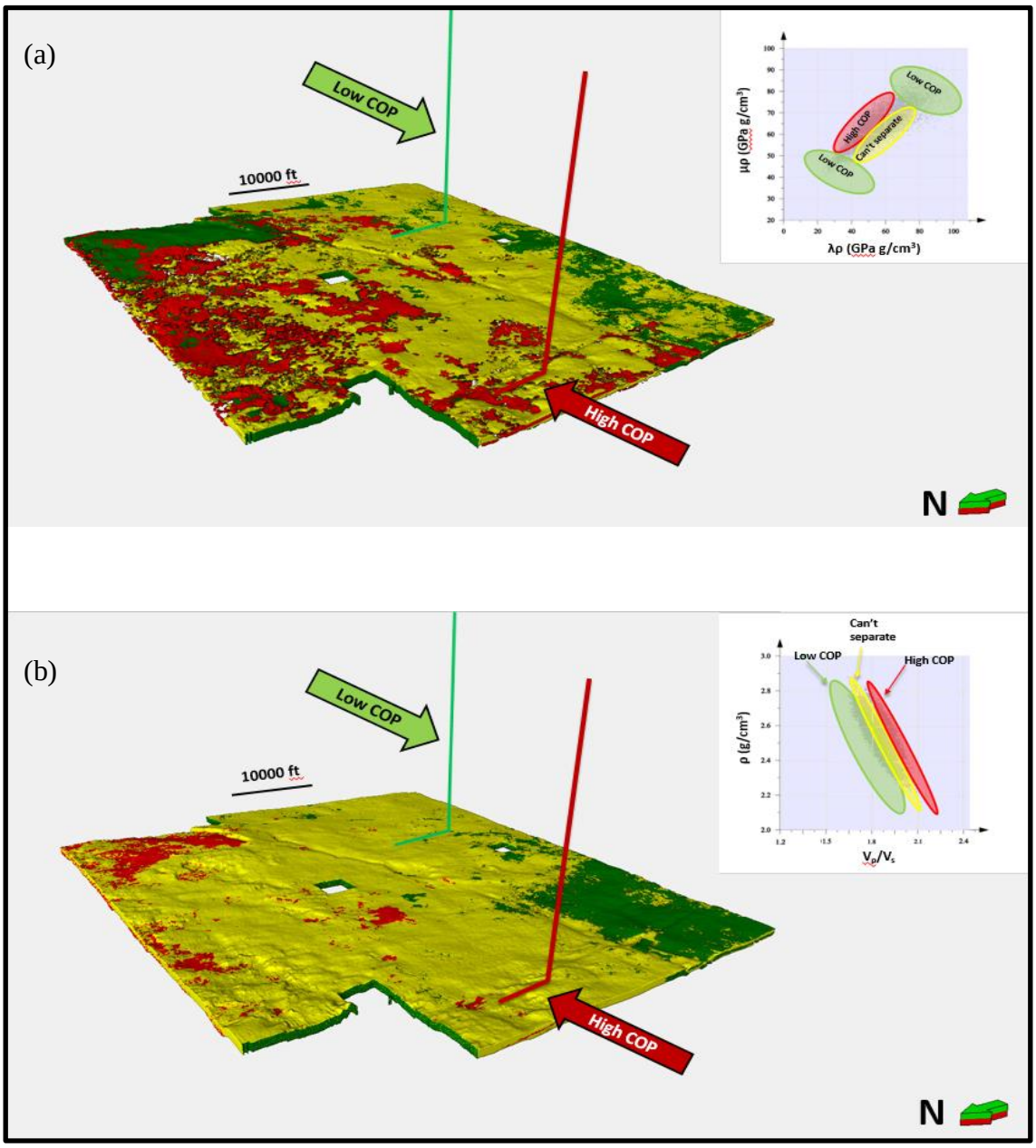

Figure 3.9. (a) An interactive classification in λρ-μρ space. Along the wellbore we have λρ, μρ and COP triplets. Each sample is color-coded along the well by its COP and plot in λρ-μρ space. Red, green and mixed cluster polygons are hand-drawn polygons around each cluster. This template is then used to color-code voxels between the top of the Mississippian Limestone and the top of Woodford. Red and green well paths denote representative high and low COP wells. In (b) Classification in ρ-V_p/V_s space. Triplets of ρ, V_p/V_s and COP are sampled along the wellbore, crossplotted, and a new template constructed and used to color code the Mississippian interval. Note that neither template accurately predicts the COP of these two wells.

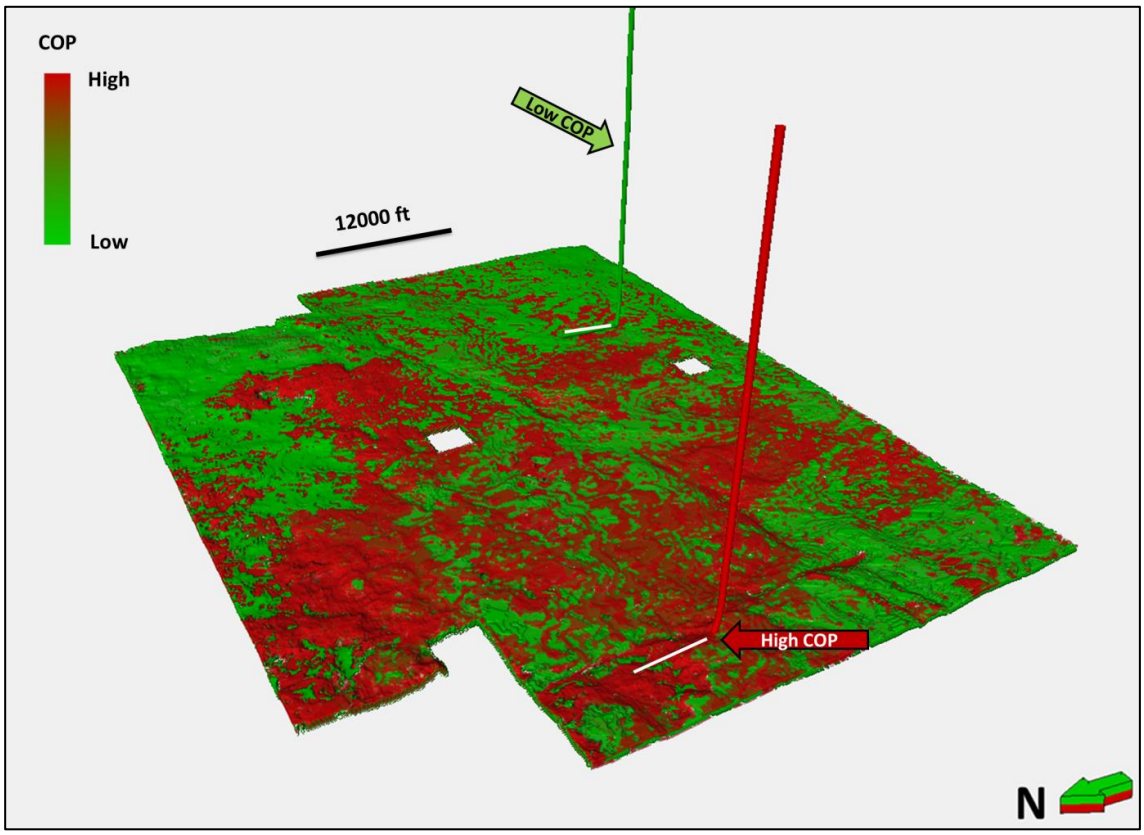

Figure 3.10. Horizon probe of COP on the Mississippian Limestone computed using the five attributes shows in Figure 3.4-3.6 and a PSVM classifier. Note that the two representative wells now fall along voxels corresponding to their observed COP value.

REFERENCES

Altamar, R. P., and K. Marfurt, 2014, Mineralogy-based brittleness prediction from surface seismic data: Application to the Barnett Shale: Interpretation, v. 2, no. 4, p. T255–T271, doi:10.1190/INT-2013-0161.1.

Bass, N. W., 1942, Subsurface geology and oil and gas resources of Osage County, Oklahoma: U.S. Geological Survey Bulletin 900-K, p. 343–393.

Bourgoyne, A. T., K. K. Millheim, M. E. Chenevert, and F. S. Young Jr., 1986, Applied drilling engineering chapter 8 solutions: Richardson, Texas, Society of Petroleum Engineers, 99 p.

Costello, D., M. Dubois, and R. Dayton, 2013, Core to characterization and modeling of the Mississippian, North Alva area, Woods and Alfalfa Counties, Oklahoma: AAPG Mid-Continent Section Core Workshop: From source to reservoir to seal, Wichita, Kansas, p. 165–175.

Da Silva, M., and K. Marfurt, 2012, Framework for EUR correlation to Seismic Attributes in the Barnett Shale, TX, *in* D. Steeples, ed., SEG Technical Programs Expanded Abstracts 2012, p. 1–5.

Dowdell, B. L., J. T. Kwiatkowski, and K. J. Marfurt, 2013, Seismic characterization of a Mississippi Lime resource play in Osage County, Oklahoma, USA: Interpretation, v. 1, no. 2, p. SB97–SB108, doi:10.1190/INT-2013-0026.1.

Farrokh, E., J. Rostami, and C. Laughton, 2012, Study of various models for estimation of penetration rate of hard rock TBMs: Tunnelling and Underground Space Technology, v. 30, p. 110–123, doi:http://dx.doi.org/10.1016/j.tust.2012.02.012.

Gong, Q. M., and J. Zhao, 2009, Development of a rock mass characteristics model for TBM penetration rate prediction: International Journal of Rock Mechanics and Mining Sciences, v. 46, no. 1, p. 8–18, doi:http://dx.doi.org/10.1016/j.ijrmms.2008.03.003.

Gong, Q. M., J. Zhao, and Y. S. Jiang, 2007, In situ TBM penetration tests and rock mass boreability analysis in hard rock tunnels: Tunnelling and Underground Space Technology, v. 22, no. 3, p. 303–316, doi:http://dx.doi.org/10.1016/j.tust.2006.07.003.

Harris, N. B., J. L. Miskimins, and C. A. Mnich, 2011, Mechanical anisotropy in the Woodford Shale, Permian Basin: Origin, magnitude, and scale: The Leading Edge, v. 30, no. 3, p. 284–291, doi:10.1190/1.3567259.

Hunt, L., S. Reynolds, S. Hadley, J. Downton, and S. Chopra, 2011, Causal fracture prediction: Curvature, stress, and geomechanics: The Leading Edge, v. 30, no. 11, p. 1274–1286, doi:10.1190/1.3663400.

King, C. H., and M. D. Pinckard, 2000, Method of and system for optimizing rate of penetration in drilling operations: Google Patent US6026912A, filed April 2, 1998, and issued February 22, 2000.

Lindzey, K., M. J. Pranter, and K. Marfurt, 2015, Geologically constrained seismic characterization and 3-D reservoir modeling of Mississippian reservoirs, North Central Anadarko Shelf, Oklahoma: AAPG Annual Convention and Exhibition, Denver, Colorado, May 31–June 3, 2015.

Mazzullo, S. J., B. W. Wilhite, and I. W. Woolsey, 2009, Petroleum reservoirs within a spiculite-dominated depositional sequence: Cowley Formation (Mississippian: Lower Carboniferous), south-central Kansas: AAPG bulletin, v. 93, no. 12, p. 1649–1689.

Montgomery, S. L., J. C. Mullarkey, M. W. Longman, W. M. Colleary, and J. P. Rogers, 1998, Mississippian "Chat" reservoirs, South Kansas: Low-resistivity pay in a complex chert reservoir: AAPG Bulletin, v. 82, p. 187–205.

Neher, H. V., 1993, Effects of pressures inside Monterey pine trees: Trees, v. 8, no. 1, p. 9–17, doi:10.1007/BF00240976.

Parham, K. D., and R. A. Northcutt, 1993, Mississippian chert and carbonate basal Pennsylvanian sandstone: Central Kansas Uplift and northern Oklahoma, *in* D. G. Bebout, W. A. White, T. F. Hentz, and M. K. Grasmick, eds., Atlas of major midcontinent gas reservoirs: Austin, Texas, Texas Bureau of Economic Geology, p. 57-60.

Perez, R., and K. Marfurt, 2013, Brittleness estimation from seismic measurements in unconventional reservoirs: Application to the Barnett Shale, *in* James Schuelke, ed., SEG Technical Program Expanded Abrstacts 2013, p. 2257–2293.

Rogers, S. M., 2001, Deposition and diagenesis of Mississippian chat reservoirs, North-Central Oklahoma: AAPG Bulletin, v. 85, no. 1, p. 115–129, doi:10.1306/8626C771-173B-11D7-8645000102C1865D.

Roy, A., B. L. Dowdell, and K. J. Marfurt, 2013, Characterizing a Mississippian tripolitic chert reservoir using 3D unsupervised and supervised multiattribute seismic facies analysis: An example from Osage County, Oklahoma: Interpretation, v. 1, no. 2, p. SB109–SB124, doi:10.1190/INT-2013-0023.1.

Stearns, V. T., 2015, Fracture characterization of the Mississippi lime utilizing whole core, horizontal borehole images, and 3D seismic data from a mature field in Noble County Oklahoma: M.S. thesis, University of Oklahoma, Norman, Oklahoma, 75 p.

Verma, S., O. Mutlu, and K. J. Marfurt, 2013, Seismic modeling evaluation of fault illumination in the Woodford Shale, *in* James Schuelke, ed., SEG Technical Program Expanded Abrstacts 2013, p. 3310–3314.

Verma, S., T. Zhao, K. J. Marfurt, and D. Devegowda, 2016, Estimation of total organic carbon and brittleness volume: Interpretation, v. 4, no. 3, p. T373–T385, doi:10.1190/INT-2015-0166.1.

Watney, W. L., W. J. Guy, and A. P. Byrnes, 2001, Characterization of the Mississippian chat in south-central Kansas: AAPG Bulletin, v. 85, no. 1, p. 85–113.

White, H., B. Dowdell, and K. J. Marfurt, 2012, Calibration of surface seismic attributes to natural fractures using horizontal image logs, Mississippian Lime, Osage County, Oklahoma, *in* D. Steeples, ed., SEG Technical Program Expanded Abstracts 2012, p. 1–6.

Zhang, B., T. Zhao, X. Jin, and K. Marfurt, 2015, Brittleness evaluation of resource plays by integrating petrophysical and seismic data analysis: Interpretation, v. 3, no. 2, p. T81–T92, doi:10.1190/INT-2014-0144.1.

Zhao, T., V. Jayaram, K. J. Marfurt, and H. Zhou, 2014, Lithofacies classification in Barnett Shale using proximal support vector machines, *in* B. Birkelo, ed., SEG Technical Program Expanded Abstracts 2014, p. 1491–1495.

Zhao, T., V. Jayaram, A. Roy, and K. J. Marfurt, 2015, A comparison of classification techniques for seismic facies recognition: Interpretation, v. 3, no. 4, p. SAE29–SAE58, doi:10.1190/INT-2015-0044.1.

CHAPTER 4

CALIBRATING VOLUMETRIC ABERRANCY FRACTURE PREDICTION USING BOREHOLE IMAGE LOGS AND MUD LOGS: APPLICATION TO THE MISSISSIPPIAN LIMESTONE [3]

ABSTRACT

Seismic attributes have been widely used to capture the morpholocial features seen in seismic data. Nevertherless, it is still a challenge to map subtle fautls and other discontinuies using relatively low resolution 3D seismic data. Volumetric aberrancy measures the gradient or lateral change of curvature, which anomalies would track the sub-seismic faults and flexures makes it complementary to coherence and curvature. At present, no direct relationships have been established between aberrancy vectors and fractures associated with faults. This study explores whether volumetric aberrancy can be statistically validated to be a fracture predicition proxy in undrilled parts of the survey. A suite of geometric including aberrancy vectors and geomechanical attributes were generated for the Mississippian Limestone target containing five interpreted borehole image logs and 52 mud log. With the use of Convolutionary Neural Network, eight statistically significant seismic attributes were chose to model fractures seen on the image logs over the Mississipppian Limestone horizon with the total accuracy 65%.

---

[3] *This study is prepared to publish as – Qi, X., M. Pranter, and K. Marfurt, Calibrating volumetric aberrancy fracture prediction using borehole image logs and mud logs: application to the Mississippian Limestone.*

INTRODUCTION

Seismic Attributes

Since the mid-1990s, seismic attributes have been widely used to capture the morphological features seen in seismic data. For example, the coherence attribute developed in the middle 1990s captures the same fault discontinuities that Rummerfield (1954) saw in the seismic amplitude data (Chopra and Marfurt, 2005). Nevertheless, it is still a challenge to map subtle faults and other discontinuities using relatively low resolution 3D seismic data that are more easily imaged using higher resolution cores, electric logs, and horehole image logs.

Volumetric aberrancy measures the lateral change (or gradient) of the curvature of a picked or inferred surface (Schot, 1978) and is complementary to curvature and coherence. While coherence measures disruptions in these surfaces, dip, curvature, and aberrancy measure changes in their orientation and morphology. Following horizon-based aberrancy calculation introduced by Di and Gao (2014), Qi and Marfurt (2018) extended aberrancy to provide volumetric results of uninterpreted seismic data volumes. In extensional terrains exhibiting normal faults, an aberrancy anomaly will track a coherence anomaly and fall between a most-positive curvature anomaly defining the footwall and a most-negative curvature anomaly defining the hanging wall. Aberrancy often delineates faults which may not exhibit a coherence anomaly when the throw falls below seismic resolution, is distributed across a suite of smaller conjugate faults, or is smeared due to inaccurate velocities and/or statics applied in the processing (Qi and Marfurt, 2018). At present, no direct relationships have been established between

aberrancy vectors and fractures associated with faults. This study explores whether volumetric aberrancy can be statistically validated to be a fracture predicition proxy in undrilled parts of the survey.

Fractures and Image Logs

Since their development in the late 1960s (Zemanek et al., 1969), borehole image logs have been widely used to map fractures in the subsurface (Wu and Pollard, 2002). More recently, several studies have explored the correlation between seismic attributes and fracturing using borehole image logs. In his analysis of core and borehole images in a North-Central Oklahoma Mississippian Limestone survey, Stearns (2015) found that curvature is an excellent measure of structural deformation and hence strain. However, fractures measured in a suite of horizontal image logs were more strongly correlated to lithology than to strain. Cook (2016) conducted a multi-linear regression analysis of six geometric attributes with fractures measured in horizontal image logs in a Northwest Oklahoma Mississippi Limestone survey and found that coherence images of karst features seeb on surface seismic data correlated strongly with natural fractures seen on image logs. Staples (2011) built a suite of clay models, induced extensional and compressional faults, measuring the degree of deformation using laser scans and the fracture density usng photographic images, and found an excellent (though nonlinear) correlation between curvature and fracture density. He then confirmed this correlation between curvature measured on a 3D seismic survey and seven horizontal image logs acquired in the Hunton Limestone of the Cherokee Platform, OK. White (2012) extended Staple's (2011) clay model experiments to include simple folding, confirming the

correlation of curvature to fractures. He further validated this correlation between fractures and folding on outcrops seen in Cambrian limestones in the Arbuckle Mountains of south-central Oklahoma, as well as between fractures measured in image logs and curvature seen on seismic data in the Mississippi Limestone in an Osage county, OK survey. Given these observations, and the fact that aberrancy is a lateral derivative of curvature, we hypothesize that aberrancy will be computed from 3D seismic data will be correlated to faults and fractures seen on image logs acquired in horizontal wells.

Cost of penetration (COP) measures how fast the drill bit go through formation. Increases in rock brittleness may cause an increase in penetration rate (Gong et al., 2007). Qi et al. (2017) explored the correlation between COP with structural attributes, and found high curvature values to be linked with lower COP values. Since aberrancy measures the gradient of curvature, we hypothesize that aberrancy can show statistically significant correlation with COP.

Linear vs. Nonlinear Correlation

White (2012) showed that drilling and borehole measurements such as fracture intensity are not linearly related to volumetric seismic attributes. Specifically, the initiation of fractures is preceded by an elastic stage of deformation, whereby the rock may be strained, but not fractured. After some minimum level of strain, the first fracture occurs, with more fractures monotonically increasing until the distance between fractures approximates the layer thickness. After reaching this "fracture saturation" point, increasing strain isg accomodated by movement along existing fractures, which are now named faults. Microseismic experiments also indicate nonlinear behavoir, with Perez and

Marfurt (2015) finding brittle rocks to accommodate most fracture events, while ductile rocks accommodate few, if any fracture events, suggesting some brittleness failure threshold. These two nonlinear observations indicate that the use of multilinear regression is limited.

In contrast to multilinear regression, neural networks are able to identify nonlinear relationships and have been successfully used in correlating well measurements to seismic attributes for almost two decades. To estimate porosity in wells, Leiphart and Hart, (2001) frist conducted a multi-linear regression analysis. Though the correlation between seismic attribues and observed porosity logs was good, exhibiting an R^2=0.74 in Lower Brush Canyon channeled sandstones, the estimated porosity volume did not correlate to known geologic features. They then trained a probabilistic neural network to look for a nonlinear relationship with the input of seven seismic attributes, including amplitude, frequency, P-wave impedance, and others. The neural network results not only exhibited a geologically realistic porosity distribution but also provided a better correlation (R^2=0.82).

We begin this paper with an overview of the Mississippian Limestone in north-central Oklahoma, previously analyzed by Cook, (2016). Next, we review the principals of volumetric aberrancy. We then use Cook's (2016) image log and Qi et al.'s (2018) mud log analyses as calibration data to determine if we can establish a quantitative relation between fractures, COP, and seismic aberrancy. Building on observations by Stearns (2016), we combine our aberrancy volumes with other geometric and geomechanical seismic attributes as input to a neural-network computer analysis. We

conclude with a summary of our findings on the use of volumetric aberrancy as an aid to structural interpretation and quantitative fracture prediction.

GEOLOGIC SETTING

The Anadarko Basin is one of the richest oil and gas reservoirs in the United States. The structural elements of the basin were created through faulting and uplift of the Wichita Orogeny during the Pennsylvanian Period. The basin is bounded to the east by the Nemaha Uplift and to the south by the Wichita Mountains and Amarillo Uplift. The basin shallows as it moves north onto a shelf (Ball et al., 1991). This shelf, better known as the Anadarko Shelf, was formed during the Permian period. The area of interest is in Woods County, located in the northwest part of Oklahoma within the Anadarko Shelf and is bounded by the Cimarron River to the west and south. Woods County has been an active petroleum production area since 1953, when the county first began producing oil (Bowles, 1961).

Our study is primarily focused on the Mississippian section which was deposited during the Late Devonian through early Pennsylvanian. During Mississippian time, the mid-continent region that is now northern Oklahoma was at 20° south latitude, covered by a well-oxygenated, shallow sea. The shelf margin sloped gradually from relatively shallow water (Mazzullo et al., 2011) to a deeper seaway to the south that paralleled the converging plate boundaries (Scotese, 1999). This plate boundary may have relesed volcanic emissions that provided the source of slica (Watney et al., 2001). Parallel to the shelf margin, sponge-microbe bioherms formed elongated mounds which led to the

deposit of spicule-rich wackestones and packstones (Watney et al., 2001). The shelf region was a highly productive carbonate factory located around the mounds.

The Mississippian Limestone in the study area was deposited in a southward prograding system near the shelf margin during approximately 360 to 320 million years ago (Costello et al., 2013). Subsurface units of the Mississippian system in Woods County include rocks of the Chesteran, Meramecian, Osagian, and Kinderhookian Series **(Figure 3.1)**. Lindzey (2015) created a type log in the study area using a well with both core sample and log data. The type log shows that the Chesterian interval is absent in the study area, subcropping south of the seismic survey.

The thickness of the Mississippian Limestone ranges from 350 ft (106.7 m) to 700 ft (213.4 m) north to south over the study area (Costello et al., 2013). The thinning in the Mississippian strata is caused by the significant uplifting and erosion of the mid-continent (Watney et al., 2001). This environment has resulted in commonly acknowledged facies within the Mississippian carbonates, ranging from shale, chert conglomerate, tripolitic chert, dense chert, altered chert-rich limestone, dense limestone, to shale-rich limestone (Lindzey et al., 2015). In the study area, tripolitic chert is most prevalent in the Upper Mississippian zones and rapidly decreases in abundance at depths greater than 150 ft (45.7 m) below the pre-Pennsylvanian unconformity (Lindzey et al., 2015).

The Mississippian strata underwent four stacked transgressive-regressive cycles, which make up one third-order transgressive-regressive cycle bounded by unconformity surfaces above and below (Manger, 2014) who proposes that sufficiently drops in reletive sea level would lead to exposure of the sponge mounds, thus allowing for weathering and

diagenetic alteration. In the study area, diagenesis left intensely altered Mississippian Limestone after deposition, where one of the most prominent of these diagenetic features is silica replacement (Lindzey et al., 2015). Water flowed through the pores and redistributed the siliceous volcanic ash and some macrofossils, which left extensive micro-scale porosity (Lindzey et al., 2015). This dissolved silica precipitated in pore space, partially or completely replacing some carbonate fossils (Lindzey et al., 2015). Pore sediment structures are not well preserved due to the strong diagenetic overprint. Chert nodules are present, especially in highly reworked and bioturbated zones. Fractures are often filled with silica or calcite (Costello et al., 2013).

Tectonic deformation and diagenetic alteration of the rock are the two leading causes of fracturing in the Mississippian (Cook, 2016). Mazzullo et al. (2011) found that fracturing in the Mississippian Limestone is associated with lithology, such that fractures occur more often in the more brittle chert and limestone, and less often in shaly limestone. Diagenesis of the chert and cherty limestone as described above could also contribute to fracture intensity in the chert and cherty limestone lithofacies (Manger, 2014). Manger highlights shrinkage fractures from de-watering along a deeper portion of Mississippian Limestone section Roadcut in Arkansas. Young (2010) found that fracturing in the Mississippian occurred due to diagenesis during subaerial exposure that occurred during uplift and erosion, burial, and hydrothermal alteration post burial. Trumbo (2014) speculated that fracturing in the Mississippian contributes to intermittent production in vertical wells in reservoirs with no matrix porosity.

METHOD

Aberrancy

The detailed description of aberrancy computation can be found in Qi and Marfurt (2018). After rotating the (x_1, x_2, x_3) coordinate system to one oriented about the reflector dip and each voxel, the apparent aberrancy (or flexure), $f(\psi)$ at azimuth ψ is

$$f(\psi) = \frac{\partial^2 p_1'}{\partial x_1' \partial x_1'}\cos^3\psi + \frac{3}{2}\left(\frac{\partial^2 p_1'}{\partial x_1' \partial x_2'} + \frac{\partial^2 p_2'}{\partial x_1' \partial x_1'}\right)\cos^2\psi \sin\psi + \frac{3}{2}\left(\frac{\partial^2 p_1'}{\partial x_2' \partial x_2'} + \frac{\partial^2 p_2'}{\partial x_1' \partial x_2'}\right)\cos\psi \sin^2\psi + \frac{\partial^2 p_2'}{\partial x_2' \partial x_2'}\sin^3\psi, \quad (1)$$

where the primes indicate the rotated coordinate system and where p_1' and p_2' are the dip components along rotated axes x_1' and x_2' measured in m/m.

The extrema of the aberrancy are computed by setting the value of $\partial f(\psi)/\partial\psi$=0. Recall that vector dip, **p**, is computed using the first derivative of the surface, $z(x_1, x_2)$, and has one extrema, the dip magnitude, and the dip azimuth, which define a single dip vector. Also recall that curvature is computed using the second derivatives of the surface $z(x_1, x_2)$ and has two extrema, the most-positive and most-negative principal curvatures and their strikes. Aberrancy is computed using the third derivatives (equation 1) of the surface $z(x_1, x_2)$ and therefore will have in general three extrema. We will call these extrema the maximum, intermediate, and minimum aberrancy vectors expressed by its magnitude, $f(\psi)$ and its azimuth ψ. The numerical roots of the minimization problem are in terms of tan ψ, such that initially ψ ranges between $\pm 90^0$. Inserting these roots into

equation 1 may provide negative values of aberrancy $f(\psi)$. It is obvious that a negative flexure to the north is equivalent to a positive flexure to the south. For this reason, in our implementation, we define our resulting maximum, intermediate, and minimum aberrancy magnitudes, f_{max}, f_{int}, and f_{min}, to be strictly positive, with the corresponding azimuths ψ_{max}, ψ_{int}, and ψ_{min} ranging between $\pm 180^{\circ}$.

The analysis and display of three roots can be cumbersome. A simple fexure is represented by a finite value of f_{max}, with $f_{int} = f_{min} = 0$. Intersecting flexures give rise to non-zero values of f_{min} and f_{int}. We hypothesize that non-zero values of $\mathbf{f_{int}}$, and $\mathbf{f_{min}}$, may be indicators of increased shear strain giving rise to fractures measureable by image logs. For structural interpretation such as picking faults, we use the total vector aberrancy, $\mathbf{f_{tot}}$, which is simply the sum of the three aberrancy vectors.

Seismic data, mud logs and image logs

In 2010, Chesapeake Energy acquired a 400 mi^2 (1036 km^2) 3D seismic survey in Woods County, Oklahoma **(Figure 3.1a)**. The seismic processing workflow included refraction statics, velocity analysis, residual statics, prestack time migration, frequency-space-time predictive noise rejection, and bandpass filtering. The overall data quality is excellent. The signal to noise ratio (S/N) is relatively high and the wavelet amplitude appears continuous throughout the Mississippian target **(Figure 3.1b)**. The data set includes digital well logs and mud logs for 83 wells, consisting of 52 horizontal and 31 vertical wells. For the cost of penetration (COP) calibration analysis, we will only use the horizontal wells. The horizontal well data consisted of 52 gamma-ray logs, 51 mud logs, with 18 of them being open-hole logs. Building on our previous findings (Qi et al., 2017),

we examine 51 horizontal wells drilled by the same operator in a similar time period; allowing us to assume consistency between the wells regarding weight on bit, mud type, and bit type. The mean and standard deviation of COP for the 51 horizontal wells resulted in two categories: high and low COP with average value of 27 and 2.5 min/ft (89 and 8.2 min/m), respectively (**Figure 3.3**).

For the borehole image logs calibration analysis, five electrical borehole image logs were interpreted from electrical borehole imaging tools to map open conductive fractures by our colleague Stephanie Cook **(Figure 4.1)**. Both open, conductive fractures and mineralized, non-conductive fractures were observed in borehole images (Cook, 2016). However, the mineralized, non-conductive fractures were removed from her interpretation results. The fracture intensity log is calculated by taking the area of the fracture surface and then dividing by the unit volume of the borehole along one foot increments resulting in measurements exhibiting units of $ft^2/ft^3 = 1/ft$ (**Figure A1**). A detailed description of the borehole image interpretation can be found in Cook (2016).

Analysis

Pre-stack inversion and seismic-attribute volumes were generated for the Mississippian Limestone target and converted to depth. The detailed description of seismic depth conversion can be found in Qi et al., (2017). Geomechanical rock properties (from seismic inversion) and seismic-attribute values were then extracted along each wellbore every 110 ft (34 m) corresponding to the well-coordinate system from both mud logs and image logs. We applied a 110 ft (34 m) sliding Backus averaging window to the

fracture area logs and mud logs to upscale them to the seismic 110 ft by 110 ft bin size (**Figure A2**). Assuming that fractures directly influence permeability, Backus averaging provides an appropriate upscaling useful for fluid flow calculations (Cook, 2016). Likewise, Backus averaging preserves the time taken to drill through a given well distance. Once upscaled, we construct a vector of seismic geometric and geomechanical attributes at 110 ft increments along each horizontal well bore.

Neural network is a generic name for a large class of machine learning algorithms, including but not limited to perceptrons, Hopfield Networks, Boltzmann Machines, Fully Connected Neural Networks, Convolutional Neural Networks and many more (Krizhevsky et al., 2012). In the late 1980s, Fully Connected Neural Networks were the most popular neural network algorithm used. Unfortunately, this type of network has a large number of parameters, and does not scale well (Krizhevsky et al., 2012). This network has been superceded by the less fully connected Convolutional Neural Network (CNN), where neurons share weights and each neuron is connected to only a few neurons in the previous layer. CNNs have been successfully appied to problems in computer vision and signal processing (Krizhevsky et al., 2012). A CNN consists of sequence of layers, and the three main types of layers to buid CNN are convolutional layers, max-pooling, and fully-connected layers. In our fracture prediction study, we first train and validate the CNN using the known fracture density data interpreted from five image logs, and then predict the fracture density in the unknown region. The input to the CNNs are eight seismic attributes extracted along the boreholes, which are then transformed using 15 hidden layers **(Figure 4.2)**. The algorithm evaluates alternative weights, **W**, and

biases, **b,** at each hidden layer of the CNN, that when combined with the output of other layers, provides a nonlinear prediction of the measured fracture density training data (Hagan et al., 1996). In this study, we used 15 hidden layers, with intermediate results from each layer passed to the last fully-connected output layer to support regression (**Figure 4.2)**. The algorithm iterates until it "learns" the relationship (finds the optimum values of **W** and **b**) between the input attributes and fracture density**.** 179 eight-element vectors were used to train the CNNs, with the proportion of 70% (125 samples), 15% (27 samples), and 15% (27 samples) to train, validate, and test the model, respectively. The CNN analysis is conducted using a Neural Network Toolbox developed by MATLAB R2017b (Mathworks, 2017).

RESULTS

Coherence andcurvature

Coherence measures the similarity between waveforms on neighboring traces, and helps delineate faults and other discontinuities in the seismic data. In contrast, curvature measures more continuous reflector deformation, with folded reflectors exhibiting high curvature and planar reflectors zero curvature. When calibrated to image logs, most-negative and most-positive curvature can serve as a means of predicting fractures from surface seismic data (Chopra and Marfurt, 2007). The horizon slice in Figure 4.3 alongh the top Mississippian Limestone in this survey shows two large strike-slip faults (yellow arrows) and one reverse fault (white arrow). One strike-slip fault runs from the northeast corner all the way to the southwest corner of the survey where the target horizon is

upthrown to the northwest and downthrown to the southeast; the second strike-slip fault extends in southeastern portion of the survey. The reverse fault runs north-south, extending south of the strike-slip fault described above. Notice that the major faults exhibit a positive curvature anomaly on the footwall, which is laterally offset from a corresponding negative curvature anomaly on the hanging wall. The offsets of the large northeast-southwest strike-slip fault can be as large as 100 ft (Cook, 2016).

Aberrancy

Aberrancy measures the lateral change of the curvature along a picked or inferred surface, and not only detects major faults that exhibits finite displacement, but also more subtle "sub-seismic-resolution" faults that appears as flexures (Qi and Marfurt, 2017). **Figure 4.4** shows the same slices as in the previous image, but now through the total aberrancy volume. The total aberrancy vector provides a single vector volume appropriate for structural interpretation. The previously identified strike-slip and reverse fault indicated by white and yellow arrows are delineated by total aberrancy. Blue arrows indicate several additional flexures seen in the horizon slice.

Geomechanical and texture attributes

The next suite of attributes which contributed to fracture characterization are geomechanical attributes. Using prestack seismic inversion, we computed lambda-rho, mu-rho, and P-impedance volumes. The P-impedance measures the product of density and seismic P-wave velocity. Lambda-rho and mu-rho are used to estimate lithology and geomechanical behavior such as brittleness index (Perez and Marfurt, 2013; 2015) (**Table**

4.1). We also constructed a chaos volume, faults and fractures result in more disorganized image (**Figure 4.5**).

Aberrancy calibration

To investigate the interpretational value of the minimum, intermediate, and maximum aberrancy (aberrancy vectors), we performed both qualitative (visualization) and quantitative (numerical) analysis. We first display five image logs against the aberrancy attributes (**Figure 4.6-4.10**). Recall that there are three aberrancy attribute vectors. For a simple linear flexure there is only one aberrancy vector – the maximum aberrancy. Flexure that defined a curved fault or fold, or flexures that cut other flexures give rise to non-zero minimum and intermediate aberrancy vectors. Examining Figure 4.8, note that high values of the minimum y and intermediate aberrancy magnitude indicated by the white arrow correlate with relatively low areas of fracture density area. In contrast, high values of maximum aberrancy magnitude correlate with areas of relatively high fracture density area indicated by yellow arrows in **Figure 4.7**. Because total aberrancy is the vector sum of three aberrancy vectors, high total aberrancy magnitude values correlate with both relatively low and high fracture density indicated by white and yellow arrows (**Figure 4.6**), indicating that this may be a poor candidate to use in fracture prediction.

To further evaluate these relations, we calculated the linear correlations between each of four aberrancy magnitude volumes and fracture density. The model shows a correlation of an increase in fractures with decreases in both minimum aberrancy, f_{min}, and intermediate aberrancy, f_{int}, magnitude (**Figure 4.11**). In contrast, there is an increase

in fractures correlate with an increase in the maximum aberrancy magnitude, f_{max}. These correlations suggest that the total aberrancy is more helpful for interpreters in highlighting subtle features. The minimum and the intermediate aberrancy is mostly helpful in finding smooth area.

Aberrancy vectors are not always correlated with fracture density, the results may limit by relatively low seismic image resolution compared to image logs and uncertainties in image logs interpretation. Both the averaged fast and slow ROP doesn't seem to have statistically significant correlations with fracture intensity, and the results are presented in the appendix (**Figure B1, B2**).

CNN prediction of fractures

Before training the CNNs model, we first performed a multi-linear regression analysis to calculate and select which of the attributes could be used to train a fracture density model that would best simulate the interpreted fracture density throughout the seismic volume (**Figure 4.12**). With the multi-linear regression, more than one step is taken to come to the best solution, where the best fit to the data requiring a reiterative process. First, one computes an initial estimate of the correlation for each attribute. Then, in the multi-linear regression process, different attributes are combined to improve the fit of the curve to the data. These iterations continue until the process converges. The resulting attribute correlations must also be examined to be geologically reasonable. For example, higher fracture intensity may be expected to be seen with smaller values of coherence. If a candidate attribute shows a correlation counter to findings in previous studies and geologic knowledge, that attribute should be taken out of the multi-linear

regression model. To avoid over training the model by incorporating too many seismic attributes, of the 22 seismic attributes examined, only eight were retained in the final model.

Eight statistically representative attributes were picked to correlate with fractures, aberrancy, coherence, lambda-rho, mu-rho, P-impedance (Z_P), chaos, envelope, and instantaneous frequency (**Figure 4.11, 4.12**). Figure 4.12 present linear correlations for each attribute with fracture density in order of their significance to the model. There is a negative correlation between fracture density and coherence, such that an increase in fractures density corresponds with a decrease in coherence. Two complex trace attributes, Instantaneous frequency and amplitude (envelope) were picked to correlate with fracture density. Envelope represents the acoustic impedance contrast and can be a good indicator of major changes of lithology or thickness (Chopra and Marfurt, 2007). The increases in fracturing correlated with increases in envelope. The chaos attribute is computed based on eigen-analysis of gradient covariance (Chopra and Marfurt, 2016). The larger the value is, the smoother the image is. There is a negative correlation between chaos and fracture density.

The cross plots confirm that all three of prestack inversion attributes exhibit negative nonlinear correlation with fracture density. This correlation is likely a result of fractures from the heterogeneous formation. Cook (2016) confirmed five rock types were seen on image logs. The first rock type was chert, with only a small percentage of the wellbores with the borehole image logs contained pure chert. The areas that contained chert except karsted chert were moderately fractured. The second rock type was cherty

limestone, which exhibited no fractures in the area. The third and fourth rock types were limestone and highly fractured limestone. As the most abundant lithology present in the borehole image logs, there was some limestone that had little to no fractures, while some limestone was heavily fractured, suggesting factors other than lithology play a role in fracture genesis (Cook, 2016). The last rock type was in the area of karsting.

All of the attributes appeared complicated nonlinear relationship with fractures. Thus we choose CNNs to recognize the fracture pattern in the unknown area. We compared the performance of multi-linear regression model with the CNNs against successive combinations of attributes, the R-square value is always higher using CNNs (**Figure 4.13**). After training, validation, and testing the CNNs model, we successfully estimated fracture density across the Mississippian Limestone horizon (**Figure 4.15**). The resulting fracture training model had the training R^2-value of 0.781, validation R^2-value of 0.426, test R^2-value of 0.564, and a total R^2-value of 0.675 (**Figure 4.14**). **Figure 4.16** display one representative fracture area log against predicted fracture intensity model. Many of the increases and decreases in fracture intensity line up between the model and the fracture area logs. The model was able to predict much of the same fracture intensity trends along Mississippian Limestone horizon, though some areas also have some discrepancies from the original interpretation of fracture area. Observing the predicted fracure density model, there is an increase in fracture density along known mapped faults in the survey (**Figure 4.15**). Increases in predicted fracture density could be an area contain a higher probability of tripolitic chert (Lindzey et al., 2015).There are areas of zero fracture density along the perimeter of the seismic survey or formed into

magenta square, which is assumed to be the edge effect or no-permit zones in the seismic survey. Lastly, in the southeastern part of the survey, strong correlation was reported between predicted fracture density and a known area of heavy karsting (Cook, 2016).

Azimuthal intensity was computed from the maximum aberrancy vector from azimuth -90°, -60°, -30°, 0, 30°, and 60°. Azimuthal intensity was extracted onto a surface of the Mississippian Limestone (**Figure 4.17**). Azimuthal intensity at 60º correlated best with estimated fracture density with a correlation coefficient of 0.72, while azimuthal intensity at 0º correlated the worst with estimated fracture density with a correlation coefficient of 0.58. This azimuthal correlation match well with Cook, (2016) image log interpretation. She pointed out that most of the natural fracturing and faulting in the study area runs -30° from the west – east maximum horizontal stress.

CONCLUSIONS

Edge-detecting seismic attributes are widely used to highlight faults and other discontinuities. Volumetric aberrancy anomalies would track the coherence anomaly and highlight sub-seismic faults and flexures. This is the first study explores whether volumetric aberrancy can be statistically correlated to fractures and therefore use it predict fractures in undrilled parts of the survey.

A suite of geometric and geomechanical attributes were generated for the Mississippian Limestone target containing five interpreted borehole image logs and 52 mud log. With the use of Convolutionary Neural Network, eight seismic attributes were used to model fractures seen on the image logs over the Mississipppian Limestone

horizon. Of these attributes, high values of minimum aberrancy and intemediate aberrancy correlate with low fracture density, while high values of the maximum aberrancy anomalies correlate with higher fracture density. In figure cross plots of all eight aberrancy attributes, there is a clear negative correlation between fracture density and coherence. Three geomechnical attributes exhibit negative nonlinear coorelation with fracture density. This nonlinear coorelation is likely a result of fractures from the heterogeneous formation. No statistically significant correlations were found between aberrancy vectors and rate of penetraion.

With the estimated fracture density model, higher fracture density was observed along known mapped faults in the survey. Some higher fracture density region can be assoicated with tripolitic chert deposits. The maximum aberrancy correlated best with estimated fracture density at 60° with a correlation coefficient of 0.72.

While we calibrated four aberrancy vectors using image logs, the total aberrancy is more helpful for interpreters in highlighting subtle features, the azimuthal fracture intensity extracted from the maximum aberrancy vector can be a good indicator of estimating azimuth of natural fracturing and fault.

CHAPTER 4 TABLES

Attribute name	Measures	Hypothesis
Aberrancy, **f**	Flexures	Greater strain induces more fractures
Instantaneous frequency	The rate of change of instantaneous phase	Fracture results in change of lithology and thickness of beds
lambda-rho, $\lambda\rho$	product of shear module and density	With mu-rho, can differentiate brittle rocks from ductile rocks
Chaos	Eigen-analysis of gradient covariance	Fracture results in more disorganized image
Mu-rho, $\mu\rho$	Product of shear module and density	With lambda-rho, can differentiate brittle rocks from ductile rocks
Envelope	Acoustic impedance contrast	Fracture results in lithology change
P-impedance, Z_P	Product of P-velocity and density	Fractures result in "softer", less dense rock
Coherence, *c*	Discontinuities	Faults and large joints may be directly detected; Subseismic resolution fractures occur in proximity to large faults.

Table 4.1. Summary of eight seismic attributes inputs and their hypothesized correlation to fractures.

CHAPTER 4 FIGURES

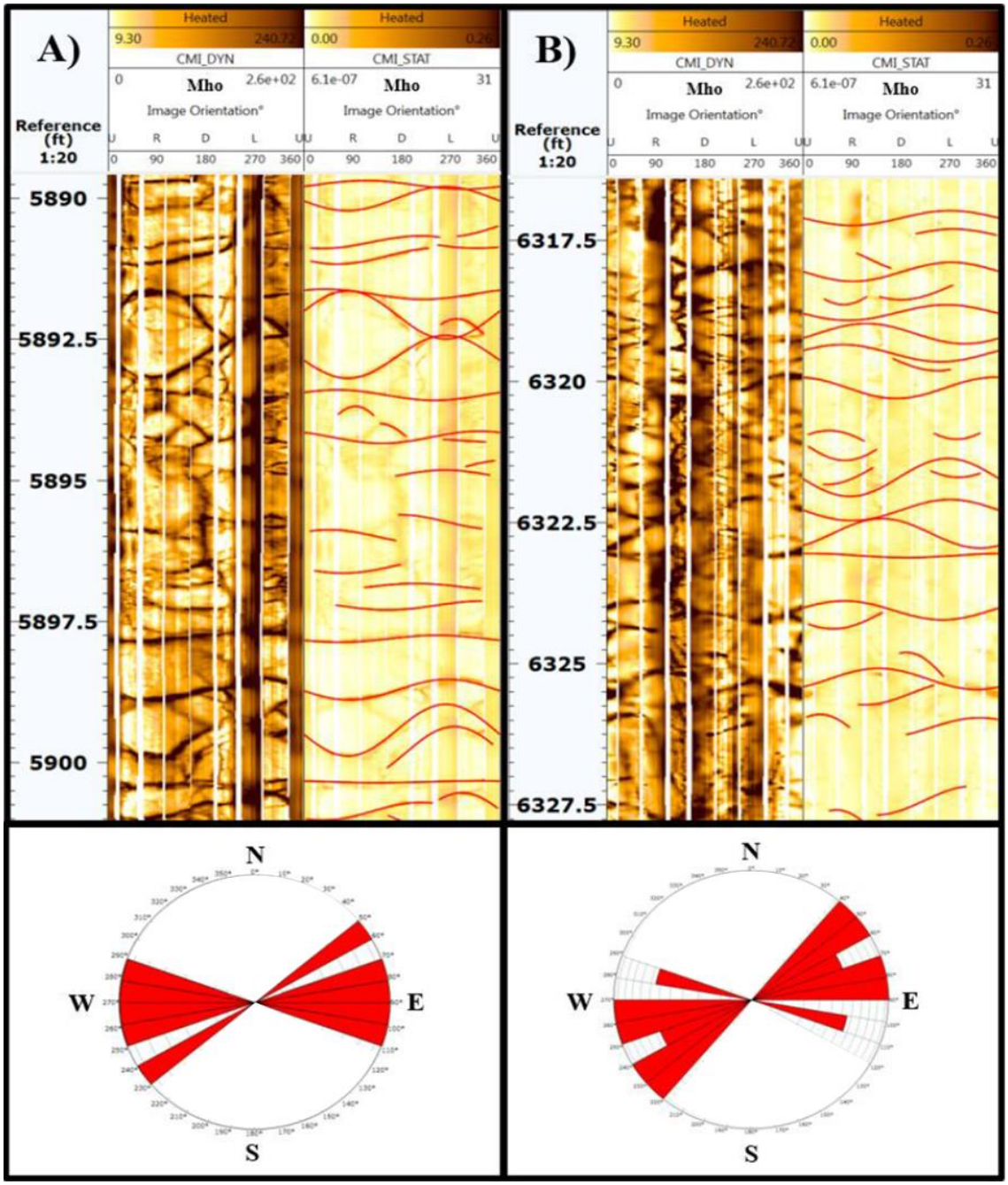

Figure 4.1. Examples of conductive fractures seen in a horizontal well where drilling mud filling the fracture planes appears as dark brown (high conductivity) against the lighter colored (lower conductivity) limestone and chert. The orientation of the image is indicated by up (U), right (R), down (D), and left (L) of the well circumference. The stereonets below the track show the strike of the fractures that cut through the entire borehole. (Modified from Cook 2016).

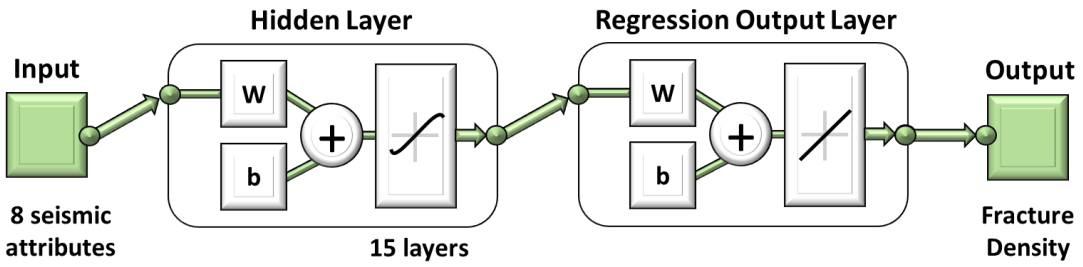

Figure 4.2. Diagram of Convolutional Neural networks (CNNs). This two-layer feed-forward network consists of 15 sigmoid hidden layers and one linear output layer. CNNs are made up of neurons that have learnable weights, **W**, and biases, **b**. The input to the CNNs include eight seismic attributes which are then transformed through 15 hidden layers. The hidden layer is connected to a regression output layer, which predicts the fracture density in the unknown region.

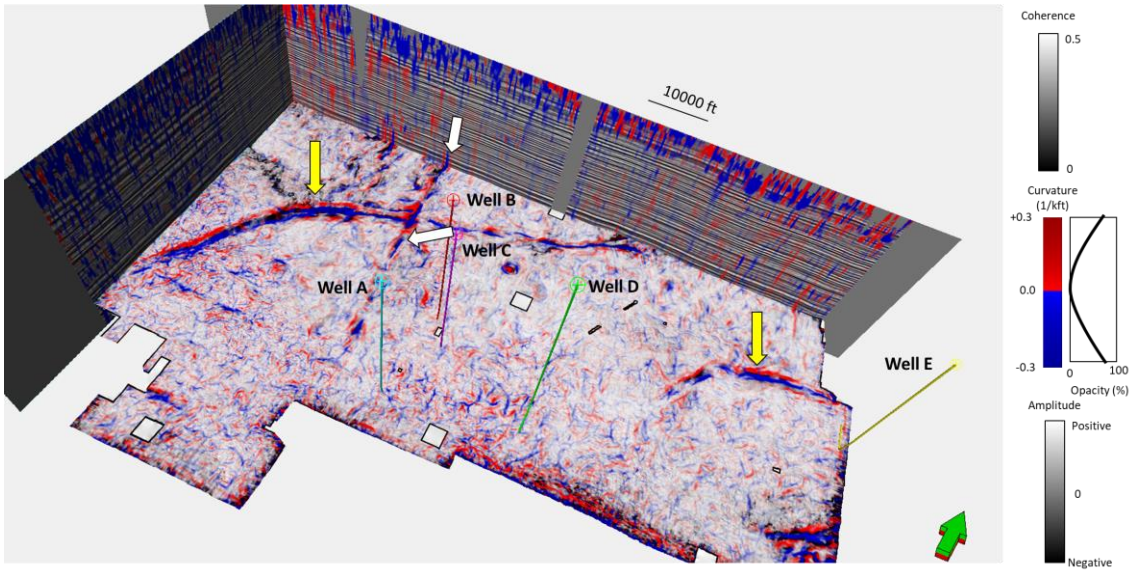

Figure 4.3. Co-rendered most-positive and most-negative curvature with seismic amplitude on the vertical slices. Horizon slice along the co-rendered top of Mississippian Limestone through the most-positive and most-negative curvature and coherence volumes showing five image log paths (wells A-E). Yellow arrows indicate two lateral strike-slip faults; one runs from the northeast corner all the way to the southwest corner of the survey, the other one extends in southeastern portion of the survey. White arrows indicate a reverse fault running north-south, extending south of the strike-slip fault described above. White squares correspond to no-permit zones in the seismic survey.

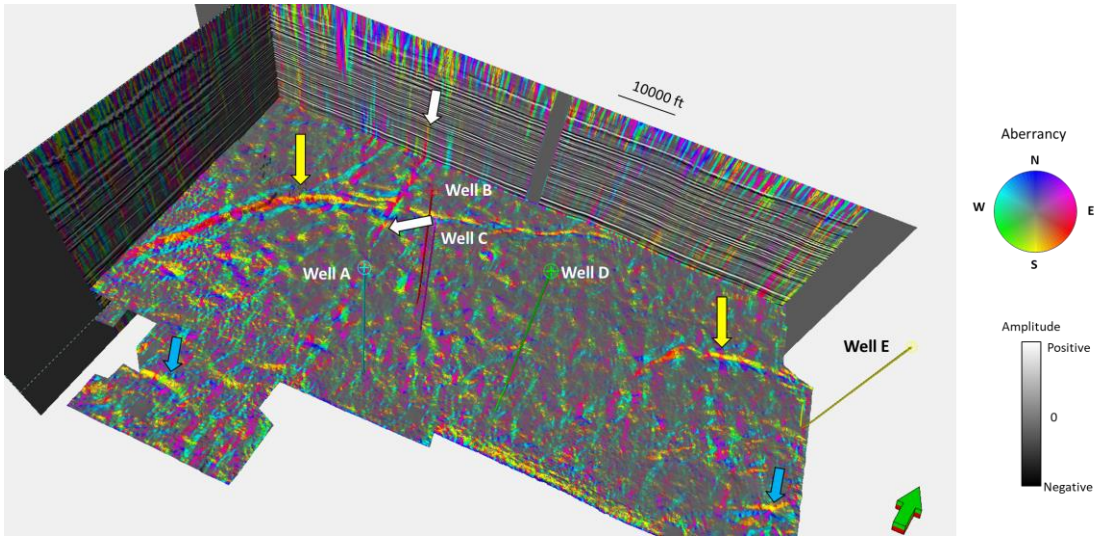

Figure 4.4. The same slices shown in the previous figures through the total aberrancy vector volume with five image logs path (well A-E). Yellow arrows indicate two lateral strike-slip faults. White arrows indicate a reverse fault running north-south, extending south of the strike-slip fault described above. Blue arrows indicate two (of many) flexures that do not exhibit a coherence anomaly.

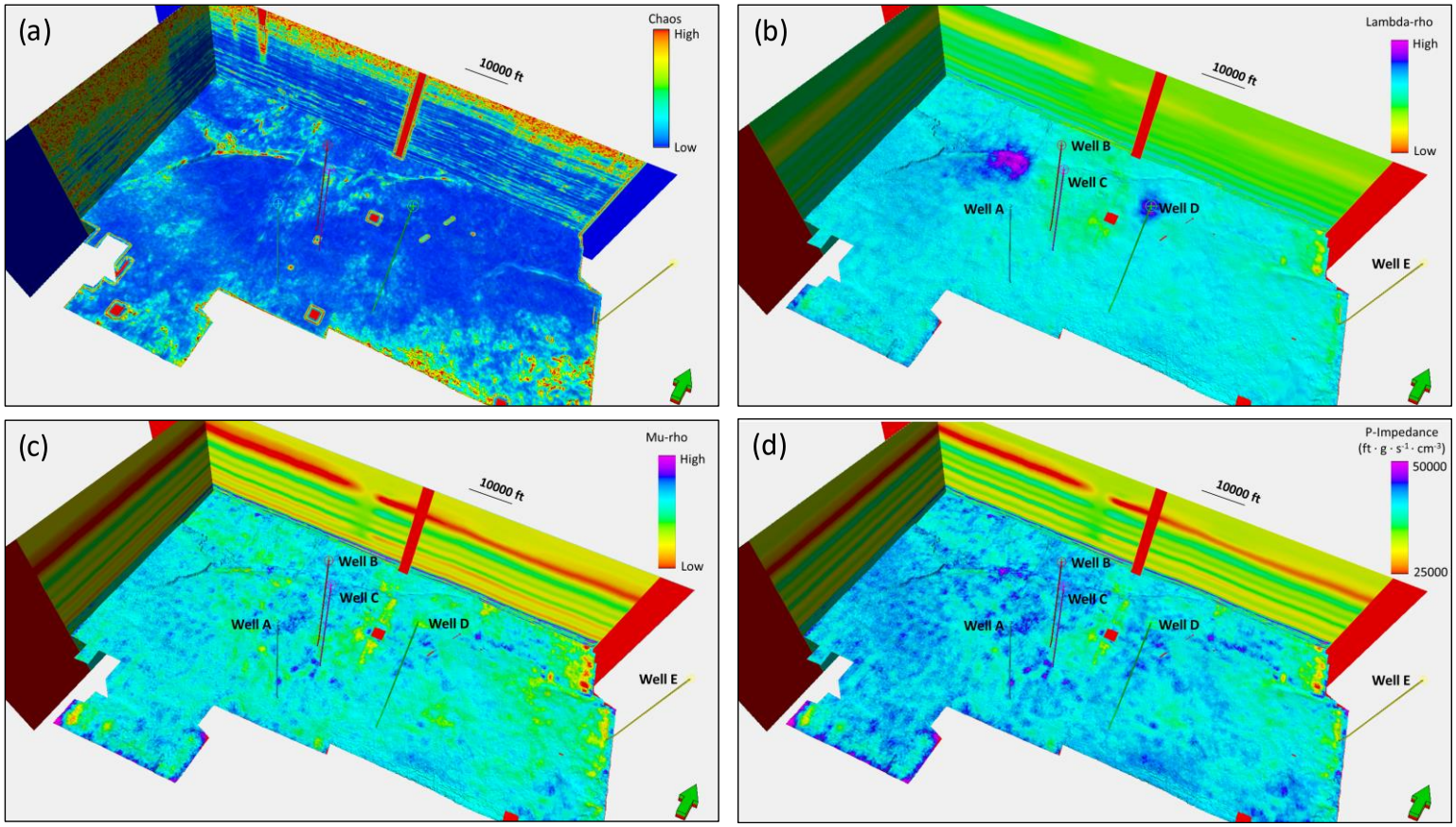

Figure 4.5. The same slices shown in the previous figures through (a) chaos, (b) lambda-rho, (c) mu-rho, and (d) P-impedance with five image logs path (well A-E).

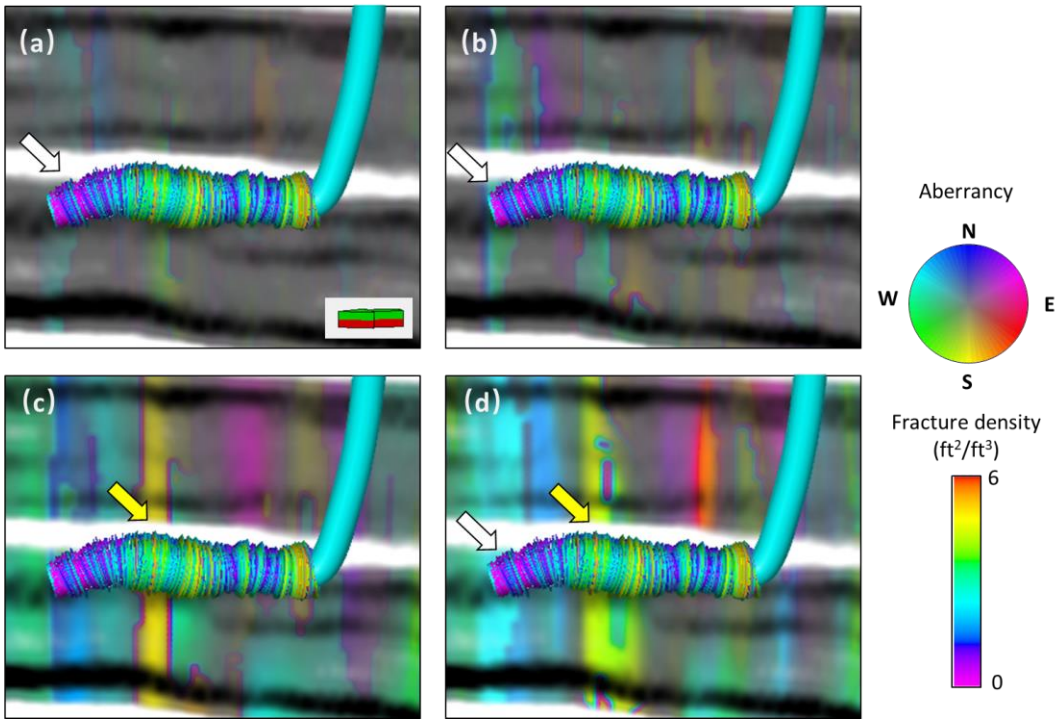

Figure 4.6. Interpreted well A fracture density plotted against (a) minimum aberrancy, (b) intermediate aberrancy, (c) maximum aberrancy, and (d) total aberrancy vectors. Yellow arrows indicate trends where higher aberrancy anomalies align with higher fracture density. White arrows indicate areas where the higher aberrancy values align with lower fracture density, suggesting it is not highly fractured.

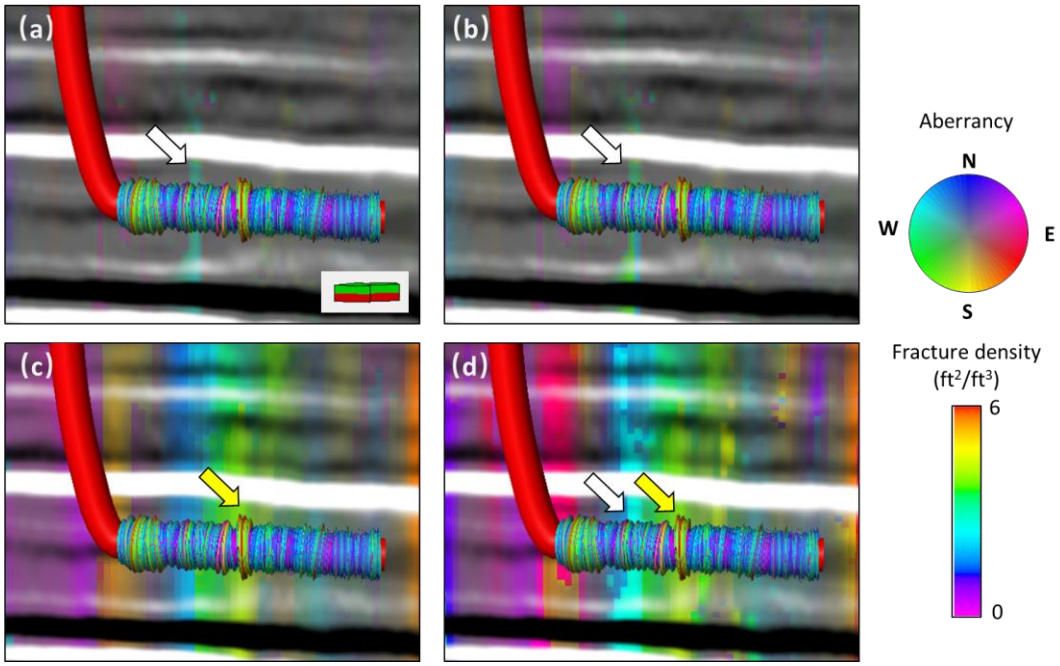

Figure 4.7. Interpreted well B fracture density plotted against (a) minimum aberrancy, (b) intermediate aberrancy, (c) maximum aberrancy, and (d) total aberrancy vectors. Yellow arrows indicate trends where the aberrancy anomalies align with higher fracture density. White arrows indicate the areas where the high aberrancy values align with lower fractures density.

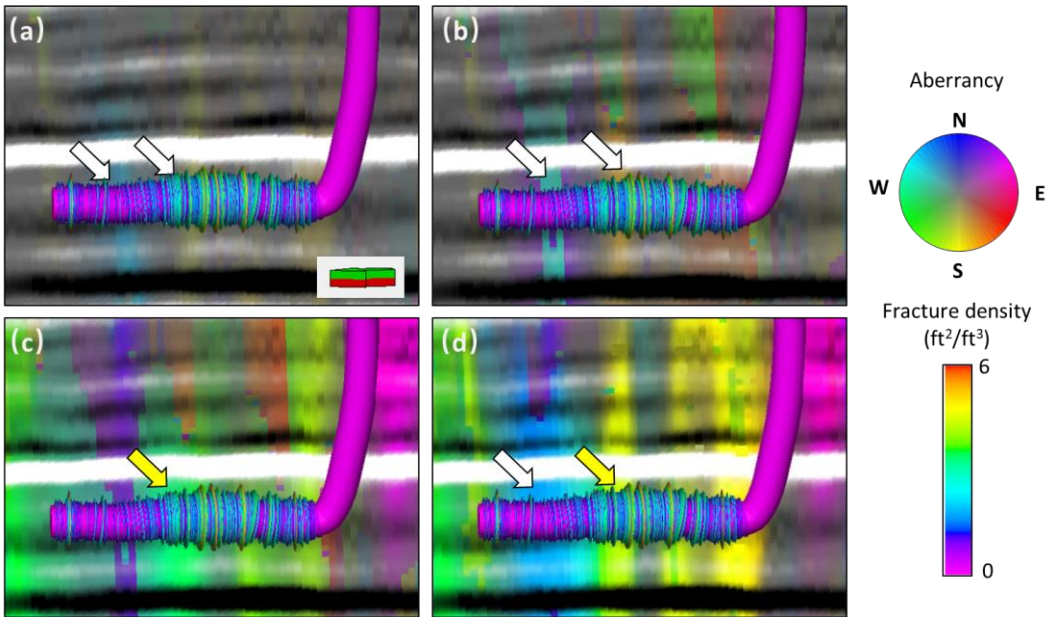

Figure 4.8. Interpreted well C fracture density plotted against (a) Minimum aberrancy, (b) intermediate aberrancy, (c) maximum aberrancy, and (d) total aberrancy vectors. Yellow arrows indicate trends where the aberrancy anomalies align with higher fracture density. White arrows indicate to the areas where the aberrancy values align with lower fractures density.

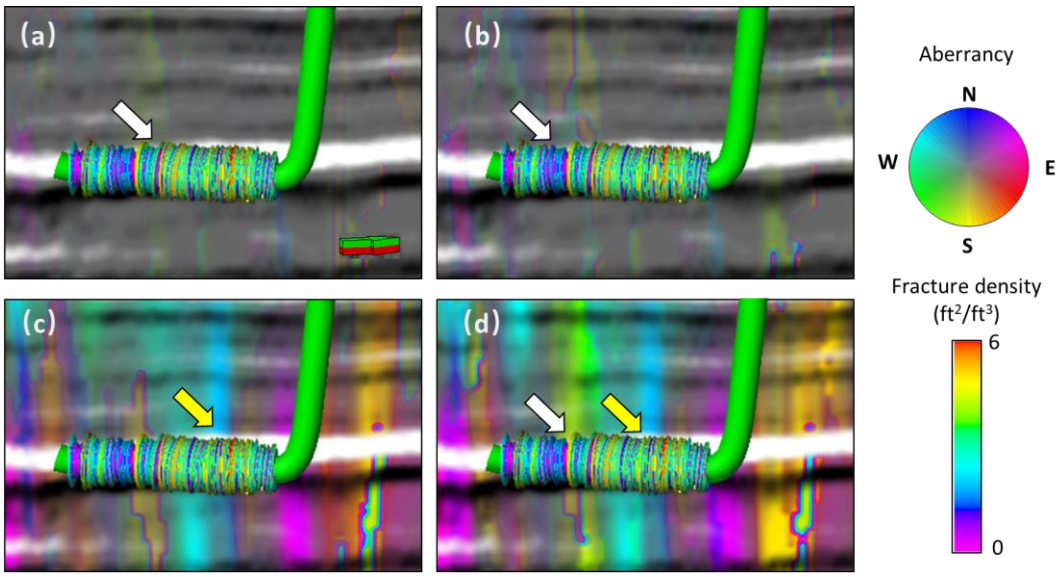

Figure 4.9. Interpreted well D fracture density plotted against (a) Minimum aberrancy, (b) intermediate aberrancy, (c) maximum aberrancy, and (d) total aberrancy vectors. Yellow arrows indicate trends where the higher aberrancy anomalies align with higher fracture density. White arrows indicate to the areas where the higher aberrancy values align with lower fracture density.

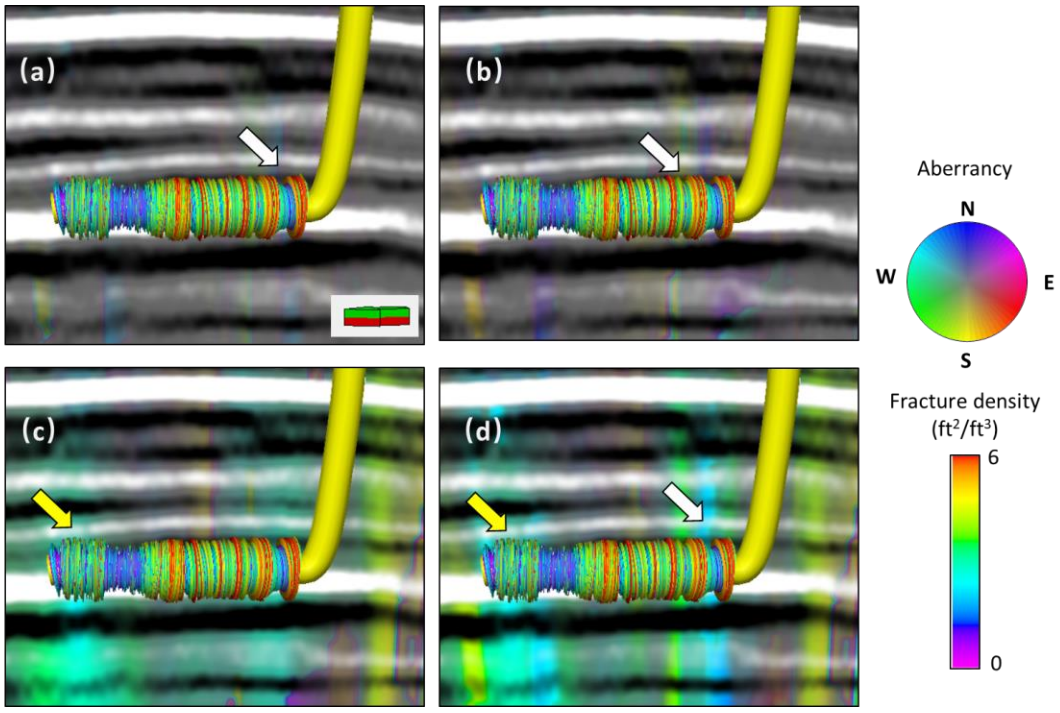

Figure 4.10. Interpreted well E fracture density plotted against (a) Minimum aberrancy, (b) intermediate aberrancy, (c) maximum aberrancy, and (d) total aberrancy vectors. Yellow arrows indicate trends where the higher aberrancy anomalies align with higher fracture density. White arrows indicate to the areas where the higher aberrancy values align with lower fracture density.

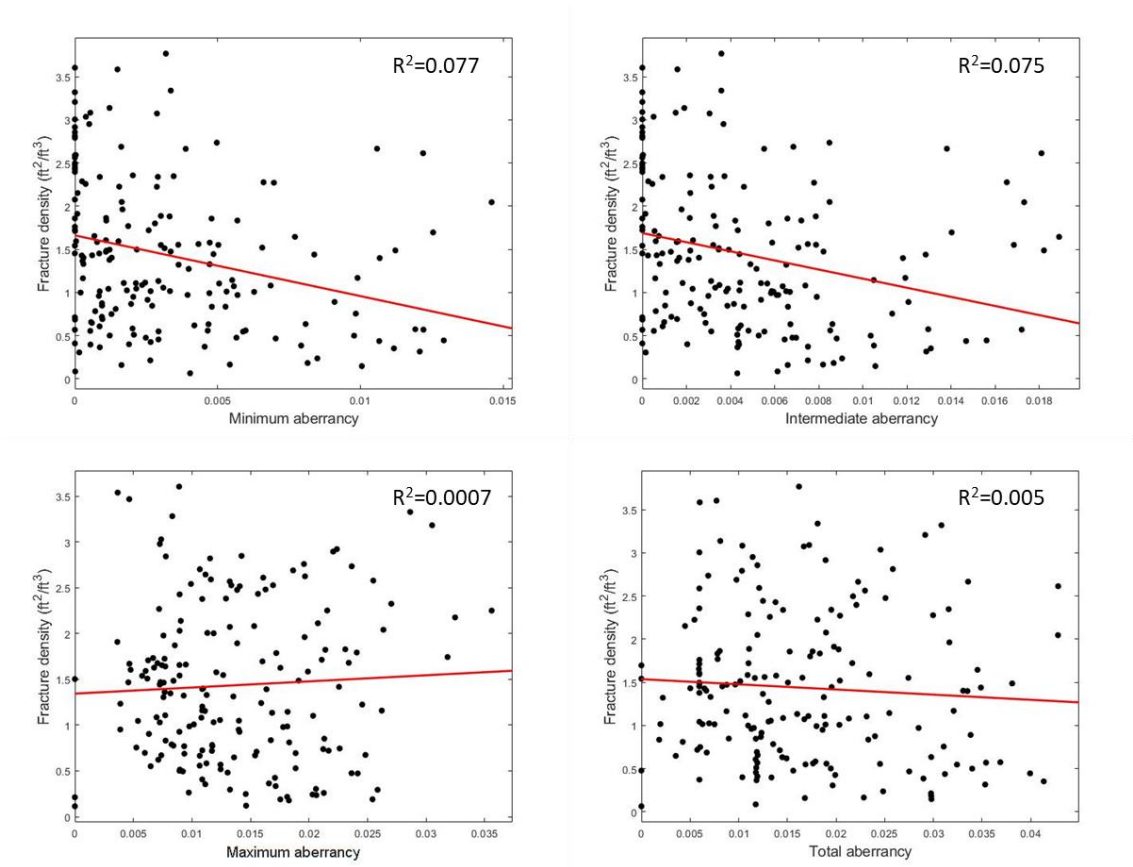

Figure 4.11. Four linear correlations between the magnitude of minimum, intermediate, maximum, and total aberrancy and fracture density. The red lines indicate the linear fit with the R^2 value at the upper right corner of each panel.

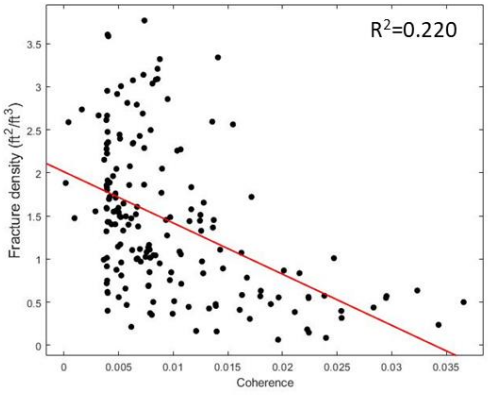
R2=0.220
Fracture density (ft2/ft3)
Coherence

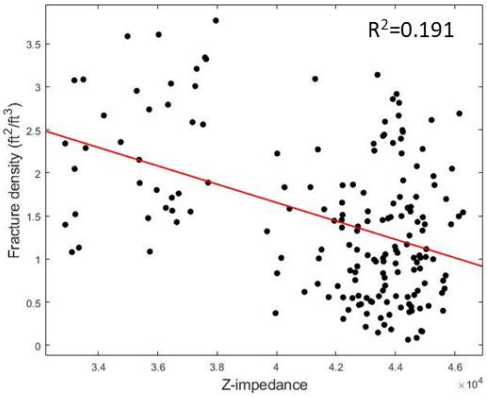
R2=0.191
Fracture density (ft2/ft3)
Z-impedance
×10^4

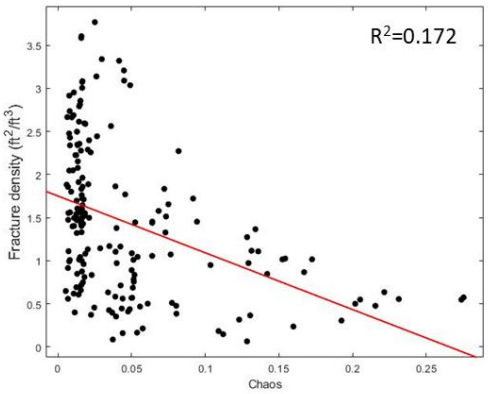
R2=0.172
Fracture density (ft2/ft3)
Chaos

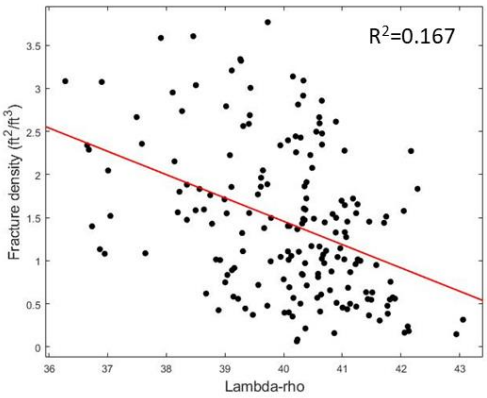
R2=0.167
Fracture density (ft2/ft3)
Lambda-rho

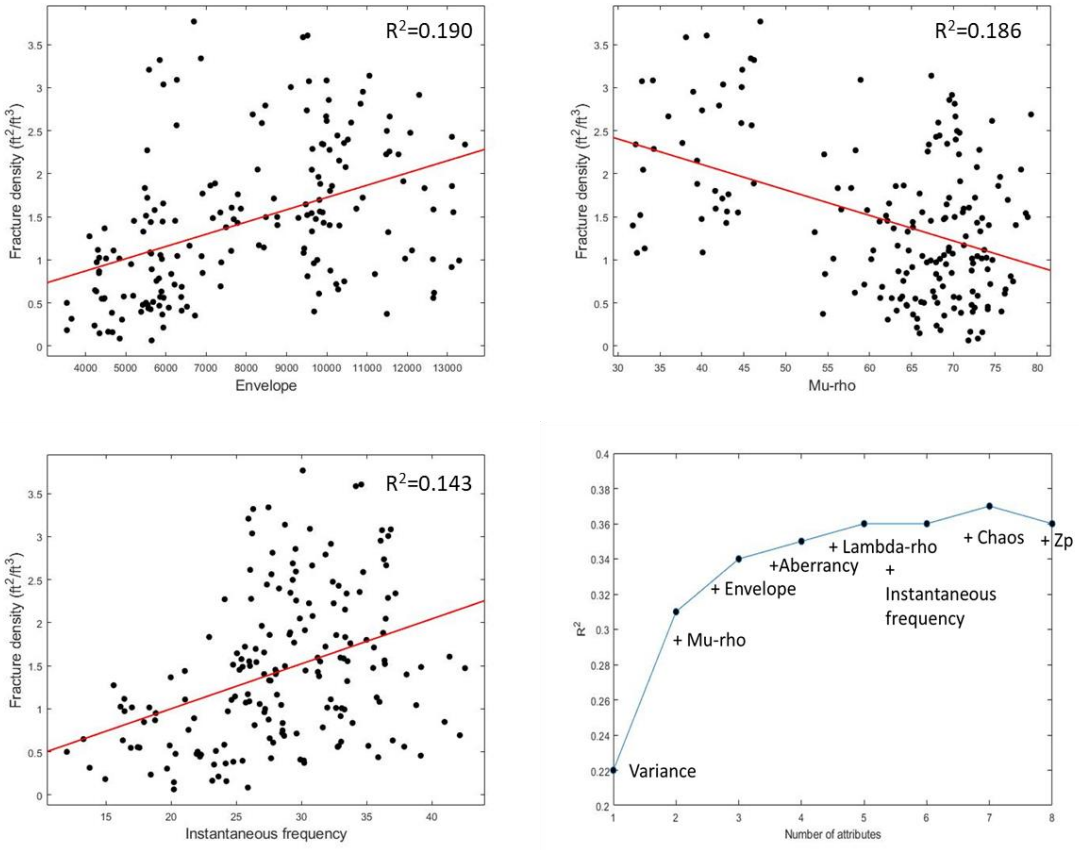

Figure 4.12. Seismic attribute input into the multi-linear regression model predicting fractures. The attributes are in order of their significance to the model. The last panel shows multi-linear regression against successive combinations of attributes.

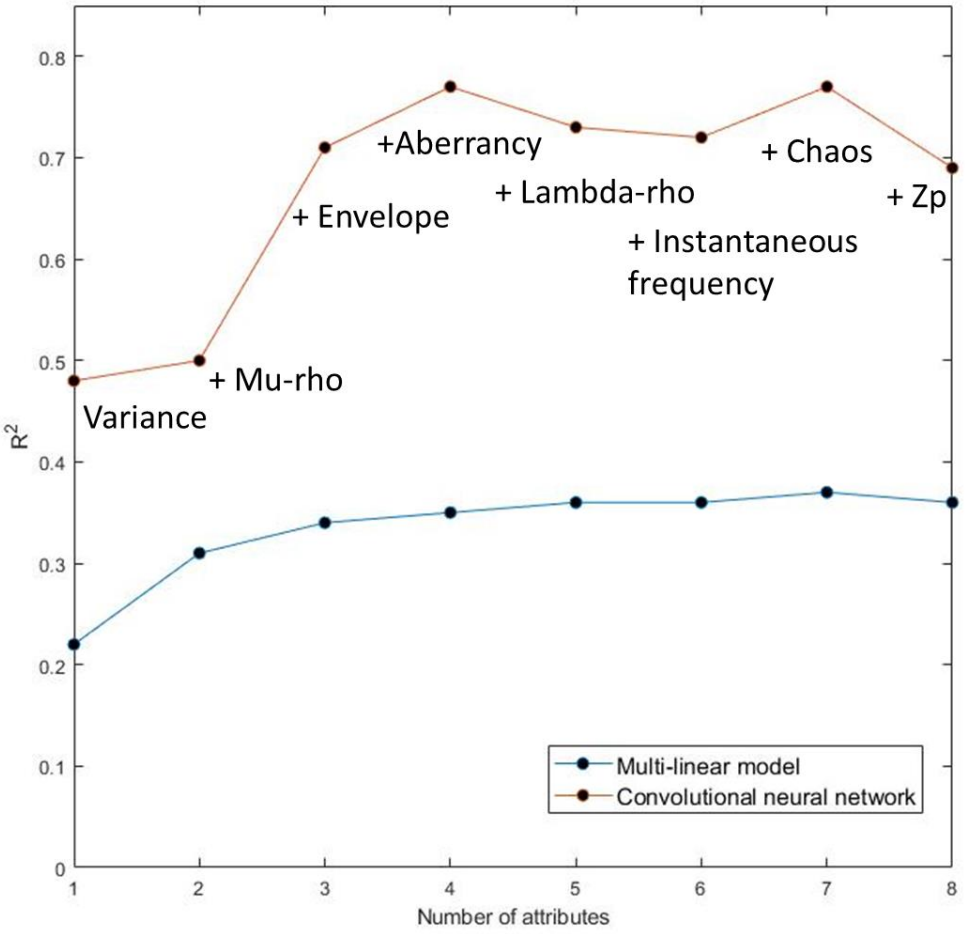

Figure 4.13. A comparison shows multi-linear regression and Convolutional Neural Network against successive combinations of attributes.

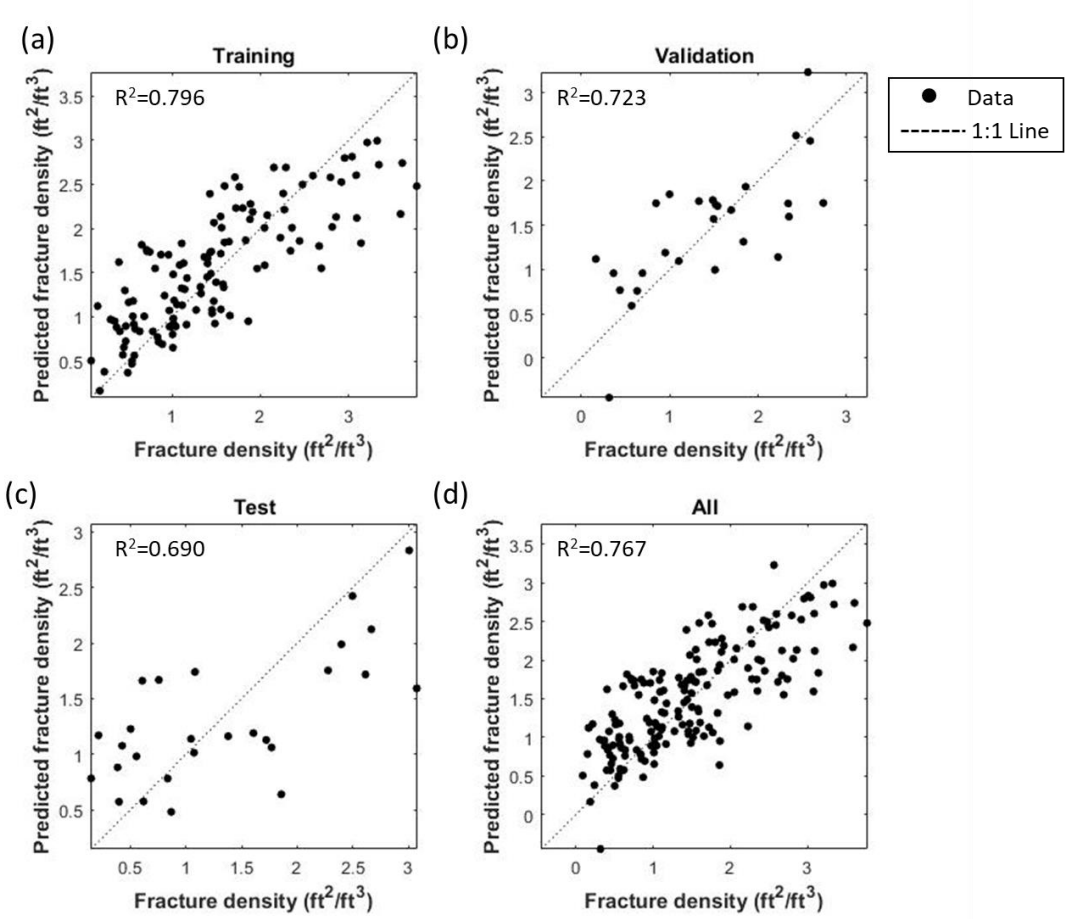

Figure 4.14. Performance of CNN model. Four panels showing results of training, validation, testing, and the complete data, with the training error R^2_{train}=0.796, validation error R^2_v=0.723 and testing error R^2_{test}=0.689 for the 1:1 Line.

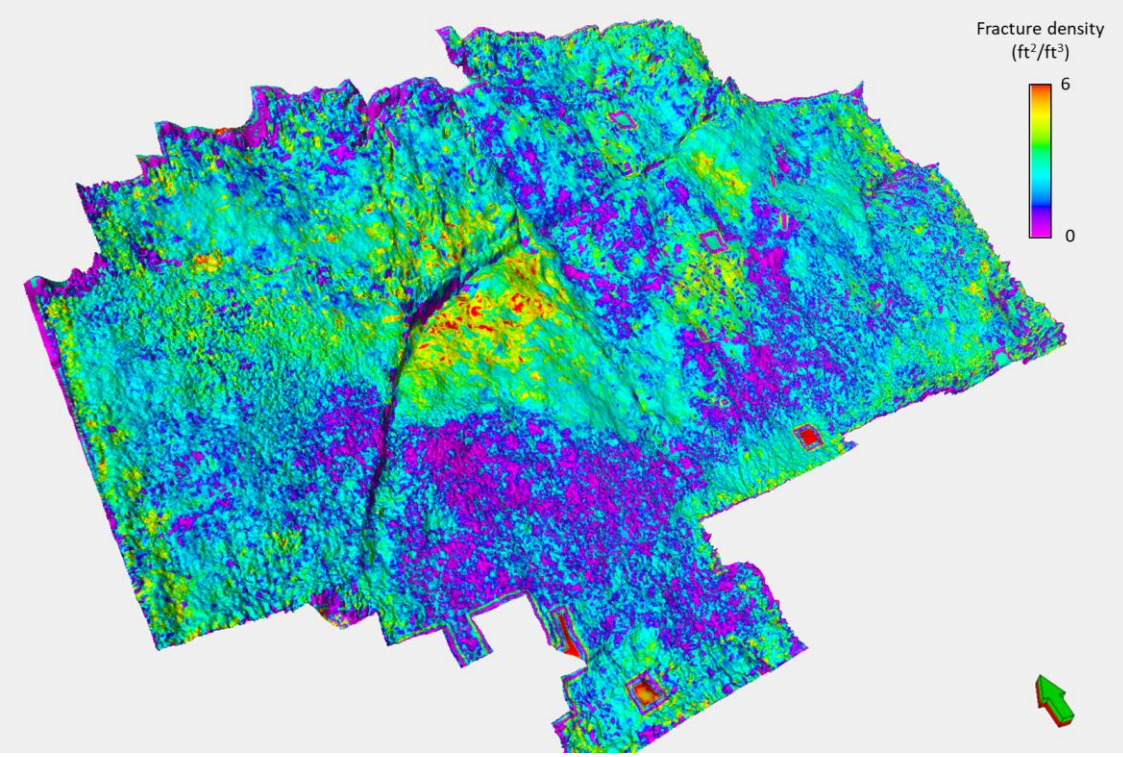

Figure 4.15. Horizon slice of predicted fracture density on the Mississippian Limestone computed using the eight attributes shown in Figures 4.11 and 4.12.

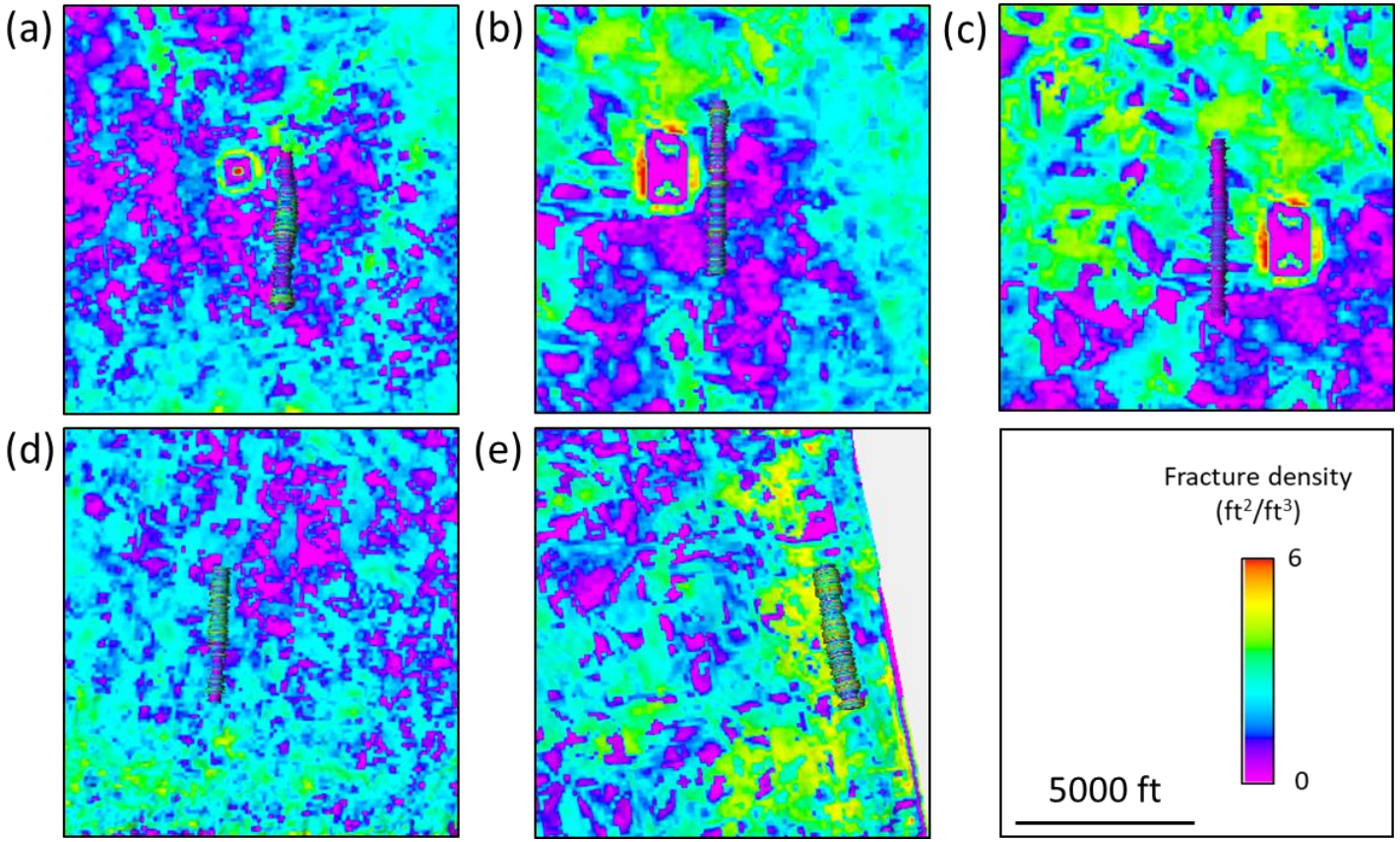

Figure 4.16. Five fracture density logs displayed against the predicted fracture density model. Many of the increases and decreases in fracture intensity line up between the model and the fracture area logs.

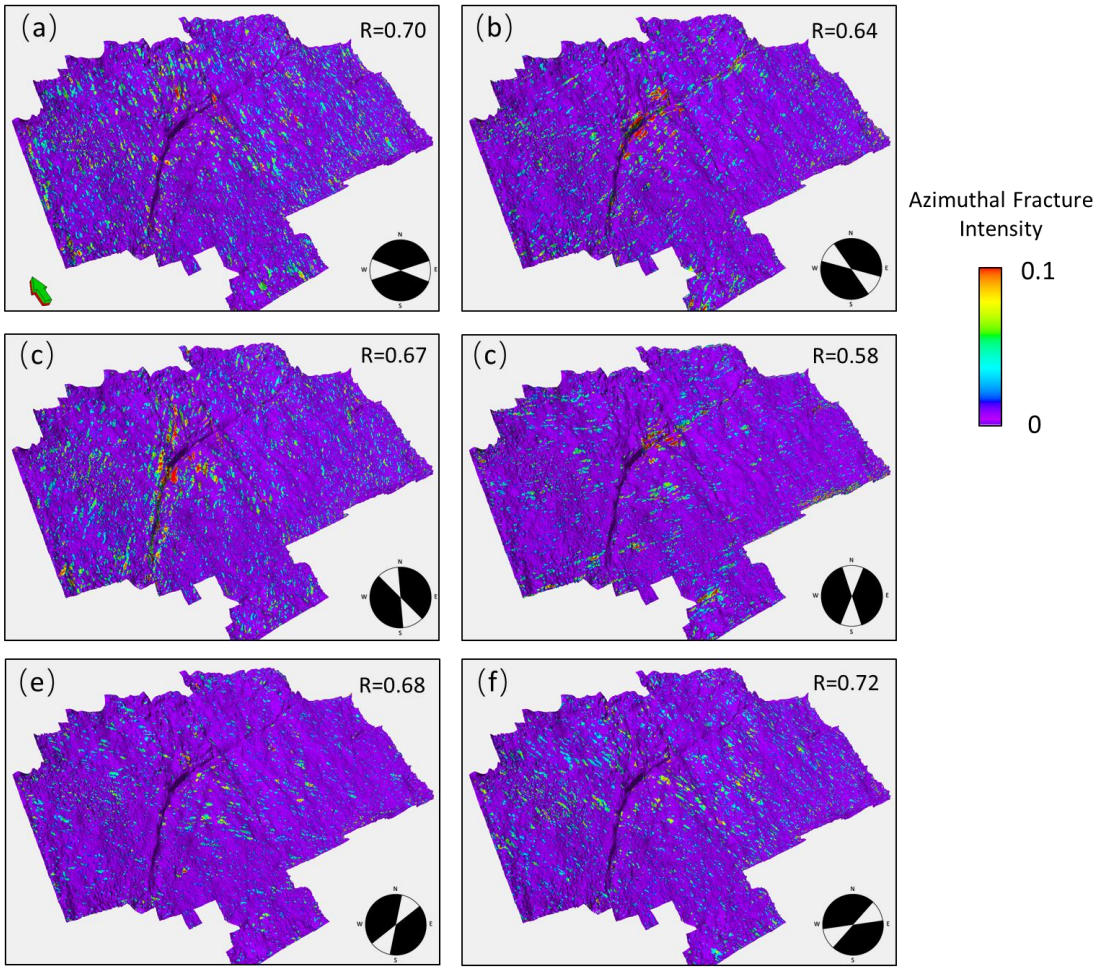

Figure 4.17. Azimuthal intensity was computed from the maximum aberrancy vector from azimuths (a) -90°, (b) -60°, (c) -30°, (d) 0°, (e) 30°, and (f) 60°. Azimuthal intensity was extracted onto a surface over the Mississippian Limestone. (f) 60° correlated best with predicted fractures density with a correlation coefficient of 0.72.

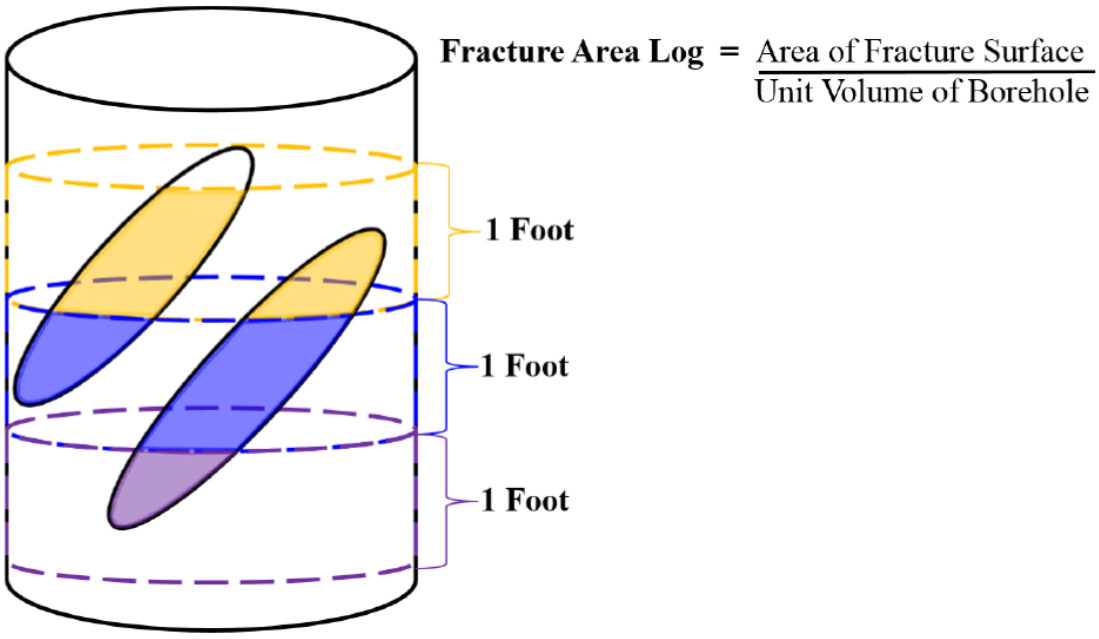

Figure A1. A schematic explaining the fracture area log that was generated based on the fracture interpretation. the fracture area logs were exported at 1 ft increment with a 1 ft step distance. Thus, the 1 ft of orange was exported out as the orange shaded area of fractures, divided by the volume of the orange cylinder (Cook, 2016).

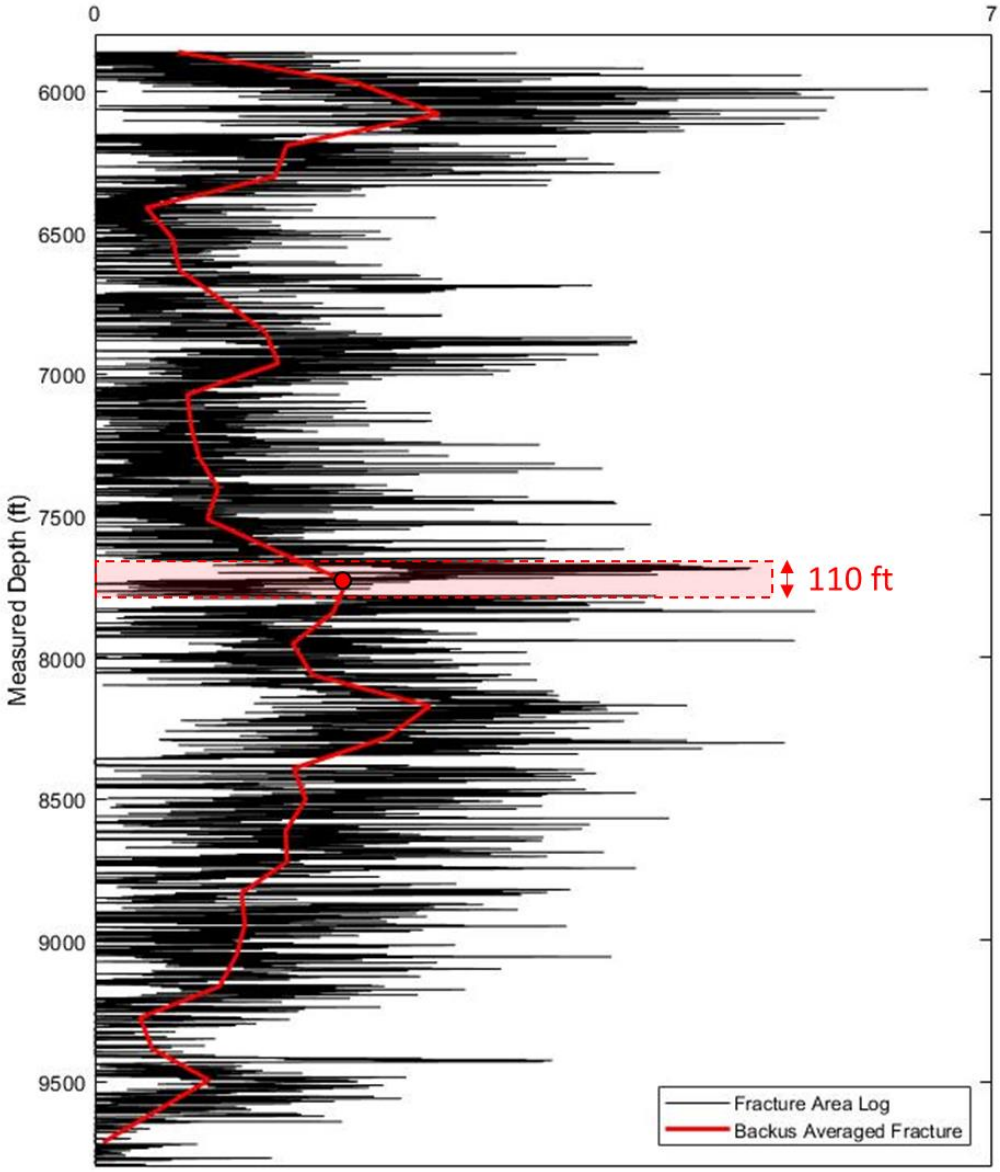

Figure A2. 1-ft resolution fracture count from the Fracture Area Log (in black) and corresponding 110-ft Backus averages (in red). The dashed area indicates the size and position of the sliding window.

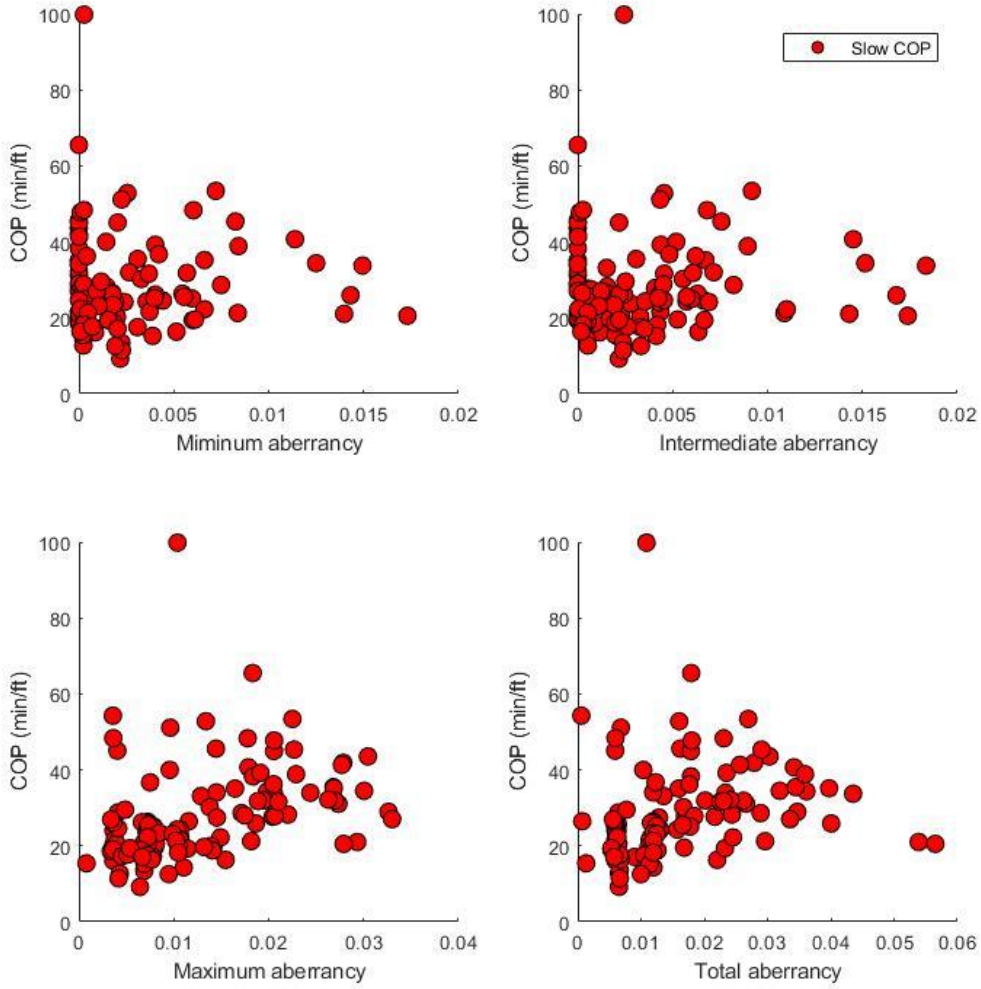

Figure B1. Cross plot of the magnitude of minimum, intermediate, maximum, total aberrancy computed from seismic volume against slow cost of penetration (COP). No statistically significant correlations were found between aberrancy vectors and slow COP.

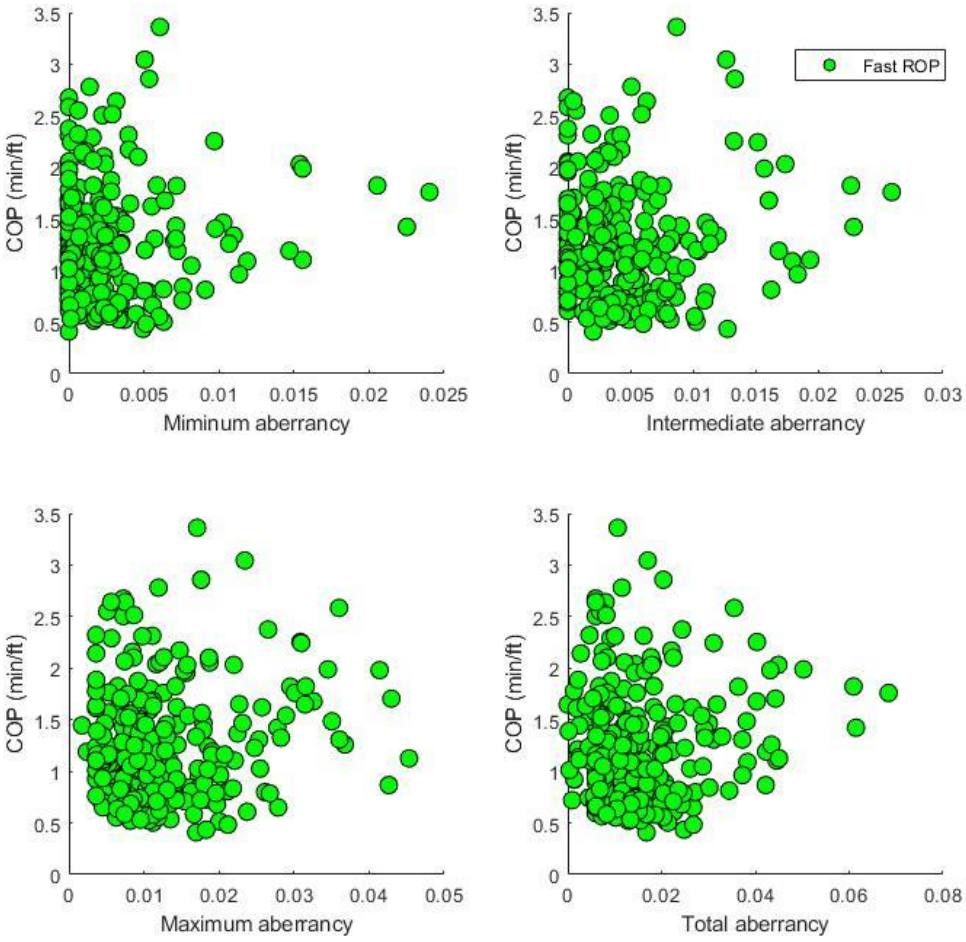

Figure B2. Cross plot of the magnitude of minimum, intermediate, maximum, total aberrancy computed from seismic volume against fast cost of penetration (COP). No statistically significant correlations were found between aberrancy vectors and fast COP.

REFERENCES

Ball M. M., H. E. Mitchell and S.E. Frezon, 1991, Petroleum geology of the Anadarko Basin region, Province (115), Kansas, Oklahoma, and Texas, Open-File Report 88-450W: U.S. Geological Survey.

Bosch, M., T. Mukerji, and E. F. Gonzalez, 2010, Seismic inversion for reservoir properties combining statistical rock physics and geostatistics: A review: Geophysics, **75**, 75A165-75A176, doi:10.1190/1.3478209.

Bowles, J. P. F., 1961, Subsurface geology of Woods County, Oklahoma: The Shale Shaker Digest, **IX–XI**, 197–215

Chopra, S., and K. J. Marfurt, 2005, Seismic attributes — A historical perspective: Geophysics, **70**, 3SO–28SO, doi:10.1190/1.2098670.

Chopra, S., and K. Marfurt, 2007, Seismic Attributes for Prospect Identification and Reservoir Characterization: Society of Exploration Geophysicists and European Association of Geoscientists and Engineers, doi:10.1190/1.9781560801900.

Chopra, S., and K. J. Marfurt, 2016, Understanding the seismic disorder attribute and its applications: The Leading Edge, **35**, 695–702, doi:10.1190/tle35080695.1.

Cook, S., 2016, Calibrating seismic fracture prediction using borehole image logs, application to the Mississippian Limestone: M.S. Thesis, University of Oklahoma.

Costello, D., M. Dubois, and R. Dayton, 2013, Core to characterization and modeling of the Mississippian, North Alva area, Woods and Alfalfa Counties, Oklahoma, in 2013 Mid-Continent Section AAPG Core Workshop: from source to reservoir to seal: Wichita, KS, 165–175.

Di, H., and D. Gao, 2014, A new algorithm for evaluating 3D curvature and curvature gradient for improved fracture detection: Computers & Geosciences, **70**, 15–25, doi:http://dx.doi.org/10.1016/j.cageo.2014.05.003.

Hagan, M. T., H. B. Demuth, M. H. Beale, and others, 1996, Neural network design: Pws Pub. Boston.

Hampson, D. P., J. S. Schuelke, and J. A. Quirein, 2001, Use of multiattribute transforms to predict log properties from seismic dataUsing Attributes to Predict Logs: Geophysics, **66**, 220, doi:10.1190/1.1444899.

Krizhevsky, A., I. Sutskever, and G. E. Hinton, 2012, ImageNet Classification with Deep Convolutional Neural Networks, *in* F. Pereira, C. J. C. Burges, L. Bottou, and K. Q. Weinberger, eds., Advances in Neural Information Processing Systems 25: Curran Associates, Inc., 1097–1105.

Leiphart, D. J., and B. S. Hart, 2001, Comparison of linear regression and a probabilistic neural network to predict porosity from 3-D seismic attributes in Lower Brushy Canyon channeled sandstones, southeast New Mexico: Geophysics, **66**, 1349–1358, doi:10.1190/1.1487080.

Lindzey, K., M. J. Pranter, and K. Marfurt, 2015, Geologically Constrained Seismic Characterization and 3-D Reservoir Modeling of Mississippian Reservoirs, North Central Anadarko Shelf, Oklahoma, *in* AAPG Annual Convention and Exhibition.

Manger, W. L., 2014, Tripolitic chert development in the Mississippian lime: New insights from SEM, in Mississippian Lime Play Forum, Oklahoma City, OK, USA.

Mathworks, 2017, Deep Learning with Matlab.

Mazzullo, S. J., B. W. Wilhite, and B. T. Morris, 2011, Mississippian Oil Reservoirs in the Southern Midcontinent: New Exploration Concepts for a Mature Reservoir Objective, v: Search and Discovery Article, p. 10373.

Parham, K. D., and R. A. Northcutt., 1993, Mississippian chert and carbonate basal Pennsylvanian sandstone; Central Kansas Uplift and northern Oklahoma, in Atlas of major midcontinent gas reservoirs: Texas Bureau of Economic Geology, Austin, TX, Gas Research Institute.

Perez, R., and K. Marfurt, 2013, Brittleness estimation from seismic measurements in unconventional reservoirs: Application to the Barnett Shale, *in* James Schuelke, ed., SEG Technical Program Expanded Abrstacts 2013, p. 2257–2293.

Poulton, M. M., B. K. Sternberg, and C. E. Glass, 1992, Location of subsurface targets in geophysical data using neural networks: Geophysics, **57**, 1534–1544, doi:10.1190/1.1443221.

Qi, X., and K. Marfurt, 2018, Volumetric aberrancy to map subtle faults and flexures: Interpretation, **6**, 1–17, doi:10.1190/int-2017-0114.1.

Schot, S. H., 1978, Aberrancy: Geometry of the third derivative: Mathematics Magazine, **51**, 259–275, doi:10.2307/2690245.

Scotese, C. R., 1999, Paleomap Project Web site: http://www.scotese.com/ (accessed February 13, 2016).

Staples, E., 2011, Subsurface and experimental analyses of fractures and curvature: M.S. Thesis, University of Oklahoma

Stearns, V. T., 2015, Fracture characterization of the Mississippi lime utilizing whole core, horizontal borehole images, and 3D seismic data from a mature field in Noble County Oklahoma: M.S. thesis, University of Oklahoma, Norman, Oklahoma, 75 p.

Trumbo, D. B., 2014, A production calibrated reservoir characterization of the Mississippi Lime in a mature field utilizing reprocessed legacy 3D seismic data, Kay County, Oklahoma: University of Oklahoma.

White, H., B. Dowdell, and K. J. Marfurt, 2012, Calibration of surface seismic attributes to natural fractures using horizontal image logs, Mississippian Lime, Osage County, Oklahoma, *in* D. Steeples, ed., SEG Technical Program Expanded Abstracts 2012, p. 1–6.

Wu, H., and D. D. Pollard, 2002, Imaging 3-D fracture networks around boreholes: AAPG bulletin, **86**, 593–604.

Young, E. M., 2010, Controls on reservoir character in carbonate-chert strata, Mississippian (Osagean-Meramecian), southeast Kansas: University of Kansas.

Zemanek, J., R. L. Caldwell, E. E. Glenn Jr., S. V Holcomb, L. J. Norton, and A. J. D. Straus, 1969, The Borehole TeleviewerA New Logging Concept for Fracture Location and Other Types of Borehole Inspection: doi:10.2118/2402-PA.

APPENDIX A: SEISMIC CALIBRATION BOREHOLE FRACTURE INTERPRETATION

In this appendix, I show how fracture density and Backus averaging fracture density were generated.

APPENDIX B: CORRELATION BETWEEN COP AND ABERRANCY

In this appendix, I show two cross plots between COP and the magnitude of four aberrancy. Two sets of COP were correlated with the magnitude of aberrancy, slow (Figure B1) and fast COP (Figure B2), with the average value of 27 min/ft and 2.5 min/ft, respectively. No statistically significant correlations were found between the magnitude of aberrancy and COP.

CHAPTER 5

CONCLUSIONS

Seismic attribute assisted reservoir characterization is a critical process in today's oil and gas industry to perform prospect evaluation. It provides interpreters with an optimal understanding of the reservoir's internal architecture and properties. This process has become significantly necessary since the era of "unconventional reservoir revolution" has begun since 2005. Higher-intensity completion design, longer horizontal sections in a well lead to more hydrocarbons recovered per well and higher production rates. All of these revolutions requires technology advancements such as providing more accurate subsurface seismic imaging, creating "perfect" fracture systems, reducing completion costs, use of data analytics to achieve productivity improvements. Since the mid-1990s, seismic attributes have widely used to capture the morphological features seen in seismic data. Seismic imaging brings large-scale reservoir behavior. Geostatistical stochastic stimulations add spatial correlation and small-scale variability which is hard to identify from seismic due to the limits of resolution. Unconventional reservoir characterization is more commonly the product of comprehensive integration of software, data, and specialize measurements.

In this dissertation, I examined the feasibility of using seismic attributes to predict fractures and rate of penetration. I spent particular focus on a new seismic attribute, aberrancy, which was previously limited to analysis of interpreted horizons to 3D analysis of uninterpreted volumes.

Aberrancy complements rather than supplants other structural attributes such as coherence, curvature, and diffraction imaging. I extended the 2-D aberrancy to volumetric results of uninterpreted seismic data volumes. Specifically, I used a long wavelength calculations successfully used in volumetric curvature computations, implemented as convolution operators in the original unrotated data volume. The new volumetric aberrancy are numerically stable, computationally efficient, and geologically meaningful in mapping faults and flexures.

Depending on the deformation, there may be as many a three independent aberrancy vectors. For a simple linear flexure there is only one aberrancy vector, the maximum aberrancy. For curvilinear and crossing flexures there may be also an intermediate and minimum aberrancy vector. I therefore wished to understand whether more complex deformation leads to increased number of natural fractures. While I hypothesized that aberrancy, which measures strain, should be correlated to natural fractures seen in horizontal image logs, this correlation was less than 10%. While not useful by itself as a fracture indicator, aberrancy was quite useful when combined with other attributes using a convolution neural network estimation. In this case, I was able to find a training accuracy of 78%, validation accuracy of 43%, and testing accuracy of 56%.

Attributes can also be correlated to the rate of penetration. Using a proximal support vector machine I found a prediction accuracy of 94%. By using this workflow, one can use rate of penetration of previously drilled wells with 3-D seismic data to predict rate of penetration over the study area. Whereas one may still wish to drill a specific target

objective, this statistical analysis technique will provide a more accurate cost estimate and help choose the appropriate drilling equipment.